Department of Physics and Astronomy

University of Heidelberg

Master thesis

in Physics

submitted by

Kristian Ehlert

born in Weilburg

2017

Simulating the interaction of extragalactic jets with turbulent magnetic fields in galaxy clusters

This Master thesis has been carried out by Kristian Ehlert

at the

Heidelberg Institute for Theoretical Studies

under the supervision of

Prof. Dr. Christoph Pfrommer

with the second referee

Prof. Dr. Volker Springel

Simulationen der Interaktion von extragalaktischen Jets mit turbulenten Magnetfeldern in Galaxienhaufen:

Galaxienhaufen mit kurzen zentralen Kühlzeiten sollten große Massenkühlungs- und Sternentstehungsraten haben, welche man nicht beobachtet. Die im Galaxienhaufenzentrum gelegenen aktiven Galaxienkerne injizieren viel Energie in Form von heißen Gasblasen, welche die kühlenden Galaxienhaufen heizen können. Kosmische Strahlung (KS) aus den Gasblasen induzieren Alfvénwellen, welche ausreichend Wärme liefern könnten. Wir simulieren die Entstehung und Entwicklung der Gasblasen durch energetische Ausflüsse in ein realistisches Haufenmedium. Um dieses Ziel zu erreichen, halfen wir bei der Entwicklung eines Jetmoduls für den magnetohydrodynamischen Code Arepo mit, und entwickelten eine Methode, um eine turbulente, magnetische Atmosphäre in Galaxienhaufen zu erstellen. Unsere Simulationen zeigen, dass magnetisierte Gasblasen und die angesammelten magnetischen Hüllen Kelvin-Helmholtz und Rayleigh-Taylor Instabilitäten unterdrücken und die Blasen stabilisieren. Die Magnetfelder im Sog der Gasblasen werden deutlich verstärkt, was die KS-Heizrate erhöht. Die resultierende KS-Verteilung von niedrigenergetischen Jets weist eine hohe Isotropie im Kern des Galaxienhaufens auf. Für höhere Jetenergien sinken die KS-Heizraten im Zentrum, aufgrund der kleineren Volumenanteile und der höheren Anisotropie der KS. Diese Ergebnisse stellen einen sehr wichtigen Schritt dar, um zukünftig kosmologische Simulationen von Galaxienhaufen mit selbstregulierendem KS-Feedback durchzuführen.

Simulating the interaction of extragalactic jets with turbulent magnetic fields in galaxy clusters:

Galaxy clusters with short central cooling times are expected to show abundant star formation and cooling flows. However, those are not observed. Active galactic nuclei in the center of clusters launch buoyant bubbles with sufficient energy to offset radiative cooling. Escaping cosmic rays (CRs) from these bubbles provide a viable heating mechanism via the dissipation of CR-excited Alfvén waves. We simulate the formation and evolution of bubbles via self-consistently launched jets into a realistic intra-cluster medium. To this end, we assisted in developing a jet module in the moving-mesh code Arepo and set up a turbulent, magnetized cluster atmosphere on a nested mesh. We find that magnetized lobes and draped external magnetic fields suppress Kelvin-Helmholtz and Rayleigh-Taylor instabilities, thereby confining the bubbles. We see an enhancement of the magnetic field in the wake of the bubbles, which increases the CR heating rate. The resulting CR distribution of low-energy jets shows a high degree of isotropy in the cluster core. With increasing jet energy, the CR depletion time of the bubbles decreases in the center, thus lowering the CR volume fraction and the degree of isotropy. These findings represent a very important step towards self-regulated simulations of CR feedback in cosmologically evolving galaxy clusters.

Contents

1 Introduction

Galaxy clusters are the largest gravitationally bound systems in the universe. In clusters, a significant fraction of the mass resides in the form of a hot gas, the so-called intra-cluster medium (ICM), which radiates bremsstrahlung in X-rays (Voit 2005). In some clusters, the ICM should radiate away its energy time scales considerably shorter than the Hubble time. As a consequence, copious star formation and mass deposition rates are expected in the center of these cool-core (CC) clusters, which are not observed (Peterson and Fabian 2006). In addition, observations show an abundance of X-ray cavities in CC clusters (Bîrzan et al. 2004) that often coincide with radio-synchrotron emitting lobes. These lobes are injected by jets, which are driven by an accreting super-massive black hole (SMBH) in the center of the cluster (Worrall 2009).

The enthalpy content of the bubbles and their duty cycle provide a heating rate that is sufficient to balance radiative cooling of the ICM (McNamara and Nulsen 2012). Multiple generations of bubbles are observed, which suggests the existence of a self-regulated feedback loop. However, the main mechanism for linking the bubble energy to the cooling gas remains unclear. Suggestions include heating through the dissipation of induced weak shocks (Li et al. 2016), sound waves (Fabian et al. 2017) and turbulence (Zhuravleva et al. 2014) and thermal conduction (Voigt and Fabian 2004; Ruszkowski and Oh 2010).

On the other hand, we observe diffuse, polarized radio emission in the form of radio mini halos in CCs (Giacintucci et al. 2014b). This synchrotron radiation reveals the presence of magnetic fields and highly-energetic non-thermal electrons, so-called cosmic ray (CR) electrons. Since particle acceleration processes can even more efficiently energize ions, an additional model was proposed that relies on the dissipation of Alfvén waves, which are excited by propagating CR ions (Loewenstein et al. 1991; Guo and Oh 2008; Pfrommer 2013). The viability of this model critically depends on the dynamics of the bubble, the geometry of cluster magnetic fields and the distribution of the escaping CRs. The buoyantly rising bubbles are unstable to Kelvin-Helmholtz and Rayleigh-Taylor instabilities. Simulations of moving bubbles show that magnetic fields (Dursi and Pfrommer 2008) and viscosity (Reynolds et al. 2005) provide sufficient stability to bubbles. In more realistic turbulent environments, magnetic fields have also shown to suppress instabilities (Ruszkowski et al. 2007).

This work studies self-consistently inflated bubbles in a turbulent, magnetized idealized cluster potential. Since this problem is highly non-linear, three-dimensional simulations are inevitable. To this end, we employ the magneto-hydrodynamical code AREPO (Springel 2010). The utilized jet model by Weinberger et al. 2017 was thoroughly tested as part of this thesis. In addition, we set up a turbulent, Gaussian-distributed magnetic field to improve our understanding of the bubble with the ambient magnetized ICM. In addition, we closely follow the evolution of the escaping CRs. These findings are an important step towards self-regulated simulations of CR feedback in cosmologically evolving galaxy clusters and to identify numerical limitations of the algorithms used.

We introduce the physics of CC clusters, streaming CRs and AREPO in Section 2. The numerical set up of a jet in a turbulent, magnetized cluster potential is presented in Section 3. The subsequent analysis discuses the evolution for different MHD and jet parameters, the influence of the external magnetic field and their consequences on the CR distribution (Section 4). We summarize our results in Section 5.

2 Theoretical Background

2.1 Galaxy clusters

2.1.1 Introduction to galaxy clusters

As the pinnacle of structure formation, galaxy clusters are still in the process of forming the largest gravitationally bound systems in our universe. As apparent in the optical, galaxy clusters host of order 10^3 galaxies. They extend out to $R_{200} \sim 1 - 3$ Mpc. R_{200} corresponds to the radius where the mean density of the cluster is equal to 200 times the critical density of the universe $\rho_{\rm crit}$. Hot gas ($1 - 10$ keV) in clusters is visible in the X-ray due to thermal bremsstrahlung and line emission of highly ionized metals. Most of their total mass ($\sim 10^{14} - 10^{15}$ $M_\odot$) is however contained in dark matter (DM). Only around 2% is made up of stars. Around 13% is due to hot gas. The remaining 85% is contributed by dark matter.

The most popular parametrization of the dark matter halo, obtained from DM halo formation simulations (Navarro et al. 1996, 1997), is the so called Navarro-Frenk-White (NFW) profile whose density profile $\rho(r)$ is given by

$$\frac{\rho(r)}{\rho_{\rm crit}} = \frac{\delta_c}{\frac{r}{r_s}\left(1 + \frac{r}{r_s}\right)^2} \tag{2.1}$$

where the critical density of the universe is $\rho_{\rm crit} = 3H^2/(8\pi G)$ (H is the Hubble constant), the scale radius is $r_{\rm s} = r_{200}/c$ and the characteristic overdensity of the halo is $\delta_{\rm c}$. As mentioned above, by definition r_{200} marks the radius within which the mean density of the halo is equal to $200\rho_{\rm crit}$. This can be used to create a dependence between the so called concentration c and $\delta_{\rm c}$.

Clusters form where waves of primordial density fluctuations after the Big Bang interfere constructively. The subsequent non-linear evolution has to be determined through numerical simulations. It has become evident that dark matter tends to clump in halos, which assembles in filamentary structures throughout the universe. In the hierarchical structure formation model, galaxy clusters form at the intersection of these filaments through mergers of smaller groups of galaxies and inflowing gas. The more massive the system the later it forms. Galaxy clusters are still in the process of forming. Clusters grow due to the inflow of gas and merger events with other clusters. If both clusters in a merger are of comparable size the merger is classified as a major merger. On average the typical time after the last major merger is around 5 Gyr. Around 20% of clusters just recently underwent a merger (Peterson and Fabian 2006). Due to the progressing accelerated expansion of the universe cluster will also remain the biggest objects in the universe.

Inflowing gas into the halo of the cluster is shock-heated at strong accretion shocks. The gas virializes within the gravitational potential of the cluster. Derived temperatures of the *inter cluster medium* (ICM) are consistent with the galaxies and gas being in equilibrium within a common gravitational potential. The temperature of the gas is equal to the so called virial temperature of the cluster potential which ranges from 10^7 to 10^8 K. For a relaxed cluster also the galaxy dispersion along the ling of sight σ can be related to the temperature of the cluster as $T \propto \sigma^2$.

If the gas mass exceeds a certain density threshold, the gas is able to cool efficiently. Thereby stars are able to form or the gas is accreted by a *super-massive black hole* (SMBH) found in the center of most galaxy clusters. SMBHs are usually found in the central *brightest cluster galaxy* (BCG). Star formation and the formation of SMBHs result in feedback processes through *supernovae* (SNe) and *active galactic nuclei* (AGNs), respectively. By these processes part of the mass, energy and metals are injected into the ICM.

X-ray observations of clusters reveal discontinuities in surface brightness maps, so called *cold fronts*. These features are not shocks as initially thought but rather contact discontinuities. They likely result from in-streaming gas from the cool core of a merged sub cluster (Govoni and Feretti 2004). In this scenario the inflowing gas from the merging subcluster is able to displace the central ICM. This forces the ICM to slosh around in the potential of the cluster. Eventually the now cold part of the ICM falls back into its dark matter halo creating a contact discontinuity between the hot gas in the core of the cluster and the returned cold gas (Markevitch and Vikhlinin 2007). These fronts appear rather long-lived such that thermal conduction as well as mixing instabilities like Kelvin-Helmholtz instabilities have to be strongly suppressed in these environments. Both observational facts suggest that the infalling gas is able to form a magnetized layer that is able to stabilize the interface (Markevitch and Vikhlinin 2007; Chen et al. 2017). This hypothesis is also supported by simulations (ZuHone et al. 2013, 2015).

A variety of other non-thermal phenomena have been observed in galaxy clusters. Radio synchrotron emission has been detected in distinguishable morphological types. So called *radio halos*/*mini radio halos* show large scale/small scale cluster-wide emission whereas *radio relics* appear more elongated and appear in cluster outskirts. The radio emission is produced by GeV relativistic electrons and μG fields (Section 2.2.1). From Faraday rotation measurements of background sources the magnetic field in clusters has also been detected and its value can be constrained (Section 2.1.5).

2.1.2 Cool core clusters

Clusters can be subdivided into *cool core clusters* (CCs) and *non-cool core clusters* (NCCs). CCs are characterized by low cooling times $\lesssim 1$ Gyr in their inner ~ 100 kpc. They lack the expected large-scale mass deposition rates (*cooling flow*) and significant star formation.

The cluster gas shows small entropies and rather low central temperatures, which cause the central cooling time to be on the order of or below one giga year. Consequently, copious star formation and large-scale cooling flows are expected, which are however not observed (Peterson and Fabian 2006). The star formation rate is observed to be suppressed in the central *giant elliptical galaxy* (cD galaxy) (Hoffer et al. 2012). *Chandra* and *XMM-Newton* revealed that even though the temperature drops in the center of CCs, the temperature never falls below a certain threshold. The threshold is usually at one half to one third of the average cluster temperature at around 1 keV (Blanton et al. 2010). Some small-scale colder filaments have however been observed (Werner et al. 2013, 2014).

Low levels of observed line emission at least exclude a one-phase cooling flow (e.g. Peterson et al. 2001; Böhringer et al. 2001). All of the above points to a local heating process that prevents the gas temperature to decrease below a certain threshold while at the same time it does not dominate the cooling process.

X-ray cavities detected by *Chandra* in the center of clusters have inspired many theories of AGN related feedback (see Section 2.1.4). The massive central BCG hosts a SMBH that accretes surrounding gas. The SMBHs powers a jet that shocks the ICM thereby inflating lobes. These hot lobes are then observed as cavities in the probed X-ray band. They leave the central region and rise buoyantly through the ICM. These, so-called bubbles, produce shocks

and sound waves (e.g. Blanton et al. 2010). The observed quasi-balance between heating and cooling points towards a self-regulated system. If the gas cools, more mass is accreted and jet activity is triggered that heats the cluster (McNamara and Nulsen 2012).

However the exact coupling mechanism responsible for supplying and distributing heat in a volume filling fashion throughout the core of the cluster has not been identified yet. Different theories exists such as weak shocks (David et al. 2001; Li et al. 2016; Guo et al. 2017), dissipation of sound waves (Mathews et al. 2006; Fabian et al. 2017), mixing of AGN bubble content (Gilkis and Soker 2012; Hillel and Soker 2016), turbulent dissipation (Sanders et al. 2011; Zhuravleva et al. 2014), thermal conduction (Voigt and Fabian 2004; Ruszkowski and Oh 2011) and cosmic rays (e.g. Guo and Oh 2008; Jacob and Pfrommer 2017b).

Thermal conduction has been identified as an efficient way in heating the outer parts of the cluster. However, it is mostly excluded in the central regions of the cluster because it is locally unstable. High resolution X-ray spectroscopic measurements by *Hitomi* inferred low velocity dispersions in the Perseus cluster excluding models with strong shocks or high levels of turbulence (Hitomi Collaboration et al. 2016). The remaining heating processes are probably all relevant. Clearly identifying the dominating one(s) remains a challenging problem.

The relation between heating in CCs and AGNs will be discussed in more detail in the next section. We subsequently present different heating mechanisms.

2.1.3 Active galactic nuclei

Active galactic nuclei (AGN) are compact regions at the center of galaxies that emit non-thermal radiation. In extragalactic radio sources bipolar outflows of magnetic fields and relativistic particles are observed from AGNs (Harris and Krawczynski 2006; Worrall 2009). Two collimated jets originating from the AGN in opposite directions are usually detected. The jets terminate in large-scale underdense cavities in X-rays which rise as bubbles in the atmosphere of the cluster. They also emit synchrotron radiation, which is visible in the radio. The radiation originates from *cosmic ray* (CR) electrons gyrating around magnetic field lines.

Theory

The jets originate from a *supermassive black hole* (SMBH) at the center of the AGN. The jet is powered by the black hole. It travels from the radius of the SMBH at 10^{-4} pc for $M_{\mathrm{BH}} = 10^9\ M_\odot$ to lobes and hotspots on scales up to Mpc. As evident, this immense range of scales of 10 orders of magnitude poses a big challenge to numerical simulations which have to focus on a subrange of these scales. The exact composition of the jet is not well constrained including the specific source of the relativistic CRs (Harris and Krawczynski 2006). A variety of formation processes for extragalactic jets have been proposed. Some principle processes are summarized in the following (Hawley et al. 2015).

There are two popular mechanisms possibly responsible for powering the jet. First, there is the Blandford-Znajek (BZ) process (Blandford and Znajek 1977). Here, the jet is powered by the rotational energy of the SMBH in combination with a large-scale magnetic field of the accretion disk. Secondly there is the Blandford-Payne (BP) process (Blandford and Payne 1982). Here, the jet power is directly provided by the accretion disk. The magnetic field is supplied by the black hole-disk system either through a dynamo effect in the disk or the inwards advection of magnetic fields. The accreting plasma is then funneled into a plasma wind from the disk surface that is still coupled to the magnetic field and accelerated through magneto-centrifugal forces.

As the plasma is linked through magnetic field lines, the differential rotation of the plasma combined with its inertia results in the conversion of part of the poloidal magnetic field into

a toroidal field component. The toroidal field component is enhanced to immense values such that the field lines expand under their own pressure. Thereby, the plasma is accelerated while also confined in form of a jet. The velocity of the plasma exceeds the speed of magneto-sonic waves in the medium and thereby causally decouples from the surrounding medium. As it collides with the ambient medium, a shock develops that thermalizes part of the jet energy.

The observable part of the jet is confined to the scales after the jet has interacted with the ambient medium. Figure 2.1 shows the jet and part of the lobe of Cen A in the radio and X-rays. The large-scale jet gives rise to synchrotron emission. Inverse-Compton emission can be observed when relativistic leptons interact with a photon field. In addition the large-scale X-ray cavities created at the termination of the jet within the cluster have been detected. These bubbles eventually decouple spatially from the jet region and buoyantly rise in the atmosphere of the cluster. They are the reservoir of energy which is likely responsible for heating CCs. The reasons for this will be explained in the next sections.

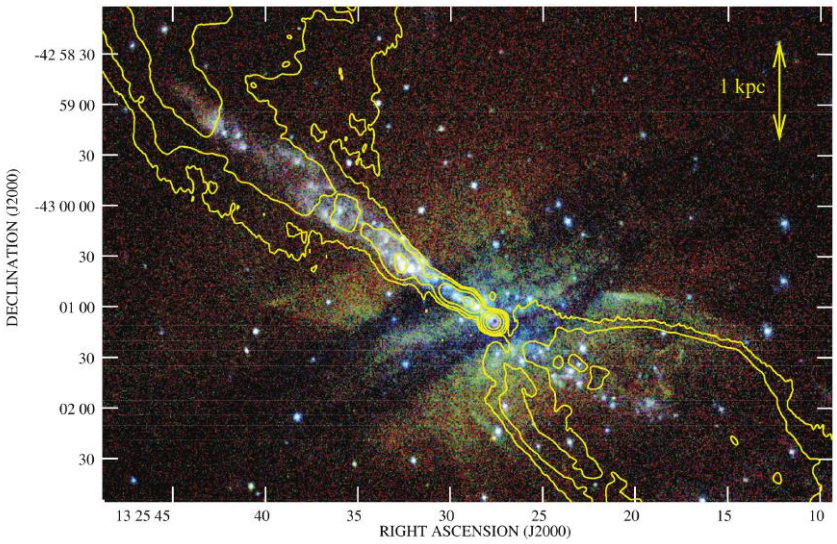

Figure 2.1: Image of the jet and counter-jet regions of Cen A using all ACIS observations. The *Chandra* data has been exposure-corrected at an appropriate energy and then combined, and weighted according to the value of the exposure map. The images are binned in standard *Chandra* pixels (0.492″ on a side) and smoothed with a FWHM = 1.0″ Gaussian. Red shows exposure-corrected counts in the energy range 0.4–0.85 keV, green shows 0.85–1.3 keV, and blue 1.3–2.5 keV. Contours [7×(1, 4, 16, ...) mJy beam] are from the 5 GHz VLA map of Hardcastle et al. (2006) with 6.0″ resolution. Surely the radio emission and probably also the X-ray emission in the jet originate from synchrotron radiation (Hardcastle et al. 2007b).

Two classes of jets

In the radio, two classes of radio galaxies (FR I/II) have been introduced by Fanaroff and Riley (1974) purely on morphological grounds. They determined the ratio of the distance between their brightest data point on both sides of the jet to the distance that separates the lowest contour line on both sides. FRII now refers to radio galaxies with a ratio above 0.5, thus referred to as *edge-brightened* sources. And sources with ratio below 0.5 are termed FRI or *edge-darkened*. FRI jets are generally attributed to rich clusters including CCs. Thus, we focus on this type. In agreement with the radio morphology criterion is the criterion based on radio power with objects below $\sim 10^{25}\ h_{70}^2$ W Hz^{-1}str^{-1} at 178 MHz mostly being FRI sources.

Ledlow and Owen (1996) found a crucial divide between FRI and FRII sources when comparing the radio power $L_{\rm R}$ of the jet with the optical luminosity $L_{\rm opt}$ of the galaxy. Sources above the dividing line that scale as $L_{\rm R} \propto L_{\rm opt}^{1.7}$ are predominantly identified as FRII sources. This strong correlation points towards the two types being the result of environmental factors.

FRI sources tend to show more broadened jets terminating in more diffuse lobes that experience significant deflections. These are probably the result of ram-pressure interactions between the moving source with the ambient medium (Worrall 2009). FRI jets usually show their maximum brightness not far away from the AGN. Further out the radio power smoothly declines. In this region bright knots in the X-ray and radio are observed. The jets are assumed to be slowed down by the surrounding medium to sub-relativistic speeds (Laing and Bridle 2014). Strong velocity shear between the moving jet and the quasi-stationary external medium should drive instabilities at the interface and make the flow turbulent (Worrall 2009).

On the other hand FRII jets keep their relativistic speeds out to large distances where they terminate in bright hotspots. They show mostly one-sided jets and are predominantly found in poorer environments. Using the assumption of equipartition (see Section 2.1.5) the magnetic field in radio radio lobes and hotspots has been estimated at $2-200$ μG (Kataoka 2005) reaching field strengths of up to 3 mG (Godfrey et al. 2009). They stay collimated for longer and are thus able to transport energy further out into the halo. They are assumed to have sufficient energy and momentum to drive a bow shock in the ambient medium and reach length scales of hundreds of kpc. Thus, they dump the majority of their energy at their termination point in contrast to FRI sources which gradually dissipate their energy while entraining significant fractions of the ambient medium.

Observational bubble physics

The dimension of jet-inflated bubbles and X-ray cavities cover a large range in scales from a few kpc (e.g., in Abell 262 Blanton et al. 2004) to hundreds of kpc (in MS0735.6+7321, McNamara et al. 2005). As discussed in more detail in Section 2.1.3, one can infer the pressure of bubbles assuming equipartition between the relativistic electron and magnetic field component to explain the synchrotron emission. The inferred pressure is only $\sim$ 10% of the pressure of the ICM. For reasons of stability non-thermal components like low energy, relativistic electrons, protons, higher magnetic field strengths or very hot, diffuse, thermal gas should be present. The later has not been observed but a few upper limits exist; $kT > 15$ keV in Hydra A (Nulsen et al. 2002), $kT > 11$ keV in Perseus (Schmidt et al. 2002) and $kt > 20$ keV Abell 2052 (Blanton et al. 2003). Bubbles further out of the cluster show fainter or no radio emission at 1.4 GHz with steeper spectra (Blanton et al. 2010). However at lower frequencies, e.g. at 330 MHz radio emission extends all the way out to the cavities (Wise et al. 2007).

The cavities are observed to form thin dense shells at the leading edge. The gas has been shown to be cooler than the ambient gas at the specific height in the cluster atmosphere (i.e. Hydra A, Nulsen et al. 2002; Perseus A, Schmidt et al. 2002). The cooling time within the shells seems longer than the radio source age. This indicates an origin of the gas closer to the center from where it was lifted by the rising lobes. For example; in Abell 2052 the cooling time in the shell is $\sim 3 \times 10^8$ years whereas the source age is estimated at $\sim 10^7$ years (Blanton et al. 2010). In some cases, optical-line emission like Hα is observed to be coincident with the X-ray shells, which requires gas temperatures on the order of 10^4 K (Fabian et al. 2003b; Blanton et al. 2004)). Consequently, cooler localized gas exists in CCs and some star formation has been observed (McNamara 1997).

Further out, bubbles also seem to entrain gas out of the center into the ICM. In M87, there is a clear correspondance between cool rims and lobes (Belsole et al. 2001; Young et al. 2002; Forman et al. 2005, 2007). In the Perseus cluster, colder gas at $\sim 10^4$ K (Hα) from the center

of the cluster seems to be entrained by one of the outer cavities (Fabian et al. 2003b). In Figure 2.2 an image of the X-ray emission in the Perseus cluster is shown with superimposed Hα emission. One X-ray cavity is clearly visible in the north-east of the cluster with a laminar wake traced by Hα emission.

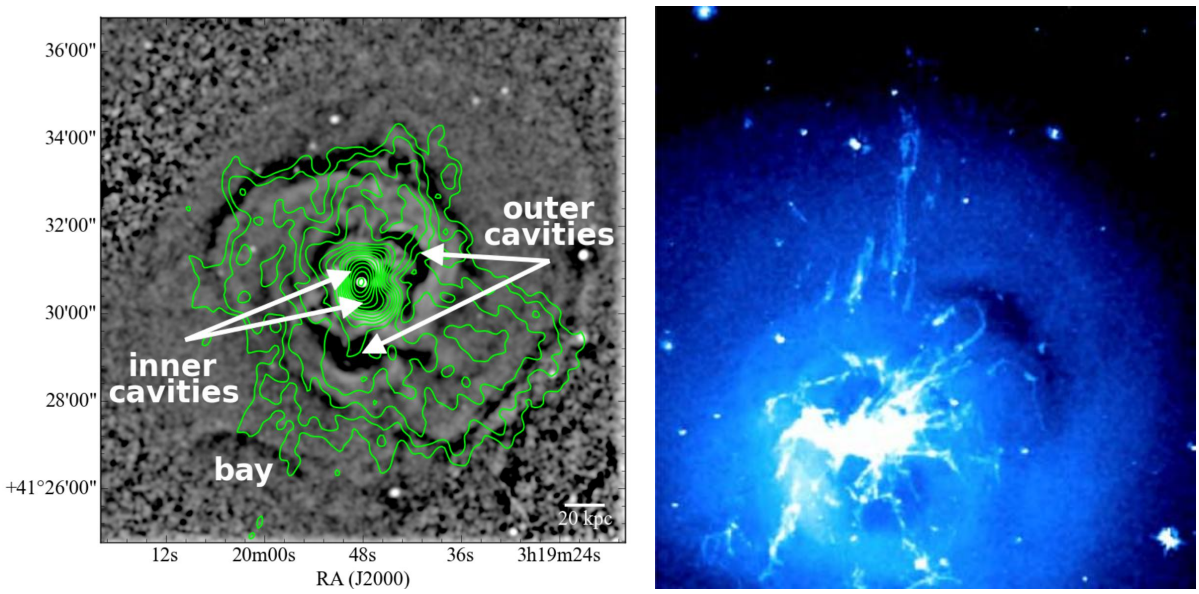

Figure 2.2: On the left a X-ray surface brightness residual map by *Chandra* is shown of the Perseus cluster. Contours correspond to low frequency 140 Mhz radio data from LOFAR (Kokotanekov et al. 2017). The discernible bubbles are also traced by the radio emission. On the right a *Chandra* X-ray image of the core region (96 kpc a side) is shown. Hα emission recorded by the Wisconsin Indiana Yale NOAO telescope (Reynolds et al. 2005) is shown in white. Arcs are clearly visible in the trail of the rising bubbles.

In Hydra A AGN activity has been observed to be responsible for lifting metals out of the center of the cluster (Kirkpatrick et al. 2009; Kirkpatrick and McNamara 2015) and excess metallicity along the jet axis has been detected in 17 clusters with cavities (McNamara and Nulsen 2012). All these observations are in good agreement with the more general observation that the ICM is enriched by metals on levels of one third solar metallicity. However close to the BCG the iron abundance can even exceed the solar metallicity (De Grandi et al. (2004), Allen and Fabian (1998)). The profile decreases with distance from the BCG. The slope of the profile is shallower than expected if it was solely due to stellar feedback (Rebusco et al. 2005). Mechanical jet power $P_{\rm jet}$ even seems to correlate with the radius out to which significant enhancement in iron $R_{\rm Fe}$ has been detected as $R_{\rm Fe} = 60 P_{\rm jet}^{0.43}$ where $R_{\rm Fe}$ is given in kpc and the jet power $P_{\rm jet}$ is expressed in units of 10^{44} erg s^{-1} (Kirkpatrick et al. 2011).

The exact path a rising bubble travels can be determined by atmospheric pressure gradients (Morsony et al. 2010). However the jet launching direction has been observed to vary (Dunn et al. 2006). This may be due to deflected jets (Pollack et al. 2005), randomly-oriented accretion disks (King and Pringle 2007) or jet precission (Gaspari et al. 2012). In some cluster (i.e., 2A 0335+096 Sanders et al. 2009) older bubbles have also been observed with a considerable offset from the current jet axis.

A rising bubble displaces gas, which generates kinetic energy in its wake from instreaming gas to fill the resulting low-density wake. This energy heats the surroundings. The bubble loses the same amount of enthalpy (McNamara and Nulsen 2007). The buoyantly rising bubbles are assumed to be disrupted through Kelvin-Helmholtz or Rayleigh-Taylor instabilities. In the

case of Abell 2052, Rayleigh-Taylor instabilities (Soker et al. 2002) might have been observed (Blanton et al. 2001, 2003). Magnetic draping should suppress these instabilities (Lyutikov 2006; Ruszkowski et al. 2007) and/or at least initially provide a pressure related to the inflation of the bubble (Pizzolato and Soker 2006).

Composition of the jet plasma

As already shown by *Einstein* and *ROSAT* X-ray telescopes the minimum pressure in FRI jets is normally below the pressure of the hot surrounding gas of the cluster (Morganti et al. 1988; Feretti et al. 1995; Worrall and Birkinshaw 2000). At the present time the external pressure on the jets can be constrained on scales from a few to several hundred kpc using *Chandra* and *XMM-Newton* observations (e.g., Hardcastle et al. 2002; Croston et al. 2008) yielding results in agreement with the previous findings. Either very hot gas > 20 keV is able to avoid detection (Gitti et al. 2007) or more likely, a non-thermal component has to be present to stabilize the bubble (McNamara and Nulsen 2012).

Observed polarized synchrotron radiation points towards the existence of relativistic particles and magnetic fields. Because of confinement the plasma should be neutral. This is possible through a variety of combinations of electrons, positrons and protons. Further constrains come from the power of the observed synchrotron emission. Here, electrons and positrons are favored as synchrotron energy losses are proportional to the inverse of the square mass of the particle. In addition, the jet power can be estimated in some cases from the detection of older cavities in the ICM. They can be used to calculate the enthalpy necessary to displace the gas (Bîrzan et al. 2004; Dunn et al. 2005; Allen et al. 2006). Averaging over the lifetime of the source yields constraints for the total energy of all particles in the jet including magnetic fields and the bulk Lorentz factor (Schwartz et al. 2006). Assuming equipartition (Section 2.1.5), the pressure provided by the radiating relativistic electrons (positrons) and the magnetic field remains insufficient (e.g., Croston et al. 2003; Croston 2008; Bîrzan et al. 2008).

Equipartition between the internal pressure, which is composed of electrons/positrons and magnetic field, and the external pressure has been observed in FRII sources with a dominance in leptons (e.g. Isobe et al. (2002)). Too large relativistic electron fractions can be excluded in most FRI sources on the basis of non-detection of inverse-Compton emission in the X-ray (Croston et al. 2003). Assuming the thermal contribution to be small (Worrall 2009) the lobes can be dominated by either relativistic or cold protons/irons, low-energy electrons or magnetic fields. The possibility of deviating from equipartition is to some extent constrained by the absence of detectable X-ray inverse-Compton emission (Croston et al. 2003). Magnetically dominated jets (Li et al. 2006) have been discussed but are disfavored observationally due to expected polarization properties and geometry (Croston and Hardcastle 2014). Initially proton-dominated jets have difficulties in transporting the protons to the lobs (De Young 2006).

Another option is for the jet to gain significant amount of material via entrainment as the jet expands. This model would result in a proton dominated jet on scales $\sim 10 - 100$ kpc. First, entrainment provides the mechanism for FRI to deaccelerate to sub-relativistic speeds on kpc scales (Bicknell 1994). Observed knots in jets can be interpreted as entrained gas clouds (e.g., Hardcastle et al. 2003, 2007a) and entrainment seems highly relevant for accurate kinematic modeling (Laing and Bridle 2014). Additionally, the entrainment model provides a natural explanation for FRII being seemingly in pressure equilibrium with their surrounding material just based on their radiating leptons whereas FRI sources are not. FRII are not observed to significantly interact with the ambient medium before terminating at hotspots such that entrainment seems unlikely. Consequently, both types of jets could initially be comprised of the same magnetized and leptonic material (Croston and Hardcastle 2014). Finally, the last point is in agreement with different morphological types of FRI sources showing a correlation

between degrees of entrainment and emission power. Strong entrainment is correlated with a larger fraction of non-radiating material (Croston et al. 2008).

Origin of radiation

In general, jets and lobes are able to create synchrotron radiation (Section 2.1.5) as well as radiation due to inverse Compton scattering through leptons. As discussed above, it is not clear if only electrons or a combination of electrons and positrons are responsible for the emission. But in the following they are referred to as electrons. In addition protons are likely to be present. The exact composition of the particle component which probably varies spatially and over time is unclear (Harris and Krawczynski 2006).

The emission of FRI sources is normally explained to originate from a single electron population which emits synchrotron emission ranging from radio, optical to X-ray emission in some cases. This idea is supported by significantly steeper spectral indices in the X-ray than in the radio and relative morphologies in radio, optical and radio emission (Harris and Krawczynski 2006). The lifetime of synchrotron emitting electrons in magnetic field with energy density u_B is given by

$$\tau = \frac{3 m_e c}{4 \sigma_\mathrm{T} u_B \gamma}, \tag{2.2}$$

where σ_T describes the Thomson cross section. Thus for synchrotron emission in the X-ray at 1keV the electrons need to have $\gamma \sim 10^7$ and assuming a magnetic field of order 200 μG the lifetime of the electron amounts to 30 years. This time is insufficient for the electrons to move from the nuclei to the observed X-ray emitting regions. Consequently, X-ray-emitting electrons are assumed to be accelerated in situ. Possible mechanisms for this include interaction with a disturbed population of plasma waves or magnetohydrodynamical turbulence (Liu et al. 2017) and/or shock acceleration (e.g., Marcowith et al. 2016). High energy protons ($> 10^{18}$ eV) which have significantly longer lifetimes are theoretically also possible but need high magnetic fields of order $\gtrsim 100$ μG (e.g., Bhattacharyya and Gupta 2016).

In addition, the observed emission could be upscattered CMB photons by highly relativistic electrons ($\gamma \sim 100$), so called *inverse-Compton* (IC) emission (Tavecchio et al. 2000; Celotti et al. 2001). Here, no re-acceleration is necessary as the lifetime of the necessary relativistic electrons suffices. Highly relativistic (beamed) jets are required while maintaining speeds out to these distances that in some cases correspond to rather large jet lengths on the order of $\gtrsim$ Mpc. The absence of theoretically observable gamma-ray emission in some sources challenges the model (Meyer et al. 2017, but Lucchini et al. 2017).

Magnetic fields in jets

Studying the magnetic fields of jet-inflated bubbles reduces the possibility of removing the degeneracy of electron distribution and magnetic field configuration that are responsible for the synchrotron radiation. In the case of Centaurus A γ-ray emission has been observed by *Fermi*. These observations clearly point to an IC origin of the radiation which helps to break the degeneracy of magnetic field strength and electron number density. In this picture, the ultra-relativistic electrons scatter CMB photons. Thus, Abdo et al. (2010) were able to estimate the magnetic field strength of the bubbles to be around 1 μG. For FRII jets a typical of 10 μG has been estimated using IC Compton data in the X-ray. The derived value corresponds to a value below equipartition (Hawley et al. 2015).

Assumptions are still required for the exact high-energy particle composition (Blundell et al. 2006; Godfrey et al. 2009) and the filling factor (of particles and the magnetic field). Simulations

have demonstrated the existence of substructure in the particle distribution (Tregillis et al. 2004) and complexity on larger scales has also been observed (Isobe et al. 2002; Migliori et al. 2007).

IC scattering on CMB photons only depends on the distribution of the electron distribution. This is in contrast to synchrotron radiation which is also sensitive to the structure of the magnetic field. It has been observed that IC maps are much smoother than synchrotron observations. Hence, magnetic fields are assumed to be dynamically sub-dominant as well as turbulent within the bubbles (Hardcastle and Croston 2005). Simulations support this picture (Tregillis et al. 2004; Hardcastle and Krause 2014).

The degree of polarization of synchrotron radiation in radio lobes makes it possible to derive the alignment of magnetic fields in the lobes. FRII jets were found to have magnetic fields aligning with the jet axis. Whereas in FRI jets the magnetic field components tend to be predominantly perpendicular to the jet axis or perpendicular to the jet at the jet center and parallel near the edges. The perpendicular component in the mixed case can be attributed to shocks and the parallel component to shear or oblique shocks (Bridle 1984). Far out from the jet, magnetic fields tend to be always perpendicular to the jet in the lobes (Hawley et al. 2015). This can be explained by an initially disordered field that expands into a lobe. Alternatively, compression of a disordered field yields similar results (Laing 1980).

2.1.4 Proposed heating mechanisms

Connection to AGNs

We observe a clear association of radio galaxies in the center of CCs in contrast to non-CCs. Burns (1990) found that around 70% of CCs host a radio galaxy but only about 20% of non-CCs. More recently Mittal et al. (2009) even found a fraction of 100% for CCs and of 45% for non-CCs. This result is in line with the idea that cooling gas is accreted by the central SMBH leading to the creation of jets, which are mostly observed in the radio. Those jets are then able to inflate large-scale cavities in the center of the cluster. This has been observationally confirmed by the coincidence of X-ray bubbles and radio emission, e.g. in Hydra A (McNamara et al. 2000), Perseus (Fabian et al. 2000), Abell 2052 (Blanton et al. 2001). The bubbles then buoyantly rise in the ICM that is composed of magnetic fields and thermal pressure of the ambient medium. *Chandra* has discovered an array of X-ray cavities outside the cluster center, i.e. Perseus (Fabian et al. 2000), Abell 2597 (McNamara et al. 2001; Clarke et al. 2005), Abell 262 (Clarke et al. 2009), Abell 2052 (Blanton et al. 2009) and Hydra A (Wise et al. 2007).

The significant amount of enthalpy needed to inflate the observed large-scale bubbles must be coupled to the cluster gas to quench star formation and to prevent cooling flows. The correlation between AGN power (related to lobe energy see below) and level of cooling (X-ray radiation) strongly supports this hypothesis (Rafferty et al. 2006) as well as the correlation between central entropy and cavity power (Pfrommer et al. 2012). In addition, AGN timescales (cavity buoyancy timescale) are in general lower or similar to central cooling times in clusters (Rafferty et al. 2008). Including other heating mechanisms like shock, sound waves, thermal conduction and CRs (see Section 2.1.4) the available amount of energy increases even more.

The observed low levels of cool gas in the core of CCs (2.1.2) theoretically challenges any of the models described above since moderate levels of accreeting cold gas by the SMBH are inevitably expected. The contraction can be reconciled with the observations when assuming that the cold gas mixes with hotter gas or high hydrogen column densities absorb the particular X-emission (Werner et al. 2013, 2014).

Energy estimates

Observed bubbles can be used to estimate the energy provided by the radio jet source. To this end, we calculate the work needed to inflate a bubble of volume V and pressure P while fixing the enthalpy H. The enthalpy corresponds to the PV work needed to inflate the bubbles and the internal pressure stabilizing the bubbles, thus

$$H = \frac{1}{\gamma - 1} PV + PV = \frac{\gamma}{\gamma - 1} PV \tag{2.3}$$

The adiabatic index γ then depends on the composition of the bubble. A purely relativistic bubble with $\gamma = 4/3$ would give an energy of $4PV$ whereas a non-relativistic bubble yields $2.5PV$. To estimate the energy input per unit time, we need an injection timescale. Normally, the projected distance between observed outer and inner cavities is used combined with the estimated buoyancy velocity. If outer cavities are not detected in a cluster, approximate values from other clusters are used. Time estimates between single injections of bubbles are at the order of $\sim 10^7$ years (e.g., Perseus McNamara et al. 2000; Abell 262 Clarke et al. 2009; Abell 2052 Blanton et al. 2009).

The cooling luminosity of the gas can be estimated by

$$L_{\text{cool}} = \frac{5}{2} \frac{\dot{M}}{\mu m_p} kT, \tag{2.4}$$

where $\dot{M}$ is the mass deposition rate in the center of the cluster, T is the upper temperature of the gas and μ is the mean molecular weight of the gas such that μm_p gives the average weight of gas particles. Comparing the injected energy rate of the bubbles to the cooling rate estimates, in most cases it has been shown that bubbles supply enough power to offset the cooling in CCs, i.e., in Abell 2052 (Blanton et al. 2001, 2009) with a rate $\sim 3 \times 10^{43}$ erg s^{-1} and in Hydra A (McNamara et al. 2000; Nulsen et al. 2002) with a rate $\sim 3 \times 10^{44}$ erg s^{-1}. In larger studies it has been shown that the energy provided is in principle able to substantially suppress cooling in CCs (Bîrzan et al. 2004; Dunn and Fabian 2006; Bîrzan et al. 2008; Diehl et al. 2008).

The exact mechanism(s) coupling this large reservoir of energy in the lobes to the cluster gas in a volume filling way has not been identified yet. The most discussed mechanisms including possible shortcomings will be discussed in the next few sections.

Weak shocks

Shocks have been observed in CCs. The majority of those show Mach numbers $\mathcal{M}$ of order unity, exceptions include Centaurus A with $\mathcal{M} = 8$ (Kraft et al. 2003) and a shock in NGC 3801 with $\mathcal{M} = 4$ (Croston et al. 2007). Simulations (Li et al. 2016) of a self-regulated idealized cluster have also identified energy dissipation by many small shocks as the main heating mechanism of CCs. Fabian et al. (2003a) and Fabian et al. (2006) find that energy dissipation of viscously damped sound waves with amplitudes consistent with the observed ripples and shock waves in Perseus provide enough energy to offset cooling.

Mathews et al. (2006) found that dissipating shock waves will be able to heat the inner $30-50$ kpc of the cluster. However, if the shocks are not sufficiently weak or rare, the center will be overheated which is not observed. Consequently, the heating contribution from weak shocks can only be secondary. A weak shock will increase the entropy of the medium while passing through the medium, which causes a slight displacement of the gas to higher radii. Thus, most of the residual energy gain from shocks ends in gravitational potential energy (Guo et al. 2017). This happens on relatively short time scales compared to the cooling time such that the long-term

impact is negligible (McNamara and Nulsen 2012). For the case of Hydra A, it has been shown that weak shock heating is not sufficient to halt cooling (David et al. 2001; Nulsen et al. 2007). On the other hand, repeated shock waves at least close to the center of the cluster can have a main contribution. In M87 (Forman et al. 2007) and NGC 5813 (Randall et al. 2011) multiple shocks have been observed with rather high frequencies in between individual outbursts.

Turbulence

Large scale flows created by inflated lobes can become turbulent through the interaction with older remaining cavities in the ICM (Heinz and Churazov 2005) or by interactions with dense clouds (Salomé et al. 2011). Rising cavities lift up low entropy gas from cluster center which should eventually return, creating turbulence in the process (Gitti et al. 2011). Flows around buoyant bubbles can also generate turbulence (Sanders et al. 2011). The dissipation of turbulence would provide another source of heating.

By analyzing deep *Chandra* observation of Perseus and Virgo, Zhuravleva et al. (2014) find the dissipation of turbulence to be sufficient to be the main heating source in CCs. Contrary to this, simulations by Reynolds et al. (2015) clearly show that AGNs drive turbulence on insufficient levels for turbulence to be the main heating mechanism, (see also Yang and Reynolds 2016a). High resolution X-ray measurements of Perseus by *Hitomi* also show low level of turbulence (Hitomi Collaboration et al. 2016) in the cluster. If the turbulence is generated in the vicinity of the bubbles the low value of measured gas velocities does not allow the energy to be dissipated in a volume filling fashion throughout the cluster (Fabian et al. 2017).

Sound waves

In addition to shocks, sound or pressure waves have been discovered in CCs. Especially in Perseus (Fabian et al. 2003a, 2006) ripples with pressure fluctuations of order $5 - 10$ % have been observed without accompanying increases in temperature. Similar observations also exist for Centaurus (Sanders and Fabian 2008) and M87 (Forman et al. 2007). The advantage of sound waves is that they would travel isotropically through the cluster. On the other hand, wave dissipation depends on transport coefficients in contrast to shock dissipation. Thus, the process would be less effective in cooler regions of the cluster. To compensate, more frequent outbursts would be necessary (McNamara and Nulsen 2007). In the light of the slow velocities detected in Perseus by Hitomi results, Fabian et al. (2017) find heating due to the dissipation of sound waves still in agreement with the observations and propose it as a major heating source in CCs.

Bubbel mixing

Hillel and Soker (2016) find the mixing of the hot bubble gas with the surrounding ICM to be the main mechanism in offsetting cooling in CCs in their simulations. Related to this, Yang and Reynolds (2016a) see the combination of bubble mixing and weak shocks as the crucial ingredient to generate entropy. This is distributed in the long term through gentle circulation. Energy exchange could be much slower if the lobes were mostly filled with CRs and magnetic fields (McNamara and Nulsen 2012).

Thermal conduction

Purely thermal conduction from outer hotter regions to the center of the cluster has been proposed as the main heating mechanism (Narayan and Medvedev 2001; Zakamska and Narayan

2003; Voit et al. 2015). The exact value of the transport coefficient, the so called Spitzer value, is however still unknown due to possible suppression effects due to plasma physics processes (Komarov et al. 2016).

Simulations (Ruszkowski and Oh 2011; Yang and Reynolds 2016b) have excluded thermal conduction as the main heating mechanism, even when assuming a maximum Spitzer conductivity. Thermal conduction has recently mainly been used to explain heating at larger radii (Li et al. 2015; Kannan et al. 2016; Jacob and Pfrommer 2017a).

Cosmic ray heating

The presence of a significant non-thermal component in the jet-inflated lobes seems most likely. The observed cavities in the X-ray would be prone to instabilities on short time scales without a stabilizing non-thermal part (Section 2.1.3). In addition estimates of the mass profile in galaxy clusters has pointed to the presence of a non-thermal component in some of them (Voigt and Fabian 2006) and the lack of energy in some bubbles could be alleviated by them partly being filled with a non-thermal relativistic component decreasing their size (Bîrzan et al. 2008).

CRs in the lobes should then be transported out of the lobes into the ICM (Sijacki et al. 2008). Subsequently, CRs can heat the cooling ICM via collisional heating or, for streaming CRs, via the more efficient excitation and dissipation of plasma waves (Enßlin et al. 2011). Guo and Oh (2008) and Jacob and Pfrommer (2017a) show that heating by streaming CRs with the addition of thermal conduction in the outer parts in the cluster is sufficient to offset cooling. The required amount of CRs is in agreement with observations (Jacob and Pfrommer 2017b) such as gamma-ray emission due to neutral pion decay from proton-proton interactions as well as synchrotron radiation from secondary electrons. The exception to this finding are CCs with a radio mini halo (Section 2.2.1). This subset however also shows increased cooling. Thus, these clusters seem to harbor the older population of CRs that partially streamed out of the cluster and could power the radio mini halos. Later cooling will again be hindered by the injection of new CRs through the self-regulated loop connected to the central SMBH.

Limitations of the described models include their reduction of the problem to finding a one-dimensional steady-state solution with a constant injection rate of CRs. Simulations by Ruszkowski et al. (2017) that include MHD and CR streaming (Sharma et al. 2010) obtain a self-regulated feedback cycle with the dominating contribution to heating from CRs. Expanding more on the exact details of the dynamics by CR-filled bubbles in such a context is the topic of this thesis.

2.1.5 Magnetic fields in clusters

The ICM is threaded by magnetic fields. They can been measured via Faraday rotation measurements of background radio galaxies and radio galaxies within clusters (Carilli and Taylor 2002; Kronberg 2003; Govoni and Feretti 2004; Vallée 2004). In the Coma cluster, magnetic field strengths $B \sim \mu$G have been infered (Kronberg 2003). In cool core cluster values of magnetic field are at the order of tens of microgauss (Clarke et al. 2001; Bonafede et al. 2010). The origin of magnetic fields in clusters is unclear as they may have been created by radio galaxies or quasars, or primordial magnetic fields may have been amplified to the current values by magnetic dynamo processes that are driven by gas turbulence and/or compression (Carilli and Taylor 2002).

Origin

A good approximation of the magnetic diffusion timescale in galaxy clusters is given by $\tau \sim 10^{36} \left(\frac{L}{10\mathrm{kpc}}\right)^2$ years where L is scale of magnetic fluctuations (Carilli and Taylor 2002). Thus, if magnetic fields are created or amplified only anomalous resistive processes like reconnection via plasma wave generation in shocks can annihilate them. Many possible mechanisms for the creation and or amplification of magnetic fields have been proposed but no definitive answer has yet been found.

Astrophysical magnetic fields may have been created by the so called Biermann battery (Biermann and Schlüter 1950). The mechanism is based on the separation of electrons and protons and requires a baroclinic term, i.e., $\nabla n_\mathrm{e} \times \nabla P_\mathrm{e} \neq 0$. This creates a current and an electric field to restore equilibrium. Magnetic fields emerge due to the symbiotic nature of electromagnetic fields. This separation in charge can be obtained due to the large differences in mass. One phenomenon with a mass dependence would be photon drag which affects electrons more heavily than protons.

Alternatively, primordial weak seed fields may have been created during phase-transitions in the early universe. Local charge separation might have happened during the quark-hadron or the electroweak transition (Baym et al. 1996). During the period of inflation, quantum magnetic field fluctuations might have been amplified via super-adiabatic amplification (Turner and Widrow 1988). These fields would have field strengths of order $\sim 10^{-21}$ G. The survivability of magnetic field on comoving scales $\leq$ a few Mpc is however unclear due to magnetic and photon diffusion during the radiation era (Battaner and Lesch 2000). Observations of the anisotropy in the CMB and inhomogeneities in the matter distribution measured by faraday rotation of distant quasars have been able to put upper limits on the magnetic field at $< 5 \times 10^{-9}$ G and $< 10^{-9} - 10^{-8}$ G, respectively (Govoni and Feretti 2004).

Possibly, magnetic fields were generated at later times. The Biermann battery effect might have been rather strong during the epoch of re-ionization (Gnedin et al. 2000) or the fields might have been created during the epoch of structure formation (Kulsrud et al. 1997).

Lastly, magnetic fields could originate from member galaxies of the cluster during its formation. Galactic winds launched from galaxies, active galaxies or starburst galaxies would all be able to eject magnetic fields into the ICM. In galaxies magnetic fields could be created by the Biermann battery in early stars, which inject them into the ISM by stellar outflows. Otherwise primordial galactic magnetic fields may have been enhanced through adiabatic compression during the collapse of the protogalactic cloud up to 10^{-19} G (Govoni and Feretti 2004). The metallicity of the ICM is around 30% which directly supports the injection of material from galaxies (Carilli and Taylor 2002). However observed magnetic field values in galaxy clusters can be of the order or even higher than the field strengths in galaxies (Grasso and Rubinstein 2000).

Independent of the exact seeding or injection mechanism, the strength of these magnetic fields would still be lower than observed values in the ICM, thus some form of dynamo is required that enhances the magnetic field strength. A dynamo is based on electrically conducting material moving in a magnetic field in order to induce currents maintaining and amplifying the original magnetic field (Govoni and Feretti 2004). To this end turbulence is needed which on galactic scales could be provided by supernovae, stellar winds or hydromagnetic instabilities. On cluster scales during the period of structure formation mergers generate shocks, bulk flows and turbulence. The former two are able to enhance the magnetic field through compression whereas turbulence might be responsible for significant nonlinear amplification. The last point could be shown in cosmological simulations where fields with insignificant field strengths were enhanced from $\sim 10^{-9}$ G to $\sim 10^{-6}$ G (Govoni and Feretti 2004).

Faraday rotation

Polarized radio radiation changes its angle of polarization in magnetized plasmas due to the so-called Faraday rotation (Carilli and Taylor 2002; Vallée 2004). The plasma forces the electrons to gyrate in preferred directions, thereby changing the index of refraction for left- vs right-circularly polarized radiation. This leads to a phase shift of the left- and right-polarized components as $\Delta\chi = \mathrm{RM}\lambda^2$, where $\Delta\chi$ defines the change in the polarization angle, λ is the wavelength of the radiation and RM is the rotation measure. The rotation measure is sensitive to the electron density and magnetic field strength along the line of sight via

$$\mathrm{RM} = 812 \int_0^L n_\mathrm{e}(x) B_{\mu\mathrm{G}}(x) dx, \tag{2.5}$$

where $B_{\mu\mathrm{G}}$ corresponds to the magnetic field strength in μG, n_e describes the electron density in the plasma per cm^3, RM is given in units of rad m^{-2}. The integral is taken from the source to the observer along the line of sight. The effect can be used to constrain field strengths of galaxies and galaxy clusters. This is done using radio telescopes ($\chi \propto \lambda^2$) measurements at different wavelengths. However, assumptions on the spatial distribution of the electron density and the magnetic field within the cluster but also in the foreground (between galaxy clusters, in our Galaxy) have to be made. Assuming a constant magnetic field in the cluster, minimum magnetic field strengths of the order of 5 to 10 μG have been determined in cool core clusters. Those values are reduced by a factor of two in non-cool core clusters (Carilli and Taylor 2002).

Synchrotron radiation

An electron in a magnetized medium with energy $\epsilon = \gamma m_e c^2$, where γ is the relativistic Lorentz factor, will be forced to gyrate around a magnetic field line due to the Lorentz force. It will emit synchrotron radiation in the direction of travel in a cone with half-angle $\simeq \gamma^{-1}$. The spectrum of the radiation will peak at the so called critical frequency ν_c given by (Rybicki and Lightman 1979)

$$\nu_c = \frac{3q_\mathrm{e}}{4\pi m_\mathrm{e} c} B\gamma^2 \sin\theta \simeq 4.2 \times 10^6 \; B\gamma^2 \sin\theta, \tag{2.6}$$

where θ is the angle between magnetic field and electron velocity.

The emitted synchrotron power by an electron is given by (Rybicki and Lightman 1979)

$$-\frac{d\epsilon}{dt} = \frac{4\sigma_\mathrm{T} c}{3} \; \beta^2\gamma^2 U_B \simeq 1.06 \times 10^{-15} \, B^2\gamma^2 \sin^2\theta, \tag{2.7}$$

where σ_T is the Thomson cross section, U_B is the magnetic energy density and the last step holds for relativistic electrons with $\beta \simeq 1$.

The particle density $N(\epsilon)$ of an electron population following a power law in energy is

$$N(\epsilon)d\epsilon = N_0 \epsilon^{-\delta} d\epsilon \tag{2.8}$$

The principle of detailed balance states that to every emission process there is a corresponding absorption process. In the case of synchrotron radiation this process is called *synchrotron self-absorption*. The process becomes relevant when the brightness temperature of the source becomes of the same order as the kinetic energy of the electrons which is not important in galaxy clusters. This effect can in some environments become relevant at low frequencies where the optically thick medium now emits at the intensity

$$S(\nu) \propto \nu^{+5/2} \tag{2.9}$$

Thus, its slope is independent of the initial electron distribution. In the optically thin regime the intensity varies as

$$S(\nu) \propto \nu^{-\alpha}, \tag{2.10}$$

where $\alpha = (\delta - 1)/2$ is the spectral index.

Synchrotron emission is by nature polarized. In the optically thin regime the degree of intrinsic linear polarization for a homogeneous and isotropic relativistic electron distribution as above is given by

$$P_{\text{int}} = \frac{3\delta + 3}{3\delta + 7} \tag{2.11}$$

polarized in the direction perpendicular to the projection of the magnetic field on the plane of the sky. Typical values for δ yield a high degree of polarization at $\sim 75 - 80\%$ (Govoni and Feretti 2004). In the optically thick case, the polarization in the direction parallel to the projected magnetic field gives

$$P_{\text{int}} = \frac{3}{6\delta + 13} \tag{2.12}$$

However in reality far smaller degrees of polarization are measured. This is partially due to the more random magnetic field structure that varies significantly along the line of sight. In addition, superpositions of Faraday rotation at different positions along the line of sight and at any foreground screens contaminate the degree of polarization (Fletcher 2010).

Equipartition

Observed synchrotron emission in radio halos (Section 2.2.1) can be used to estimate the magnetic field strength in the ICM. As discussed, when using measured synchrotron emission, the magnetic field strength cannot unambiguously be separated from the energy of the radiating electrons. Thus, the minimum energy assumption is made, which means that the total energy content is minimized to match observed synchrotron fluxes. The relevant energies here are given by the energy in protons U_p, energy in electrons U_e and the magnetic field energy U_B. The total energy can then be expressed as

$$U_{\text{tot}} = U_{\text{e}} + U_p + U_B \tag{2.13}$$

Assuming the energy in protons is just a constant fraction k of the electron energy, one obtains

$$U_p = kU_{\text{e}} \tag{2.14}$$

The magnetic field energy can be described up to a volume filling fraction ΦV as

$$U_B = \frac{B^2}{8\pi}\Phi V \tag{2.15}$$

Assuming a power law distribution in electrons one can use the synchrotron luminosity of the electrons to express U_{tot} in terms of the magnetic field strength as (Carilli and Taylor 2002)

$$U_{\text{tot}} = A(\alpha, \nu_1, \nu_2, k)B^{-3/2} + \frac{B^2}{8\pi}\Phi V, \tag{2.16}$$

where the coefficient A depends on α, k and the spectral bin from frequency ν_1 to ν_2 of the observational data. Minimizing $U_{\text{tot}}(B)$ with regard to B gives a similar result as assuming equipartition between the energy in particles and the energy in the magnetic field.

The exact value of k is rather uncertain as it strongly depends on the exact mechanism to produce relativistic electrons. In addition, the volume filling fraction is poorly constrained as well as the extent of the source itself along the line of sight.

Observed strengths and spectral shape

For Hydra A (CC cluster), Kuchar and Enßlin (2011) find the magnetic field strength and magnetic power spectrum $\omega(k) \propto k^{\gamma}$ (with spectral index γ) through fitting their model to Faraday rotation measurements. They assume a double beta profile for the electron number density

$$n_e(x) = \left[n_{\mathrm{e1}}^2 \left(1 + \left(\frac{r}{r_{c1}}\right)^2\right)^{-3\beta} + n_{\mathrm{e2}}^2 \left(1 + \left(\frac{r}{r_{c2}}\right)^2\right)^{-3\beta} \right]^{1/2} \tag{2.17}$$

as is common for CC clusters (Vogt and Enßlin 2005). In addition, they assume a dependence on $n_e(x)$ for the magnetic field of the form

$$\langle B^2(\boldsymbol{x}) \rangle = B_0^2 (n_{\mathrm{e}}(\boldsymbol{x})/n_0)^{2\alpha} \tag{2.18}$$

and statistical isotropy.

Their resulting power law ranges for $\alpha = 1$ from scales of 0.3 kpc to about 8 kpc. They do not detect a significant cut-off scale at large scales. Smaller scales are not accessible due to the FWHM of the beam. Their spectral index $\gamma = 1.73$ is consistent with a Kolmogorov spectrum ($\gamma = 1.67$). A Kolmogorov spectrum in general suggests that large scale turbulence drives the magnetic dynamo in the cluster. Extrapolating their model, they measure a central magnetic field strength of $B_0 = 20 - 80\ \mu$G. They are able to directly measure the magnetic field strength at a distance of 50 kpc from the cluster center as $B_{50} = 10 - 30\ \mu$G.

The Perseus CC cluster seems to host a turbulent magnetic field. Observations (Schuecker et al. 2004) as well as simulations find the magnetic field power spectrum of the Coma cluster to to be consistent with a Kolmogorov power spectrum. Bonafede et al. (2010) use Faraday rotation measurements to constrain the magnetic field strength and optimize parameters for the power spectrum of the magnetic field. They use data from seven distinct radio sources and are thereby able to probe the magnetic field on larger scales. Assuming a Kolmogorov power spectrum, they find that the data is best reproduced with a model where the maximum fluctuations are on a scale of 34 kpc and the minimum fluctuations on a scale of 2 kpc. They also assume a magnetic field dependence as given in Equation 2.18. For the magnetic field normalization they find $B_0 = 3.9 - 5.4$ and index $\alpha = 0.4 - 0.7$. The definition of the plasma beta factor is

$$\beta_B = \frac{P_u}{P_B} = \frac{nkT}{B^2/(8\pi)} \tag{2.19}$$

Hence, the inferred magnetic profile by Bonafede et al. (2010) is consistent with a constant (isothermal) plasma beta factor.

A more vivid example for the index α is given in the following. Assuming a cylinder with magnetic field B, cross-sectional area A and particle density n, one sees that the particle flux nA and magnetic flux BA are conserved (ideal MHD). We have

$$\frac{B}{n} = \text{constant}, \tag{2.20}$$

which is independent of A. Consequently, perpendicular contraction or expansion does not alter the relation. Assuming a parallel contraction or expansion, A stays constant, thus $B =$ constant in this case. For isotropic contraction or expansion the particle number is conserved $nr^3 =$ constant as well as magnetic flux Br^2. We obtain

$$\frac{B}{n^{2/3}} = \text{constant} \tag{2.21}$$

In summary:

$$\frac{B}{\rho^i} = \text{constant}; \quad i = \begin{cases} 1 & \text{perpendicular contraction/expansion} \\ 0 & \text{parallel contraction/expansion} \\ \frac{2}{3} & \text{isotropical contraction/expansion} \end{cases} \tag{2.22}$$

The case of $i = 0.5$ can thus be seen as an intermediate case of parallel and perpendicular contraction which is a reasonable assumption for the ICM.

Draping

The process of draping describes the amplification of magnetic fields and their corresponding tension on the bounding layer perpendicular to the direction of motion of an object while the object moves at super-Alfvénic speeds through a magnetized medium with magnetic field strength B_0. Bubbles inflated by AGN jets might be affected by this process (Ruszkowski et al. 2007; Dursi and Pfrommer 2008). The process results in a slow down of the object and makes it more resilient against Kelvin-Helmholtz and Rayleigh-Taylor instabilities. Thus, it should have a significant impact on the timescale and life time of bubbles inflated by AGN jets discussed in this thesis. This effect in the environment of galaxy clusters has been studied previously in the context of cold fronts. These sharp transitions in the ICM are relatively long lived. However, enhanced magnetic fields along their edges might support the medium against thermal conduction and hydrodynamical motions (Asai et al. 2007; Lyutikov 2006; Vikhlinin et al. 2001). In addition, the transport of CRs should also be inhibited across draped magnetic field layers.

Dursi and Pfrommer (2008) set up an (over-dense) spherical bullet with radius R and subsonic speed u in a box with a homogeneous magnetic field perpendicular to the direction of motion of the projectile and a constant density and pressure. They find the critical value for draping to saturate to be $\alpha \approx 2$ where α describes the ratio between the maximum magnetic pressure and incoming ram pressure at the stagnation line as

$$\alpha = \frac{B^2/(8\pi)}{\rho u^2/2} \tag{2.23}$$

Here, B describes the magnetic field strength at the boundary layer, ρ the density of the ambient medium and there is a slight modification represented by α whose origin has not been fully understood yet (Pfrommer and Dursi 2010).

For $\alpha \ll 1$ the ram pressure dominates and the bullet passes uninhibited through the medium as perpendicular field lines are just swept over the object. If the magnetic field dominates ($\alpha > 1$) magnetic tension becomes too strong and the object is slowed down. In two dimensions the ever-increasing tension from the swept up material is at some point able to even reverse the direction of travel of the object (Figure 3/4 Asai et al. 2005; Figure 6 Dursi and Pfrommer 2008) as the field lines have no possibility of sliding over the object in the third dimension.

Using Equation 2.23 the thickness of the resulting draping layer can be derived. The magnetic field at the boundary layer of a sphere at the stagnation line can shown to be

$$B \simeq B_0 \left[1 - \left(\frac{R}{R+s}\right)^3\right]^{-\frac{1}{2}} \simeq B_0 \sqrt{\frac{R}{3s}}, \tag{2.24}$$

where s describes the distance from the leading edge along the stagnation line (Pfrommer and Dursi 2010; Lyutikov 2006). The last result holds for $s/R \ll 1$. It is straightforward to show that the thickness of the draping layer at the stagnation line for a spherical object is given by

$$s \simeq \frac{1}{3\alpha \mathcal{M}_A^2} R \simeq \frac{2}{3\alpha\beta\gamma\mathcal{M}^2} R, \tag{2.25}$$

where $\mathcal{M}_\mathrm{A} = u/u_\mathrm{A} = \mathcal{M}\sqrt{\beta\gamma/2}$ is the Alfén Mach number, $M = u/c_\mathrm{s} = u/\sqrt{\gamma P/\rho}$ is the hydrodynamic Mach number and $\beta = P/P_B = P/(B^2/(8\pi))$ describes the plasma beta factor of the surrounding medium. To first order the draping layer should be established when the object has been able to sweep up enough field lines to cover half its surface area with magnetic field lines. Magnetic draping describes the sweeping up of magnetic fields at its surface. The magnetic field lines are slightly compressed and stretch accordingly. Consequently, it requires the field lines not to be considerably smaller than the object as they otherwise would not stay attached to the object. The sweeping procedure should have completed at half the crossing time of the object $t_\mathrm{c}/2$ with $t_\mathrm{c} = 2R/u$. Thus, the timescale of establishing the draping layer is given by:

$$t = \frac{R}{u} \tag{2.26}$$

Pfrommer and Dursi (2010) find empirically that around five galactic crossing times are necessary in more realistic scenarios.

As discussed above draping is only possible for magnetic field lines with a large enough coherence length to wrap around the object. To estimate the minimum magnetic field coherence length one can look at a simplified model of the problem assuming a perfect potential flow. This is basically valid in the upper half of the object in the direction of motion but due to the significant generation of vorticity not in the lower hemisphere. From the analytical solution of the model a critical impact parameter can be derived of the streamline to the stagnation line that is tangent to the outermost boundary layer. The critical impact parameter p_cr can shown to be

$$p_\mathrm{cr} = \frac{R}{\sqrt{\alpha\beta\gamma\mathcal{M}}}, \tag{2.27}$$

which, even though strictly only valid for a perfect potential flow of a sphere, is in good agreement with simulations (Pfrommer and Dursi 2010). Magnetic fields with coherence length smaller than $2p_\mathrm{cr}$ cannot completely encase the objects working surface in the flow. They are not be able to attach to its surface and, thus, do not contribute to the draping layer. This constrains the ratio of the magnetic coherence length λ_B with the radius of the object to

$$\frac{\lambda_B}{2R} = \frac{1}{\sqrt{\alpha\beta\gamma\mathcal{M}^2}} \tag{2.28}$$

In a more general model R can also describe the radius of curvature of the object.

2.2 Cosmic rays

We are interested in CRs in clusters, first we review important aspects of CR physics that were obtained in studies of Galactic CRs. The majority of particles in the universe are thermal particles. There is also a non-thermal particle component, so called *cosmic rays* (CR) which can span kinetic energies from $10^0 - 10^{21}$ eV. Only $1 - 2\%$ of CRs are electrons. The thermal electrons that dominate by orders of magnitude can easily cancel CR proton currents.

To constrain the confinement and propagation time of CRs in the Galaxy one can study the measured composition of CRs. The abundance of r-process elements (supernovae (SNe) ejecta) in CRs is close to the interstellar value. On the other hand there is a strong overabundance (by 5-7 orders of magnitude at ~ 1 GeV) of light elements (Fermi 1949) like He, Li, Be and B. These abundances can be explained if CRs passed through $3 - 6$ gcm^{-2} of ISM to produce spallation

products (Zweibel 2013). Using transport equations that model the spallation processes and account for life times of resulting isotopes (Strong et al. 2007), one can show that CRs stay in the galactic disk for $1 - 2 \times 10^7$ years at 1 GeV and less with increasing energy.

This hints at an efficient confinement mechanism as the CR lifetime in the disk is 3-4 orders of magnitude larger than the light travel time through the Galaxy. However the obvious contender, magnetic fields, cannot be the only reason for confinement as they would yield an energy dependence on the confinement time. Also the acceleration process itself seems to happen on much smaller timescales than the CR lifetime. Otherwise one would expect the longest-lived CRs to have the highest energy whereas the opposite is actually observed.

Observations on the isotropy of CRs at ~ 1 GeV are hindered due to strong pollution from the solar wind (Webber 1998). However data from CRs with higher energies indicate that CRs are isotropic to a few parts in 10^4 with the anisotropy slowly increasing for higher energies. Some local sources might be present that slightly modify the picture, however the main idea remains valid. CRs are accelerated on short timescales and propagate diffusively through the interstellar medium. Using basic random walk approximations on can show that the ratio of the mean free path λ of the CR to the size of the system is on the same order as the ratio of free streaming time to confinement time. The mean free path for CRs at ~ 1 GeV is a few pc such that the diffusion coefficient is of order 10^{28-29} cm^{2}s^{-1}. More insights into this, from which also the treatment of CRs as a fluid will follow, will be given in Section 2.2.2 after the discussion of some CR sources in galaxy clusters.

2.2.1 Observations in galaxy clusters

Observing galaxy clusters in the radio spectrum revealed the existence of peculiar objects within galaxy clusters. Large-scale diffuse radio emission has been observed in a variety of clusters, so called *radio halos* and smaller so called *radio mini halos*. In addition more irregular elongated objects, *radio relics*, have been identified at the cluster periphery. They generally all show very steep spectra. Radio relics however show much higher degrees of polarization compared to halos (Feretti et al. 2012). Due to their polarization their common origin seems to be synchrotron radiation, which proves the prevalence of magnetic fields and at least CR electrons in galaxy clusters. In the Galaxy, the CR proton energy density even outnumbers the CR electron density by two orders of magnitude suggesting the existence of CR protons in galaxy clusters (Enßlin et al. 2005). A brief overview of these radio phenomena will be given in the following.

Radio Halos

A subset of galaxy clusters host diffuse synchrotron radio-emitting structures. The large Mpc-size subclass is comprised of *giant radio halos* whereas the smaller-scale feature is referred to as *minihalo* (Feretti et al. 2012). Radio mini halos are predominantly found in cool core clusters whereas giant radio halos are hosted by unrelaxed clusters (Yuan et al. 2015) that very rarely (Sommer et al. 2017) posses a cool core (Rossetti et al. 2013). Radio halos show steep spectral indices ($\alpha > 1$, equation 2.10) and low surface brightnesses. Their centroids seem to align with the cluster center as seen in the X-ray (Carilli and Taylor 2002).

The two main models for explaining the radio emission are based on fossil or secondary electrons that are re-accelerated in the volume of the cluster (Brunetti and Lazarian 2011; Pinzke et al. 2015) or secondary electrons produced throughout the cluster by (hadronic) proton-proton collisions (Enßlin et al. 2011).

As giant radio halos are preferentially observed in clusters that show merging signatures, it is reasonable to assume that mergers supply the re-acceleration energy for the electrons (Feretti et al. 2012). This model is strengthened by the correlation between the spectral index and

cluster temperature. Hotter halos (more recent mergers) seem to host radio halos with flatter spectrum indicating more recent acceleration processes (e.g., Feretti et al. 2004; Cassano et al. 2008).

The clusters X-ray luminosity ($0.1 - 2.4$ keV) and its giant halo radio power at 1.4 GHz are only correlated in merging galaxy clusters (Feretti et al. 2012). In addition, spatial correlations between X-ray and radio emission have been found for a number of regular giant radio halos (e.g., Feretti et al. 2001; Giacintucci et al. 2005). These findings strongly support the merger-driven origin of radio halos. More irregular radio systems show significant offsets between X-ray and radio emission (Feretti et al. 2010) possibly due to distinct fluctuations in the magnetic field structure of the cluster (Vacca et al. 2010).

Giant halos in seemingly X-ray deficient clusters in relation to their radio luminosity (Giovannini et al. 2009, 2011) and clearly dynamically disturbed system without significant radio detection (Cassano et al. 2010; Russell et al. 2011) challenge the outlined picture above. To resolve these findings a new type of mergers has been suggested (Feretti et al. 2010).

Mini Halos

Some cool core clusters show diffuse radio emission on scales of $\sim$ 100 kpc up to $\sim$ 500 kpc from the central radio galaxy, which is clearly not related to any X-ray cavity. These features are called radio minihalos. The flux density of minihalos $S_\nu \propto \nu^{-\alpha_{\rm radio}}$ at frequency ν with radio spectral index $\alpha_{\rm radio}$ drops rather steeply with $\alpha_{\rm radio} > 1$. The source of this diffuse emission with a steep spectrum seems to require magnetic fields and ultra relativistic electrons distributed throughout a large fraction of the cooling cluster core (Brunetti and Jones 2014).

In contrast to giant radio halos, minihalos have been almost exclusively found at the center of CCs (Kale et al. 2015; Yuan et al. 2015; Giacintucci et al. 2017). The emission is centered around the central active radio galaxy that usually exists in CCs (Mittal et al. 2009) and extends out to high distances $\sim 50 - 300$ pc, thereby usually filling the cooling region. The minihalos do not show any clear structure like extended radio galaxies with lobes and jets. Thus, they also differ from old remnants of radio galaxies at the center of some clusters. These remnants show even steeper radio spectra ($\alpha_{\rm radio} \gtrsim 2$) and a modified version of the lobe structure can still be visible (Saikia and Jamrozy 2009; Murgia et al. 2011, 2012).

Cold X-ray fronts that surround the radio minihalos are observed (Mazzotta and Giacintucci 2008; Giacintucci et al. 2014a,b). They seem to be the result of sloshing processes of the cool gas in the central core region (Ascasibar and Markevitch 2006). One interpretation of these observations is that minihalos are formed by relativistic electrons that are reaccelerated at turbulent magnetic fields, which are created by the sloshing effect of a minor merger within the cluster (Mazzotta and Giacintucci 2008; ZuHone et al. 2013; Giacintucci et al. 2014a). Numerical simulations confirm that sloshing motions are able to amplify magnetic fields and create turbulence in a region bordered by cold fronts where diffuse radio emission can be generated (ZuHone et al. 2013, 2016). The X-ray observations by the *Hitomi* satellite (Hitomi Collaboration et al. 2016) show levels of turbulence sufficient for the described model (Giacintucci et al. 2017).

On the other hand, there is also a hadronic model trying to explain the origin of the minihalos (Pfrommer and Enßlin 2004; Enßlin et al. 2011; Jacob and Pfrommer 2017b). Here, CR protons inelastically interact with thermal protons forming pions which eventually decay into electrons and positrons. Both turbulence and CR protons (Section 2.1.4) could play a vital role in heating CCs, such that a direct connection seems evident (Fujita and Ohira 2013; Bravi et al. 2016; Jacob and Pfrommer 2017b). Further support for this hypothesis is given by Giacintucci et al. (2017). They are able to detect 12 minihalos within their sample of 15 massive clusters

($M_{500} > 6 \times 10^{14} M_{\odot}$) where they find an increased probability of detecting minihalos in hotter CCs in agreement with Giacintucci et al. (2014b).

In contrast to radio halos, radio mini halos show a wide range in radio emissivity in some cases like Perseus their emissivity is even two orders of the magnitude higher than that of radio halos (Enßlin et al. 2011). In addition, a small correlation between the mini halo and the cD radio power has been found (Govoni et al. 2009). Both of which hints towards a connection of radio mini halos partly to the local intergalactic medium and partly to the AGN activity.

Radio relics

First, radio relics discussed here should not be confused with old bubbles (AGN relics) in the ICM previously inflated by an AGN. Radio relics discussed here are similarly to radio halos large ($\gtrsim 1$ Mpc), steep spectrum ($\alpha \gtrsim 1$) diffuse low surface brightness radio sources. Relics are seen in the outskirts of clusters of merging and relaxed galaxy clusters. They are strongly polarized ($\sim 20 - 30\%$) (Feretti et al. 2012). They are a good indicator for μG magnetic fields at the outskirts of clusters and hint towards shock accelerated relativstic electrons at large distances from the cluster center (Brüggen et al. 2011; Pinzke et al. 2013).

Relics show an elongation roughly perpendicular to the direction to the cluster center. Relics have been detected in merging as well as CCs clusters. This points towards their formation being related to major mergers and minor or off-axis mergers. Those findings and X-ray observations of radio relics (e.g., Finoguenov et al. 2010) suggest a profound connection between merger shocks and radio relics (Brüggen et al. 2012). Hydrodynamical cosmological simulations are also able to reproduce the main observed features of radio relics (e.g., Nuza et al. 2017).

However, not all relics can be explained with this model. Two distinct populations of radio relics differ in morphology. There are roundish as well as elongated relics. Elongated relics seem to be related to the ICM and the result of merger shocks then (usually) referred to as *gischt* (Kempner et al. 2004). They show strong ordered polarizations and are clearly related to large-scale shocks ($\mathcal{M} = 1 - 3$). Consequently, their polarisation, morphology, location and spectral index are in good agreement with shock accelerated particles and compressed magnetic fields which causes the observed synchrotron radiation (van Weeren et al. 2011). In addition, expected double radio relics on both sides of the merged cluster with extensions perpendicular to the merger axis have been detected in many systems (i.e., Abell 3667, see Rottgering et al. 1997, Johnston-Hollitt 2003; in Abell 3376, see Bagchi et al. 2006).

There is another class of roundish shaped relics which are termed *phoenix* (Kempner et al. 2004). They are also detected off center close (~ 0.4 Mpc) to the largest central galaxy but show a more regular roundish shape. Interpreting them as elongated relics, seen from the sides, is statistically unlikely (Feretti et al. 2012). Their sizes are in the range $\lesssim 100 - 350$ kpc and show filamentary structure (Govoni et al. 2001). Their close proximity to an AGN source leads to them being interpreted as re-energized (from shock waves) radio lobes (Enßlin and Gopal-Krishna 2001; Enßlin and Brüggen 2001). Alternativley, they could be powered by an radio-emitting lobe created by CRs lacked from a X-ray cavity inflated by the central AGN (Mathews and Brighenti 2008). Some exceptionally distant roundish relics have been found in Abell 1664 (Govoni et al. 2001) and Abell 548b (with two relics on the same side of the AGN) (Feretti et al. 2006; Solovyeva et al. 2008), which does not agree well with the model.

2.2.2 Fluid description

Vlasov Equation

In general CRs can be described by a distribution function $f(\boldsymbol{x}, \boldsymbol{p}, t)$, the probability for a CR to be at position $\boldsymbol{x}$ with momentum $\boldsymbol{p}$ at time t. The distribution function follows the Boltzmann equation

$$\frac{\partial f}{\partial t} + \boldsymbol{v} \cdot \nabla f + \frac{d\boldsymbol{p}}{dt} \cdot \nabla_{\mathbf{p}} f = \left.\frac{\partial f}{\partial t}\right|_c + S(\boldsymbol{x}, \boldsymbol{p}, t), \tag{2.29}$$

where $\boldsymbol{v}$ is the velocity of the CRs and $\partial f/\partial t|_c$ describes collisional processes like spallation and pion production. CR propagation codes like GALPROP (Strong and Moskalenko 1998) use this term to compare propagation models with observations or determine the radiative emission from CRs. The term $S(\boldsymbol{x}, \boldsymbol{p}, t)$ characterizes the sources of CRs. Even if we had knowledge of the exact magnetic field structure of the Galaxy, it would still be unfeasible to solve Equation 2.29 by direct integration, as gyro radii of GeV protons are 9-10 orders of magnitude smaller than the size of the system. Consequently, approximations are necessary.

For the relevant radiation processes in galaxy clusters the full treatment of the spallation processes is not relevant. When excluding sources for the CRs one can rewrite Equation 2.29 in the following form (assuming isotropy in momentum space)

$$\frac{\partial f}{\partial t} + \boldsymbol{v} \cdot \nabla f + \frac{dp}{dt} \cdot \nabla_p f = 0 \tag{2.30}$$

This is the so called *Vlasov equation* which is valid for all collisionless systems and describes the conservation of phase space density ($df/dt = 0$). For the Boltzmann/Vlasov equation to be applicable, interactions on the microscopic scale of the particles λ have to be on scales much smaller than the scale l we are interested in. In turn l has to be smaller than the size of the system L. The last point is quite clearly fulfilled. The condition $\lambda \ll l$ might seem problematic as Coulomb interactions in the relatively dense ISM between CRs and thermal particles have a mean free path of $\sim 10^{10}$ pc. However, CRs constantly pitch angle scatter on magnetic fluctuations so called *Alfvénic waves*, which causes them to interact without collisions on much smaller scales. The crucial last point will be explained in more detail in the next section.

Pitch angle scattering

As discussed in the introduction of this subsection, the CR confinement time and CR isotropy point towards a confinement mechanism of CRs which is not primarily related to gyration around magnetic fields nor to the timescale of acceleration mechanisms but due to the influence of plasma effects on CRs. It becomes necessary to study how CRs interact with small scale magnetic fluctuations δB on a uniform background magnetic field B_0. The transverse magnetic field component of the fluctuation $\delta B_\perp$ exerts a Lorentz force on the CR. Assuming the Lorentz force decreases the parallel velocity component $v_\parallel$ (with respect to the the magnetic field) of the CR, the perpendicular component $v_\perp$ will increase as (time-independent) magnetic fields leave the energy of the particle invariant.

Consequently, the pitch angle of the particle $\cos\theta = v_\parallel/v$ changes. One refers to this form of interaction as *pitch angle scattering*. For pitch angle scattering to be most effective, the scale of the magnetic fluctuations $r_{\delta B}$ should be on the order of the gyration radius of the CR r_G. If $r_G \ll r_{\delta B}$ the CR just gyrates around the slowly evolving magnetic field flucuation. On the other hand, if $r_G \gg r_{\delta B}$ the lorentz force varies on such small scales that it averages out and the CR effectively does not get scattered.

In a more quantitative sense the two relevant resonances are the Landau resonance

$$\omega - k_{\parallel} v_{\parallel} = 0 \tag{2.31}$$

which is related to magnetosonic waves, and the gyroresonances

$$\omega - k_{\parallel} v_{\parallel} = \pm n\Omega \qquad n \in \mathbb{N}, \tag{2.32}$$

where subscript "$\parallel$" refers to parallel direction with respect to the magnetic field, ω and $k_{\parallel}$ describe the frequency and parallel wavenumber of the fluctuation, $v_{\parallel}$ and Ω are the parallel CR velocity and relativistic gyro-frequency ($\Omega = \Omega_0/\gamma = eB_0/(\gamma m_p c)$). The $\pm$ sign corresponds to left and right polarization, respectively. One can see that the Landau resonance describes the special case for the gyro-resonance when $n = 0$.

For MHD fluctuations one expects $\omega \sim k v_A$ while $v \sim c$. Thus, we get for the Landau condition either

$$\frac{k_{\parallel}}{k} \sim \frac{v_A}{v_{\parallel}} \sim \frac{v_A}{c} \ll 1 \tag{2.33}$$

for $v_{\parallel} \sim c$ or alternatively $\mu \equiv v_{\parallel}/v \ll 1$. Similarly one gets $k_{\parallel} v_{\parallel} \sim n\Omega$, i.e. CR gyro-radius and gyro-resonant fluctuations are in resonance.

Before looking at the exact source of the magnetic fluctuations, let us discuss how the pitch angle scattering influences CR transport properties described in the Vlasov equation. Energy is conserved in the frame of the wave. However, in the frame of the plasma energy is transfered to the waves, i.e., a diffusion in momentum space is observed (Kennel and Engelmann 1966). Quantitatively this can be seen when investigating the influence of the electromagnetic fields of Alfvén waves on a CR distribution using the Vlasov equation. The resulting expression can be simplified by acknowledging that scattering in μ dominates over scattering in p at the order of $(c/v_A)^2$. Ensemble averaging of all sets of waves, we obtain (Kulsrud and Pearce 1969)

$$\frac{\partial f}{\partial t} + v_z \frac{\partial f}{\partial z} = \frac{\partial}{\partial \mu}\left(\nu(\mu, p)\frac{(1-\mu^2)}{2}\frac{\partial f}{\partial \mu}\right) \tag{2.34}$$

for a background field $B_0 = B_z \hat{z}$. The scattering frequency $\nu(\mu, p)$ is given by

$$\nu(\mu, p) = \frac{\pi}{4}\Omega \frac{k\mathcal{E}(k)}{B_0^2/8\pi} \tag{2.35}$$

where $k = \Omega/(\mu\nu)$ is the gyroresonance condition and $k\mathcal{E}(k)$ is the wave energy at wavenmumber k. The general form of a diffusion term can clearly be recognized from the right-hand side of Equation 2.34. The scattering frequency can be interpreted as $\nu(\mu, p) \propto \Omega(\delta B/B_0)^2$, (as $k\mathcal{E}(k) \sim (\delta B)^2$, i.e., the Alfvén wave's energy scales with its magnetic field energy). If one interprets the angle enclosed by δB and B_0 as the rms of the scattering angle $\delta\theta$ and assumes that the CR is scattered by random angle configurations then the angular diffusion coefficient is given by $\langle(\delta\theta)^2\rangle/\delta t \sim \Omega(\delta B/B_0)^2$ yielding an intuitive explanation of Equation 2.35.

Self-confinement of CRs

Alfvénic fluctuations δB are naturally present in the interstellar medium as a result of cascading large scale MHD turbulence. However, the Alfén wave cascade does not provide efficient scattering partners for the CRs. The problem is the highly anisotropic nature of the turbulence (Zweibel 2013). The ratio $k_{\perp}/k_{\parallel}$ is expected to increase for smaller and smaller scales below the

driving scale. Gyro-resonant fluctuations with $k_\perp/k_\parallel \gg 1$ are very inefficient for scattering as the strong variability of the magnetic field fluctuations smooths out the effect. Other possible scattering sources include magnetic mirroring or scattering by magneto-sonic waves generated by compressibility effects in the cascade. For the later, the relevant damping mechanisms are difficult to determine (Zweibel 2013). In addition, fast magneto-sonic waves seem to be the relevant waves in the cascade for CR scattering. However, they only carry a small fraction of the energy in the cascade (Zweibel 2017).

The most discussed mechanism is based on waves generated by the CRs themselves. An instability can be derived that leads to the the excitation of Alfvén waves with wavelengths equal to the projected gyro-radius of the CRs. To derive the growth rate of the waves $\Gamma_{\rm rc}$, we start with the Vlasov equation and use linear perturbation theory to derive the dispersion relation of an excited wave. This results from perturbing the external magnetic and electric field in the presence of a CR population with distribution function $f(\boldsymbol{x}, \boldsymbol{p}, t)$. We assume a low CR density such that CRs only influence the system by exciting growing waves that are damped by collisionless processes. In the opposite extreme, large CR densities may lead to strongly enhanced magnetic fields near strong shocks (Caprioli and Spitkovsky 2014). The imaginary part of the resulting frequency gives the growth rate of the instability corresponding to the growth rate of the Alfvén waves as (Skilling 1971)

$$\Gamma_{\rm cr} = \frac{\pi^2}{2}\frac{q^2 v_A}{ck}\int \frac{v(1-\mu^2)}{cp} \times \left[\delta\left(\mu + \frac{m\Omega_0}{kp}\right) + \delta\left(\mu - \frac{m\Omega_0}{kp}\right)\right]\frac{\partial f}{\partial \mu} d^3p \tag{2.36}$$

in the frame of the wave. The delta distributions show the resonance for left- and right-handed circularly polarized waves, which is equivalent to the gyro-resonance with negligible ω. For positive anisotropies of the CRs in their frame $\partial f/\partial\mu > 0$ the waves grow, for negative anisotropies they are damped and for isotropic CRs they stay neutral. Thus, if the CRs and waves move in the same direction the waves are unstable, if the CRs stream faster than the waves (positive anisotropy). We see that only CRs above the minimum momentum $p_{\rm min} = m\Omega_0/k$ are able to resonate with waves of wavenumber k. Assuming a power-law distribution of CRs, $f \propto p^{-\alpha}$, and comparing the result of the integral with the expression of the number density of CRs $n_{\rm cr}$ above momentum $p_{\rm min}$ one obtains (Kulsrud and Cesarsky 1971)

$$\Gamma_{\rm cr} = \frac{\pi}{4}\frac{\alpha-1}{\alpha}\Omega_0 \frac{n_{cr}(>p_{min})}{n_i}\left(\frac{v_D}{v_A} - 1\right), \tag{2.37}$$

where $n_{\rm i}$ is the ion number density of the ambient medium and $v_{\rm D}$ describes the streaming velocity of the CRs along the background magnetic field. For typical values in the ISM, CRs of energy of a few GeV and $v_{\rm D}/v_{\rm A} \sim 1$, one obtains a growth time of 10^{10} s $\sim$ 300 yr. This implies that in galactic environments CRs adopt quickly to their environment (Zweibel 2013).

The steep spectral index $\alpha \sim 4.6$ of the momentum p for GeV CRs means that wave growth becomes less relevant for higher-energy CRs. Thus, at around $\sim$ 100 GeV, CRs will not anymore be able to confine themselves. The reason for this is that some form of wave damping is always present and the growth time is too large in comparison to the damping time. Another consequence of the steep CR spectrum is the fact that waves that grow at the scale k are largely produced by CRs at $p_{\rm min}(k)$ (Zweibel 2013).

Qualitatively, one can interpret Equation 2.37 as the momentum loss of a single CR, $\dot{p} \propto p\Omega = (\gamma mc)(\Omega_0/\gamma) \propto \Omega_0$, which is proportional to the non-relativistic gyro-frequency. The growth rate scales with the number of available CRs that are able to generate waves, $n_{\rm cr}(> p_{\rm min})$, and is inversely proportional to thermal ions, which provide inertia slowing down wave growth. As already seen above, isotropic CR populations cannot drive waves. This becomes evident from the factor $v_{\rm D}/v_{\rm A} - 1$ which is 0 if all particles move ($v_{\rm D}$) with the same speed as the wave ($v_{\rm A}$) and negative, i.e. wave damping, for $v_{\rm D} < v_{\rm A}$ (Wiener et al. 2013).

Wave damping

So far there is no criterion hindering the CRs from transferring their energy into the creation of more and more waves. However in nature, there are damping processes that impede wave growth. The two most relevant ones in the environment of clusters are non-linear Landau damping and turbulent damping.

The basic idea behind *non-linear Landau* (NL) *damping* is the superposition of two waves A and B of slightly different frequency forming a beat wave. This beat wave is then able to interact with thermal particles with parallel velocities, which are identical to the phase speed of the wave $v_\parallel = (w_A - w_B)/(k_A - k_B)$. Particles moving faster than the wave add energy to the wave and particles that are slightly slower than the wave extract energy from the wave, i.e. damp the wave. For Maxwellian plasmas, usually $\partial f/\partial v < 0$ in the range $v_\parallel = v_\mathrm{A}$ and consequently, damping dominates. The NL damping rate (Lee and Völk 1973) in the case of a high plasma beta (Wiener et al. 2013) is given by

$$\Gamma_\mathrm{NL} \approx \frac{1}{2}\sqrt{\frac{\pi}{2}}\left(\frac{v_\mathrm{i}}{v_\mathrm{A}}\right)\left(\frac{\delta B}{B}\right)^2 w \approx 0.3\frac{\Omega}{\mu}\frac{v_\mathrm{i}}{c}\left(\frac{\delta B}{B}\right)^2 \tag{2.38}$$

The wave frequency $w = k_\parallel v_\mathrm{A}$ sets the fundamental frequency of interaction while interactions with the beat wave arise to second order in magnetic field fluctuations. As particles moving at speed $v_\parallel = v_\mathrm{A}$ are in resonance and $v_\parallel = \mu v_\mathrm{i}$, it is reasonable to assume that the damping rate depends on the ratio $\mu = v_\mathrm{i}/v_\mathrm{A}$.

But where exactly does the generation of Alfvén waves settle into a steady state with the NL damping process? This balance ultimately determines the value of the bulk velocity of the CRs, often termed *drift velocity* v_D or *streaming velocity*. Using Equation 2.34 in the limit of strong scattering such that the CR distribution function can be expanded as $f = f_0 + f_1 + f_2 + ...$, the equation can be simplified such that

$$\frac{\partial \mathcal{F}}{\partial \mu} = -\frac{c}{\nu L_Z}, \tag{2.39}$$

where $L(p,z) = f_0/(\partial f/\partial z)$ is the scale height and $\mathcal{F} = f_1/f_0$ is the relative perturbed CR distribution function. We assume (Wiener et al. 2013)

$$\mathcal{F} = 1 + \frac{3(v_\mathrm{D} - v_\mathrm{A})}{c}\mu \tag{2.40}$$

with the accessible characteristic that the leading anisotropy in the distribution function is given by the net drift relative to the wave frame, i.e. $\langle \mu c \mathcal{F}(\mu)\rangle = v_D - v_A$. One can consider CRs at ~ 1 GeV ($\gamma \sim 1$) with a power law distribution including cutoff at momentum q

$$f_0(p) \propto p^{-\alpha}\Theta(p-q). \tag{2.41}$$

In steady state the NL damping rate of waves Γ_NL (Equation 2.37) is equal to the growth rate of waves due to CRs, Γ_cr (Equation 2.38). Combining the resulting equation with Equation 2.39 the drift velocity $v_\mathrm{D,NL}$ is given by (Jacob 2015)

$$v_\mathrm{D,NL} = v_\mathrm{A}\left(1 + 0.002\frac{n_{i,-2}^{3/4}\, T_\mathrm{2keV}^{1/4}\, \gamma^{(\alpha-1)/2}}{B_{15\mu\mathrm{G}}\, L_{z,20\mathrm{kpc}}^{1/2}\, n_\mathrm{cr,fid}^{1/2}}\right) \tag{2.42}$$

scaled to realistic values for CCs ($n_{i,-2} = n_i/(10^{-2}\mathrm{cm}^{-3})$, $B_{15\mu\mathrm{G}} = B/(15\mu\mathrm{G})$, $L_{z,20\mathrm{kpc}} = L/(20\mathrm{kpc})$, $T_\mathrm{2keV} = T/(2\mathrm{keV})$, $n_\mathrm{CR,fid} = n_\mathrm{cr}/(5\times 10^{-9}\mathrm{cm}^{-3})$) with $\alpha = 2.2$ and $q = 0.5\ m_p c$.

One can clearly see that considering only NL damping the velocity of CRs is strongly constrained by the generation of the Alfvén waves and their drift velocity is basically given by the Alfvén velocity.

The other relevant damping process in the studied environments for our analysis is *turbulent damping*. As discussed above, the highly anisotropic nature of MHD turbulence (Yan and Lazarian 2002; Farmer and Goldreich 2004) makes it unlikely for the CRs to be confined. Exactly the opposite is true in CCs, magnetic turbulence damps waves (Wiener et al. 2013). In clusters, turbulence is subsonic except for the outskirts. Combining this with the fact that strong turbulence is prevalent in clusters ($\mathcal{M}_\mathrm{A} \gtrsim 1$; $\mathcal{M}_\mathrm{A} = v/v_\mathrm{A}$), the MHD turbulence theory by Goldreich and Sridhar (1995) is applicable (Wiener et al. 2013). One major complication of MHD turbulence compared to HD turbulence is the fact that MHD turbulence is highly anisotropic as the magnetic field reacts much stronger to motion perpendicular to the field lines (magnetic tension, pressure) than motions parallel to the fields. As we need to consider anisotropic interactions now, we have to introduce two different timescales $\tau_\perp = v_{\lambda_\perp} k_\perp$ and $\tau_\parallel = v_\mathrm{A} k_\parallel$ with the length-scale transverse to the local mean magnetic field $\lambda_\perp$ and the root mean squared velocity component across this scale $v_{\lambda_\perp}$. Assuming so called *local balance* between the different time scales, we equate them and arrive at (Nazarenko and Schekochihin 2011):

$$v_{\lambda_\perp} k_\perp = v_\mathrm{A} k_\parallel \tag{2.43}$$

We assume $\lambda_\parallel(\lambda_\perp)$ is the length-scale parallel to the local mean magnetic field across which the velocity fluctuation is $v_{\lambda_\perp}$, L_MHD is the driving scale of the turbulence with speeds $\mathcal{M}_\mathrm{A} = 1$ and $\epsilon \sim v_{\lambda_\perp}^3/\lambda_\perp \sim v_\mathrm{A}^3/L_\mathrm{MHD}$ is the constant (as incompressible) energy input per unit time. Then within the framework of strong incompressible MHD turbulence we have

$$v_{\lambda_\perp} \sim v_\mathrm{A} \left(\frac{\lambda_\perp}{L_\mathrm{MHD}}\right)^{1/3} \sim (\epsilon \lambda_\perp)^{1/3} \tag{2.44}$$

$$\frac{\lambda_\parallel(\lambda_\perp)}{\lambda_\perp} \sim \left(\frac{L_\mathrm{MHD}}{\lambda_\perp}\right)^{1/3} \tag{2.45}$$

Equation 2.44 shows the typical relation for Kolmogorov turbulence here in the perpendicular direction. Equation 2.45 on the other shows that an eddy becomes increasingly elongated along a magnetic field line ($\lambda_\perp/\Lambda_\parallel \ll 1$) over time, as $L_\mathrm{MHD}/\lambda_\perp$ increases following the energy cascade down to the dissipative scale. This means that the cascade proceeds mostly in the perpendicular direction. And as in general $\epsilon = v^3\tau$ and from Equation 2.44 $v_{\lambda_\perp}/v_\mathrm{A} \sim (\lambda_\perp/L_\mathrm{MHD})^{1/3}$, we see that throughout the cascade more turbulent energy will be stored in the perpendicular direction.

Intuitively, this can be seen from the idea that in MHD turbulence, non-linear interactions arise from two colliding wave particles traveling along magnetic field lines. Wave packets are distorted if the colliding partner causes the wave packet to distort the field line on scales of $\lambda_\perp$ and to cascade to smaller scales. The velocity and magnetic fluctuations associated with Alfvén waves happen in the perpendicular direction to the magnetic field line and thus most energy will be stored here. The confining waves of the CRs are hereby perturbed and cascade down before CRs scatter on them. In addition small-scale perpendicular fluctuations introduced by MHD turbulence will hinder the effective forcing of pitch angle scattering that is necessary for confinement. The damping rate thus corresponds to the eddy turnover scale in the perpendicular direction

$$\Gamma_\mathrm{turb} \sim \frac{v_{\lambda_\perp}}{\lambda_\perp} \sim \frac{\epsilon^{1/3}}{\lambda_\perp^{2/3}} \tag{2.46}$$

using Equation 2.44. The minimum turbulent damping rate can then be determined as follows. First, one derives an expression for the largest $k_\parallel$ of the Alfvén waves (created by the CRs) as $(k_\perp/k_\parallel)_{\rm min} \sim \delta B(\lambda_\perp)/B \sim v_{\lambda_\perp}/v_{\rm A} \sim (\lambda_\perp/L_{\rm MHD})^{1/3}$ using Equation 2.44 in the last step. Using this result and again Equation 2.44 with the resonance condition $k_\parallel \sim r_{\rm L}^{-1}$ one obtains $k_{\perp,\rm min} \sim \epsilon^{1/4}(r_L v_{\rm A})^{-3/4}$, which in turn can be combined with Equation 2.46 to obtain the minimum turbulent damping rate in resonance (Wiener et al. 2013)

$$\Gamma_{\rm turb,min} \sim \left(\frac{\epsilon}{r_{\rm L} v_{\rm A}}\right)^{1/2}. \tag{2.47}$$

Again, if one uses the same type of CR population as for the NL case above, one obtains the following steady state drift velocity of the CRs (Jacob 2015)

$$v_{\rm D,turb} = v_{\rm A}\left(1 + 0.004\,\frac{B_{15\mu\rm G}^{1/2}\; n_{\rm i,-2}^{1/2}}{L_{\rm MHD,20}^{1/2}\; n_{\rm cr,fid}}\right), \tag{2.48}$$

where $L_{\rm MHD,20} = L_{\rm MHD}/(20\rm kpc)$ is the scale height. We can clearly see that the most relevant damping processes are not able to significantly damp the wave in order to approximately alleviate the self-confinement of the CRs. Their drift velocity has been shown to be equal to the Alfvén velocity of the waves.

Transport processes

These findings show that CRs are self-confined. This has major implications on their transport processes. The resulting equation in the limit of frequent wave-particle scattering is given by Skilling (1975)

$$\frac{\partial f_p}{\partial t} + (\boldsymbol{u} + \boldsymbol{v}_{\rm D})\cdot\nabla f_p = \nabla\cdot[\kappa_p \boldsymbol{b}(\boldsymbol{b}\cdot\nabla f_p] + \frac{1}{3}p\frac{\partial f_p}{\partial p}\nabla\cdot(\boldsymbol{u}+\boldsymbol{v}_{\rm D}) + \frac{1}{p^2}\frac{\partial}{\partial p}\left[p^2\Gamma_p\frac{df_p}{\partial p}\right] + Q, \tag{2.49}$$

where $f(\boldsymbol{x}, p, t)$ is the CR distribution function (isotropic in momentum space), $\boldsymbol{u}$ is the gas velocity, $\boldsymbol{v}_{\rm A}$ is the Alfvén velocity, the direction of the magnetic field is $\boldsymbol{b} = \boldsymbol{B}/|\boldsymbol{B}|$ and Q is the CR source function. Momentum has been normalized to mc and κ_p describes the diffusion coefficient.

Here, the derivation will be sketched briefly following Wiener et al. (2013). We start with the Vlasov equation (Equation 2.30) under the influence of the Lorentz force ($d\boldsymbol{p}/dt = \boldsymbol{F}_{\rm L}$) but evaluated in the frame of the CR-excited Alfvén waves and averaged over pitch angles. Then, the distribution function is approximated as an expansion in the inverse scattering frequency ν, $f = f_0 + f_1 + f_2 + ...$ with $f_i = \mathcal{O}(\nu^{-i})$. As we are in the limit of strong scattering the distribution can be seen as isotropic plus a small anisotropy included in f_1.

The left-hand side of Equation 2.49 can then be interpreted as the advective transport of CRs whereas on the right-hand side, from left to right: diffusive transport along magnetic field lines, diffusive shock acceleration as well as second-order Fermi acceleration (momentum-space diffusion) and sources/sinks for the distribution function. Thus, the system is fully determined if κ, Γ_p and Q are given.

When considering only the isotropic distribution function f_0 in the wave frame (no cross frame diffusion, $\kappa = 0$) and only keeping terms of order p, the transport equation simplifies to

$$\frac{Df_0}{Dt} = \frac{1}{3}p\frac{\partial f_0}{\partial p}\nabla\cdot(\boldsymbol{u} + \boldsymbol{v}_{\rm A}) \tag{2.50}$$

Thus, the CRs just move adiabatically in the wave frame, with $p \propto n_{\rm cr}^{1/3}$. Scattering of the CRs in the wave frame does not involve electric field, consequently particles conserve energy. In the frame of the plasma however, the presence of electric fields causes the CRs to lose energy heating the plasma in the process. The volumetric heating rate can be derived (Kulsrud 2005; Jacob 2015) as

$$\Gamma_{\rm wave} = -\boldsymbol{v}_{\rm A} \cdot \nabla P_c \tag{2.51}$$

The work is transmitted by the Alfvén waves in the system. Thus, their speed enters into this wave-heating rate.

As indicated by Equation 2.36 CRs only excite Alfvén waves that propagate down the CR pressure gradient. In addition we know that due to relatively weak damping the CRs are forced to basically stream at the Alfvén velocity. To summarize, CRs are able to only stream down their gradient and in the here studied limit $v_{\rm D} \rightarrow v_{\rm A}$, CRs propagate at the streaming velocity $v_{\rm st}$, given in this limit by

$$\boldsymbol{v}_{\rm st} = -{\rm sgn}\left(\hat{\boldsymbol{b}} \cdot \nabla P_{\rm cr}\right) \boldsymbol{v}_{\rm A} \tag{2.52}$$

Fluid description

The small scale and continuous interactions through pitch-angle scattering make a fluid description of CRs possible. CRs affect the thermal gas via pitch angle scatterings, which can be cast into an effective pressure. Analogously to hydrodynamics, the three moments of f_p are defined as the CR number density $n_{\rm cr}$, CR pressure $P_{\rm cr}$ and CR energy density $\epsilon_{\rm cr}$.

$$n_{\rm cr} = 4\pi \int_0^\infty p^2 f_p(p) {\rm d}p \tag{2.53}$$

$$P_{\rm cr} = \frac{4\pi m c^2}{3} \int_0^\infty \beta p^3 f_p(p) {\rm d}p \tag{2.54}$$

$$\epsilon_{\rm cr} = 4\pi \int_0^\infty p^2 {\rm E}_p(p) f_p(p) {\rm d}p, \tag{2.55}$$

where $\rm E_p$ is the kinetic energy of a CR particle given by

$${\rm E}_p(p) = (\sqrt{1+p^2} - 1) m c^2, \tag{2.56}$$

where the closure relation is given by the equation of state for CRs

$$P_{\rm cr} = (\gamma_{\rm cr} - 1)\epsilon_{\rm cr} \tag{2.57}$$

where $\gamma_{\rm cr} = 4/3$ is the CR adiabatic index.

Using Equation 2.49 multiplied with E_p and integrated over the mentioned momenta of p, one can derive the following equation for the evolution of the CR energy density ϵ_{cr} (Pfrommer et al. 2017)

$$\frac{\partial \epsilon_{\rm cr}}{\partial t} + \nabla \cdot \left[(\boldsymbol{v} + \boldsymbol{v}_{\rm st})(P_{\rm cr} + \epsilon_{\rm cr}) - \kappa_\epsilon \boldsymbol{b}(\boldsymbol{b} \cdot \nabla \epsilon_{\rm cr})\right] = (\boldsymbol{v} + \boldsymbol{v}_{\rm st}) \cdot \nabla P_{\rm cr} + \Gamma_{\rm acc} + \bar{Q}_\epsilon, \tag{2.58}$$

where the momentum-space averaged spatial diffusion coefficient κ_ϵ, the net source of mean kinetic energy density of CRs $\bar{Q}_\epsilon$ and the energy gain per unit time of CRs due to second-order Fermi acceleration $\Gamma_{\rm acc}$ are given by

$$\kappa_\epsilon = \frac{\int_0^\infty p^2 E_{\rm p}(p)\kappa_{\rm p}(\boldsymbol{x},p)\ \boldsymbol{b}\cdot\nabla f_{\rm p}\ {\rm d}p}{\int_0^\infty p^2 E_{\rm p}(p)\ \boldsymbol{b}\cdot\nabla f_{\rm p}\ {\rm d}p} \tag{2.59}$$

$$\bar{Q}_\epsilon = 4\pi\int_0^\infty p^2 E_{\rm p}(p) Q(\boldsymbol{x},p){\rm d}p \tag{2.60}$$

$$\Gamma_{\rm acc} = -4\pi m c^2 \int_0^\infty \beta p^2 \Gamma_{\rm p}\frac{\partial f_{\rm p}}{\partial p}{\rm d}p > 0 \qquad \text{for} \qquad \frac{\partial f_{\rm p}}{\partial p} < 0. \tag{2.61}$$

In the arising picture (Pfrommer et al. 2017), the CR energy density is modulated by advection of the CR enthalpy $h_{\rm cr} = P_{cr} + \epsilon_{\rm cr}$ with total velocity $\boldsymbol{v} + \boldsymbol{v}_{\rm st}$ according to the second term on the left, which also captures the anisotropic diffusion of CRs along magnetic field lines. The first term on the right captures the energy loss rate of CRs due to the volume work of the CR pressure on the background plasma ($\boldsymbol{v}\cdot\nabla P_{cr}$) and the generation of Alfvén waves ($\boldsymbol{v}_{\rm cr}\cdot\nabla P_{\rm cr}$). The term $\Gamma_{\rm acc}$ describes the production of CR energy density through second-order Fermi acceleration. Lastly, the term $\bar{Q}_\epsilon$ encapsulates all the remaining loss $\Lambda_{\rm cr}$ and gain terms $\Gamma_{\rm cr}$ in the form $\bar{Q}_\epsilon = \Gamma_{\rm cr} - \Lambda_{\rm cr}$.

2.3 AREPO

For our analysis, we use the magneto-hydrodynamical cosmological code AREPO (Springel 2010). The code is based on a moving, unstructured Voronoi mesh. The hyperbolic conservation laws of magneto-hydrodynamics are solved on the mesh using a finite volume approach. Thereby, the code represents a combination of Lagrangian characteristics in combination with a finite-volume Eulerian mesh code. The main idea of this approach is to inherit many advantages of SPH techniques (e.g., intrinsic adaptivity, low advection errors, small numerical diffusion) as well as of fixed mesh codes (e.g., better convergence for smooth flows, good shock capturing). Numerical convergence (perfect accuracy in the limit of infinite resolution) for codes employing SPH is first of all hard to show (Zhu et al. 2015) and in the limit of high resolution tends to shows less optimal solutions then fixed mesh codes. AREPO, on the other hand, shows second order numerical convergence (Pakmor et al. 2016b) while keeping a low level of numerical truncation errors.

2.3.1 Magneto hydrodynamics solver

The Euler equations describing ideal MHD can be written as a system of hyperbolic conservation laws for conserved quantities $\boldsymbol{U}$ and flux $\boldsymbol{F}(\boldsymbol{U})$ in the form

$$\frac{\partial \boldsymbol{U}}{\partial t} + \nabla\cdot\boldsymbol{F} = 0, \tag{2.62}$$

where $\boldsymbol{U}$ and $\boldsymbol{F}(\boldsymbol{U})$ are given by

$$\boldsymbol{U} = \begin{pmatrix} \rho \\ \rho\boldsymbol{v} \\ \rho e \\ \boldsymbol{B} \end{pmatrix} \qquad \boldsymbol{F}(\boldsymbol{U}) = \begin{pmatrix} \rho\boldsymbol{v} \\ \rho\boldsymbol{v}\boldsymbol{v}^{\rm T} + P\boldsymbol{1} - \boldsymbol{B}\boldsymbol{B}^{\rm T} \\ \rho e\boldsymbol{v} + \rho\boldsymbol{v} - \boldsymbol{B}(\boldsymbol{v}\cdot\boldsymbol{B}) \\ \boldsymbol{B}\boldsymbol{v}^{\rm T} - \boldsymbol{v}\boldsymbol{B}^{\rm T} \end{pmatrix}, \tag{2.63}$$

where $P = P_{\rm gas} + B^2/2$ is the total gas pressure and $e = u + \frac{1}{2}v^2 + \frac{1}{2\rho}B^2$ is the total energy per unit mass, adopting the units system of Heaviside-Lorentz. The closure relation is given by the equation of state, $P = \rho(\gamma - 1)$, with adiabatic index γ.

For obtaining the fluxes over an interface, approximate Riemann problems are solved along the normal of the interfaces (Pakmor et al. 2011, 2013). For this, the values of the conserved quantities to the left and right of the interface are spatially extrapolated.

Heun's method has been adopted for AREPO. It is based on a second-order Runge-Kutta method where fluxes are estimated using the values of primitive variables both at the beginning and at the end of the time step. Two different meshes are in theory needed for this, however, the new mesh can be recycled at the next time step, so effectively, only one mesh construction step is necessary per time-step however fluxes have to be calculated twice. Conservative variables are extrapolated using spatial derivatives instead of storing intermediate states with initial values which complicates book-keeping especially when using adaptive time-steps (Pakmor et al. 2016b).

Gradients are estimated using a least-square gradient estimator (Pakmor et al. 2016b). Here, the center of mass $\boldsymbol{r}_i$ value of variable $Q_{{\rm cm}_i}$ of cell i is assumed to be linearly connected to each neighboring cell's center of mass values $Q_{{\rm cm}_j}$ at $\boldsymbol{r}_j$ via the estimated gradient $\langle \nabla \phi_i \rangle$. Solving for the smallest error of extrapolated values $Q'_{{\rm cm}_j}$ using $\langle \nabla \phi_i \rangle$ and actual values $Q_{{\rm cm}_j}$ yields an estimate for the gradient. The weights g_j for the least square optimization are assigned according to the respective distance between neighbor j and cell i, i.e. $g_j \propto 1/(|r_i - r_j|)$.

The calculated fluxes have to be evolved in time across the moving interfaces. Due to the nature of the moving mesh in AREPO, the equations become more complex here. The fluxes are calculated in the rest frame of the interface to prevent numerical inaccuracies due to the fact that mesh points normally have very similar velocities in comparison to the fluid velocity. A HLLD Rieman solver is used for the time evolution (Miyoshi and Kusano 2005). As generally the case for fluid dynamics, the maximum time step is limited by the maximum signal speed of a cell, which is given by the fastest magneto-acoustic waves in the system plus the velocity of the cell (when working in the cell frame).

In addition to fulfilling the MHD equations given by Equation 2.62, magnetic fields obey the constraint

$$\nabla \cdot \boldsymbol{B} = 0, \tag{2.64}$$

according to Maxwell's equations. In theory, a divergence-free initial magnetic field should keep this property when evolved in time. However, due to discretization errors, this is in practice not the case in MHD simulations. If ignored, these errors can significantly amplify magnetic and velocity fields, leading to unphysical solutions (Pakmor and Springel 2013). The so called constrained transport approach discretizes the electric and magnetic field in such a way that their consequent evolution automatically guarantees a divergence-free magnetic field (Evans and Hawley 1988).

Alternatively as done here, the Powell approach is adopted (Powell et al. 1999). Here, a term describing the passive advection of magnetic fields with the flow is added to the momentum, induction and energy equation. These modifications prevent the further growth of magnetic field divergences in a stable manner (Pakmor and Springel 2013). In addition, the adaptations allow for local time-stepping, which makes the code much more efficient.

2.3.2 Cosmic ray module

This section follows (Pfrommer et al. 2017), here we provide a short overview of the implementation of CRs in AREPO. CRs with energies $\sim$ 1GeV dominate the CR pressure which

makes their interactions with the gas the most relevant for our analysis. AREPO focuses on this population of CRs. They are treated as a second fluid next to the gas. So far, only the energy density of these CRs is evolved without spectral information. As discussed in Section 2.2.2, the fluid description is justified within the framework of self-constrained CR transport via streaming. CRs effectively stream at the speed of the Alfvén waves that they generate as they pitch angle scatter on the waves.

Equation 2.58 shows the consequence of this mechanism as CRs are advected with the Alfvén wave frame at velocity $\boldsymbol{v} + \boldsymbol{v}_{\rm st}$ and diffuse along magnetic field lines. In addition, adiabatic expansion or contraction of CRs modifies the CR energy density. CR acceleration represents CR sources, $\Gamma_{\rm acc}$. The pitch angle scattering process leads to a transfer of energy from the CRs to the gas, thereby forming a sink for the CR energy density, $\bar{Q}_\epsilon$.

In summary, the hyperbolic MHD equations, again expressed in the unit system of Heavyside-Lorentz, are modified and a source term $\boldsymbol{S}$ is added

$$\frac{\partial \boldsymbol{U'}}{\partial t} + \nabla \cdot \boldsymbol{F'} = \boldsymbol{S}, \tag{2.65}$$

where $\boldsymbol{U'}$ is a conserved variables and $\boldsymbol{F'}(\boldsymbol{U'})$ is the flux function given by (Pfrommer et al. 2017)

$$\begin{aligned} \boldsymbol{U'} &= \begin{pmatrix} \rho \\ \rho\boldsymbol{v} \\ \epsilon \\ \epsilon_{\rm cr} \\ \boldsymbol{B} \end{pmatrix}, \boldsymbol{F'} = \begin{pmatrix} \rho\boldsymbol{v} \\ \rho\boldsymbol{v}\boldsymbol{v}^{\rm T} + P\mathbf{1} - \boldsymbol{B}\boldsymbol{B}^{\rm T} \\ (\epsilon + p)\boldsymbol{v} - \boldsymbol{B}(\boldsymbol{v}\cdot\boldsymbol{B}) \\ \epsilon_{\rm cr}\boldsymbol{v} + (\epsilon_{\rm cr} + P_{\rm cr})\boldsymbol{v}_{\rm st} - \kappa_\epsilon \boldsymbol{b}(\boldsymbol{b}\cdot\nabla\epsilon_{\rm cr}) \\ \boldsymbol{B}\boldsymbol{v}^{\rm T} - \boldsymbol{v}\boldsymbol{B}^{\rm T} \end{pmatrix}, \\ \boldsymbol{S} &= \begin{pmatrix} 0 \\ \mathbf{0} \\ P_{\rm cr}\nabla\cdot\boldsymbol{v} - \boldsymbol{v}_{\rm st}\cdot\nabla P_{\rm cr} + \Lambda_{\rm th} + \Gamma_{\rm th} \\ -P_{\rm cr}\nabla\cdot\boldsymbol{v} + \boldsymbol{v}_{\rm st}\cdot\nabla P_{\rm cr} + \Lambda_{\rm cr} + \Gamma_{\rm cr} \\ \mathbf{0} \end{pmatrix}, \end{aligned} \tag{2.66}$$

where $\Gamma_{\rm cr}$ is the source term and $\Lambda_{\rm cr}$ is the sink term for CRs. Now, the total pressure is given by $P = P_{\rm th} + P_{\rm cr} + \boldsymbol{B}^2/2$ and the total energy density reads $\epsilon = \epsilon_{\rm th} + \rho\boldsymbol{v}^2/2 + \boldsymbol{B}^2/2$. The CR streaming velocity can be expressed (see Section 2.2.2) as

$$\boldsymbol{v}_{\rm st} = -\boldsymbol{v}_{\rm A}\ \mathrm{sgn}(\boldsymbol{B}\cdot\nabla P_{\rm cr}) = -\frac{\boldsymbol{B}}{\sqrt{\rho}}\frac{\boldsymbol{B}\cdot\nabla P_{\rm cr}}{|\boldsymbol{B}\cdot\nabla P_{\rm cr}|}. \tag{2.67}$$

The streaming speed of the CRs corresponds to the Alfvén speed $\boldsymbol{v}_{\rm A}$ and is always directed along magnetic field lines down the CR gradient.

The MHD solver that is described in Section 2.3.1 is used to solve the equations with the modified total pressure and energy density. First, gradients are estimated using the least-square gradient estimator. These gradients are needed for the Runge-Kutta time integration (Pakmor et al. 2016b). The Rieman problem across interfaces is solved with the HLLD Riemann solver (Pakmor et al. 2011). The modified adiabatic index influences the speed of the fast and slow magneto-acoustic waves which is of importance for determining the time-step of individual cells.

The CR energy density equation is solved by passively advecting the CRs with the gas. Adiabatic changes $P_{\rm cr}\nabla\cdot\boldsymbol{v}$ are determined via Gauss' theorem in every cell and exchanging the net flux across cells. The remaining source terms and active CR transport are treated seperately, i.e., via operator splitting after evolving the system by one time step. In theory, CRs can be injected at hydrodynamical shocks in the simulation, which however would be secondary to the

main objective of this thesis. Instead we will focus CR diffusion along magnetic fields (Pakmor et al. 2016a) and neglect CR streaming (which is postponed to future work). For CR losses, we consider Coulomb interactions and inelastic collisions between CRs and thermal protons as well as Alfvén wave heating as a result of damping of Alfvén waves.

Diffusion of cosmic rays

CRs have been shown to diffuse along magnetic fields as they pitch-angle scatter on magnetic irregularities. This property is crucial for the dynamical effect of CRs on the plasma. AREPO employs a semi-implicit solver for anisotropic CR diffusion with local timestepping (Pakmor et al. 2016a). To ensure numerical stability in explicit solvers, time steps are required to scale quadratically with the linear dimension of the resolution elements. If global time steps were necessary, the cell with the smallest CR diffusion time scale would limit the time step of every cell in the simulation. Both issues would severely limit the size of the simulation, rendering cosmological applications impossible. The implemented solver is based on the flux limiting scheme by Sharma and Hammett (2007) and the semi-implicit time integration scheme developed by Sharma and Hammett (2011). In addition to the mentioned features, the solver also ensures energy conservation and CRs are only transported from high to low abundance regions in agreement with the entropy condition $\Delta S \geq 0$.

The basic diffusion equation is given by

$$\frac{\partial \epsilon_{\mathrm{cr}}}{\partial t} - \nabla \cdot [\kappa_\epsilon \boldsymbol{b}\ (\boldsymbol{b} \cdot \nabla \epsilon_{\mathrm{cr}})] = 0. \tag{2.68}$$

The diffusion equation is now integrated over the volume of cell i and divided by its volume V_i. Using Gauss's theorem, one obtains

$$\frac{\partial \epsilon_{\mathrm{cr},i}}{\partial t} - \int_{\partial V_i} \kappa_\epsilon (\boldsymbol{b} \cdot \nabla \epsilon_{\mathrm{cr}}) \boldsymbol{b} \cdot \mathrm{d}\boldsymbol{A_i}, \tag{2.69}$$

where $\epsilon_{\mathrm{cr},i}$ is the CR energy density of cell i and $\mathrm{d}\boldsymbol{A}_i$ is oriented normal to the surface of the cell. Discretization of the problem yields

$$\frac{\partial \epsilon_{\mathrm{cr},i}}{\partial t} - \frac{1}{V_i} \sum_j \kappa_{ij} (\boldsymbol{b}_{ij} \cdot \nabla \epsilon_{\mathrm{cr},ij}) \boldsymbol{b}_{ij} \cdot \boldsymbol{n}_{ij} A_{ij} = 0, \tag{2.70}$$

where j runs over all cell interfaces, $\nabla \epsilon_{\mathrm{cr},ij}$ gives the gradient of the CR energy density at the cell interface, $\boldsymbol{n}_{ij}$ is the normal vector of the interface and A_{ij} is its area. A sophisticated estimate for CR energy density gradients at interfaces is crucial for satisfying the entropy condition.

Here, the gradient at the interface is estimated from the gradient at the corners of the mesh. As before, this is done via optimization of the interpolated/extrapolated center of mass of neighboring cells. In a Voronoi mesh the corner of a cell $\boldsymbol{c}$ is surrounded by four neighboring cells with center of masses at positions $\boldsymbol{s}_i$. A linear interpolation of the values at centers of mass of adjacent cells is performed to their common corner with the gradient at the corner of a cell. To estimate the gradient, the residual of the interpolation is minimized. The residual $\boldsymbol{r}_i$ is given by

$$\boldsymbol{r}_i = \phi(\boldsymbol{c}) + (\nabla \phi)(\boldsymbol{s}_i - \boldsymbol{c}) - \phi(\boldsymbol{s}_i), \tag{2.71}$$

where $\phi(\boldsymbol{c})$ is the unknown value at the corner of a cell, $\phi(\boldsymbol{s}_i)$ is the value at the center of mass s_i of cell i and $\nabla \phi$ is the gradient at the corner.

By setting the residual to zero ($r_i = 0$), four independent equations are obtained with four unknowns, namely $\phi(\boldsymbol{c})$ and $\nabla\phi$. They can be brought in the convenient form

$$\boldsymbol{q} = \mathbf{M}\boldsymbol{Y}, \tag{2.72}$$

where $\boldsymbol{q}(\phi(\boldsymbol{c}), \nabla\phi)$ and $\boldsymbol{Y}(\phi(\boldsymbol{s}_i))$ are vectors and $\mathbf{M}(\boldsymbol{s}_i, \boldsymbol{c}_i,)$ is a matrix. Consequently, $\mathbf{M}$ only contains properties related to the mesh whereas $\boldsymbol{Y}$ only contains quantities at the centers of mass (for more details see Pakmor et al. 2016a).

$\mathbf{M}$ can easily be determined with standard solvers of linear algebra. Its first row is only related to the value at the corner. If the entries are positive, this corresponds to the case where the position of the corner is within the tetrahedron enclosed by the neighboring centers of mass. This means that the quantity at the corner can be interpolated. In contrast, at least one negative value implies that the position of the corner lies outside the tetrahedron. In this case, the quantity at the corner has to be extrapolated, which is generally unstable. To retain stability, special care has to be taken for corners with $\mathbf{M}_0, j < 0$. In this implementation, the threshold is set less strictly to $\mathbf{M}_0, j < -0.01$, which has been proven sufficient (Pakmor et al. 2016a). Corners detected below this threshold are treated in a special way as described below.

The required value of the magnetic field at the center of the interface is determined via weighted averages of the values of neighboring corners while considering the area in the direction of the respective corner (see Figure 2 of Pakmor et al. 2016a). Calculating the gradient of CR energy density is done separately for the part of the gradient that lies normal to the surface of the interface $\nabla\epsilon_{\mathrm{cr,n}}$ and the part that is within the interface. Here, only the component parallel to the magnetic field in the interface $\nabla\epsilon_{\mathrm{cr,t}}$ is considered because the other perpendicular component cancels out. To restrict the CR flux to flow from cells with higher CR energy density to cells with lower CR energy, a gradient limiter is implemented. Here, a generalized version of the van-Leer limiter (van Leer 1984) is used to calculate the gradient $\nabla\epsilon_{\mathrm{cr,t}}$ in the interface along the magnetic field using the unlimited gradients in the same direction $\nabla\epsilon^i_{\mathrm{cr,t}}$ at corner i. In case $\nabla\epsilon^i_{\mathrm{cr,t}}$ have the same sign, $\nabla\epsilon_{\mathrm{cr,t}}$ is calculated as

$$\nabla\epsilon_{\mathrm{cr,t}} = \frac{N}{\sum_i \left(\nabla\epsilon^i_{\mathrm{cr,t}}\right)^{-1}}, \tag{2.73}$$

where N describes the number of dimensions. The problematic corners mentioned previously are neglected in the sum. In the special case of all corners being flagged, the stricter minmod limiter is used. Also, if all $\nabla\epsilon^i_{\mathrm{cr,t}}$ do not all carry the same sign, $\nabla\epsilon_{\mathrm{cr,t}}$ is set to zero.

The normal gradients $\nabla\epsilon_{\mathrm{cr,n}}$ can be calculated in two ways. These are either referred to as *full* or *simple* normal gradients. The simple normal gradient is only based on the values at the two centers of the cells (L,R) sharing the interface in question. The gradient estimation is then projected onto the normal of the interface.

$$\nabla\epsilon_{\mathrm{cr,n}} = \frac{\epsilon_{\mathrm{cr,L}} - \epsilon_{\mathrm{cr,R}}}{|\boldsymbol{s}_{\mathrm{L}} - \boldsymbol{s}_{\mathrm{R}}|} \frac{\boldsymbol{s}_{\mathrm{L}} - \boldsymbol{s}_{\mathrm{R}}}{\boldsymbol{s}_{\mathrm{L}} - \boldsymbol{s}_{\mathrm{R}}} \cdot \boldsymbol{n}_{\mathrm{face}} \tag{2.74}$$

The mesh generating point is by definition parallel to the interface. Thus, if mesh generating point and center of mass align perfectly the estimate is fairly accurate. Possible misalignments slightly underestimate the true gradient.

The full normal gradient is calculated by analogy with the magnetic field, i.e. via weighted averages with respect to the area covered in the direction of neighboring corners of the respective interface. The value of flagged corners is replaced by the simple normal gradient estimate which is weighted with the area in the direction of this corner. The simple normal gradient is by

construction in agreement with the entropy constraint. If the calculated full normal gradient violates the constraint, it is replaced with the simple normal gradient estimate.

As mentioned above explicit time integration is heavily constrained by the global time limit for diffusion $\Delta t_{\rm diffusion}$, which is given by

$$\Delta t_{\rm diffusion} < \frac{\Delta x^2}{\kappa_\epsilon}, \tag{2.75}$$

where Δx is the linear scale of a cell and κ_ϵ is the diffusion coefficient. This van-Neumann time step criterion follows from stability considerations. Consequently, we use a semi-implicit time integration which is stable on longer timescales. For this, the CR energy density is advanced in time by only considering the flux contribution due to gradients in the interfaces. Here, an *explicit* forward Euler time integrator is necessary due to the non-linearity of the tangential gradient estimate, $\nabla \epsilon^n_{\rm cr,t,ij}$, for which a flux limiter is used. The latter makes the problem non-linear, which would result in a very expensive implicit algorithm. The updated CR energy density due to fluxes in the interface $\epsilon^{\tilde{n}}_{{\rm cr},i}$ is then given by

$$\epsilon^{\tilde{n}}_{{\rm cr},i} = \epsilon_{{\rm cr},i} + \frac{\Delta t}{V_i} \sum_j \kappa_{ij} (\boldsymbol{b}_{ij} \cdot \nabla \epsilon^n_{\rm cr,t,ij}) \; \boldsymbol{b}_{ij} \cdot \boldsymbol{n}_{ij} A_{ij} \tag{2.76}$$

Afterwards, contributions from the flux due to the gradient normal to the interfaces are considered. Here, an *implicit* backward Euler scheme can be utilized for the linear gradients. The value at the next time step of the CR energy density $\epsilon^{n+1}_{{\rm cr},i}$ can then be determined by

$$\epsilon^{n+1}_{{\rm cr},i} = \epsilon^{\tilde{n}}_{{\rm cr},i} + \frac{\Delta t}{V_i} \sum_j \kappa_{ij} (\boldsymbol{b}_{ij} \cdot \nabla \epsilon^{n+1}_{\rm cr,n,ij}) \; \boldsymbol{b}_{ij} \cdot \boldsymbol{n}_{ij} A_{ij} \tag{2.77}$$

The scheme has proven to be stable for very large time steps. However, there are cases where the solution becomes incorrect and the entropy constraint can be violated (Pakmor et al. 2016a).

Alfvén cooling

The generated Alfvén waves by the CRs are damped via non-linear Landau damping and turbulent damping. Damping processes take energy out of the waves and transfer it to the gas, increasing thermal energy. The relevant term in Equation 2.65 describing the change in CR energy density per unit time $v_{\rm st} \cdot \nabla P_{\rm cr}$ can be simplified using Equation 2.67 to

$$\Delta \dot{\epsilon}_{\rm cr,A} = v_{\rm st} \cdot \nabla P_{\rm cr} = -\frac{\boldsymbol{B} \cdot \nabla P_{\rm cr}}{|\boldsymbol{B} \cdot \nabla P_{\rm cr}|} \frac{\boldsymbol{B}}{\sqrt{\rho}} \cdot \nabla P_{\rm cr} = -\frac{|\boldsymbol{B} \cdot \nabla P_{\rm cr}|}{\sqrt{\rho}} \tag{2.78}$$

All these quantities are readily available to the code. Consequently, multiplying $\Delta \dot{\epsilon}_{\rm cr,ac}$ with the time step Δt of the individual cell yields the gain and loss of energy density for the gas and CRs, respectively. This is also evident from the signs in front of those terms in Equation 2.65.

Collisional loss processes

CRs lose energy through high impact parameter interactions with thermal electrons and CR momentum is also transfered to the gas through excitations of quantized plasma oscillations in low impact parameter interactions. Both loss terms are summarized as Coulomb losses, which effectively transfer energy from CRs to the thermal gas. On the other hand, CRs can collide inelastically with thermal protons to produce pions and to lose CR energy. The latter process produces secondary electrons, which radiate energy via non thermal interactions and partially

heat the ambient medium. Thereby, these so called hadronic losses at least partially heat the ambient medium.

Hadronic losses mostly effect highly energetic CRs and are approximately independent of CR momentum. Thus, the exact spectral shape can be neglected. However, Coulomb losses linearly depend on CR momentum and low momentum CRs are most significantly affected. Consequently, the spectral shape of the CR momentum is expected to stay invariant at the high end but low-energy CRs transfer their energy to the thermal gas. Hence, we assume an equilibrium momentum distribution of CRs where injection balances both forms of losses. This is a valid approximation for times larger than the timescale of significant variability in the injection process (Pfrommer et al. 2017).

The kinetic energy of a proton with dimensionless momentum $p = P_\mathrm{p}/(m_\mathrm{p}c)$ is given by

$$E_\mathrm{p}(p) = \left(\sqrt{1+p^2} - 1\right) m_\mathrm{p}c^2. \tag{2.79}$$

The kinetic energy loss of a proton with $\gamma \ll m_\mathrm{p}/m_\mathrm{e}$ due to Coulomb losses (neglecting recoils) is given by (Gould 1972)

$$-\left(\frac{\mathrm{d}E_\mathrm{p}(p)}{\mathrm{d}t}\right)_\mathrm{Coul} = \frac{4\pi e^4 n_\mathrm{e}}{m_\mathrm{e}\beta c}\left[\ln\left(\frac{2m_\mathrm{e}c^2\beta p}{\hbar\omega_\mathrm{pl}}\right) - \frac{\beta^2}{2}\right] \equiv \frac{A_\mathrm{Coul}}{\beta}, \tag{2.80}$$

where $\omega_\mathrm{pl} = \sqrt{4\pi e^2 n_\mathrm{e}/m_\mathrm{e}}$ is the plasma frequency, n_e is the number density of free electrons and $\beta = v_\mathrm{p}/c = p/\sqrt{1+p^2}$ is the dimensionless CR velocity. To obtain the equilibrium solution, the term βp in the Coulomb logarithm is replaced by its average $\langle\beta p\rangle = 3P_\mathrm{cr}/(m_\mathrm{p}c^2 n_\mathrm{rc})$. Lastly, a characteristic Coulomb timescale τ_Coul can be defined as

$$\tau_\mathrm{Coul} \equiv \frac{\epsilon_\mathrm{cr}}{|\mathrm{d}\epsilon_\mathrm{cr}/\mathrm{d}t|_\mathrm{Coul}}. \tag{2.81}$$

If the kinematic CR energy exceeds the threshold value of $p_\mathrm{thr}m_\mathrm{p}c = 0.78$ GeV$/c$ CR protons inelastically collide with thermal protons to mainly form pions. Neutral pions decay after 9×10^{-17} s mostly to gamma rays whereas charged pions decay via the chain (Patrignani et al. 2016).

$$\begin{aligned} &\pi^\pm \rightarrow \mu^\pm + \nu_\mu/\bar{\nu}_\mu \rightarrow e^\pm + \nu_e/\bar{\nu}_e + \nu_\mu + \bar{\nu}_\mu \\ &\pi^0 \rightarrow 2\gamma \end{aligned} \tag{2.82}$$

About 1/6 of the initial energy of the charged pions ends up in secondary electrons and positrons. The mildly relativistic subpopulation of the latter ($\gamma_e \lesssim 200$) eventually thermalize their energy via Coulomb collisions (Rephaeli 1979; Sarazin 1999). High energy electron losses ($\gamma_e \gtrsim 1,000$) are completely dominated by synchrotron and Compton scattering.

The hadronic energy loss of a CR proton population is independent of the exact proton momenta and given by (Pfrommer et al. 2017)

$$-\left(\frac{\mathrm{d}E_\mathrm{p}}{\mathrm{d}t}\right)_\mathrm{hadr} = n_\mathrm{N}\sigma_\mathrm{pp}K_\mathrm{p}m_\mathrm{p}c^3(\gamma-1)\theta(p-p_{thr}) \equiv A_\mathrm{hadr}(\gamma-1)\theta(p-p_\mathrm{thr}), \tag{2.83}$$

where $\sigma_\mathrm{pp} \approx 44.2$ mbarn is the total pion cross section (Pfrommer and Enßlin 2004), $K_\mathrm{p} \approx 1/2$ describes the inelasticity of the hadronic reaction in the limiting regime (Mannheim and Schlickeiser 1994) and $n_\mathrm{N} = n_e/(1-X_\mathrm{He}/2)$ is the target nuclear density in the ICM, assuming a primordial element composition of $X_\mathrm{He} = 0.24$. The Heaviside distribution θ is unity for

positive values and zero otherwise. By analogy with the Coulomb case a timescale for hadronic losses $\tau_{\rm hadr}$ is defined as

$$\tau_{\rm hadr} \equiv \frac{\epsilon_{\rm cr}}{|{\rm d}\epsilon_{\rm cr}/{\rm d}t|_{\rm hadr}} \tag{2.84}$$

To estimate the collisional losses an equilibrium CR distribution is derived balancing continuous injection and discussed losses (following Enßlin et al. 2007). We assume a homogeneous environment and an isotropic one-dimensional CR distribution in momentum space, $f_p^{(1)}(p,t) = 4\pi p^2 f_p(p,t)$ and a CR injection spectrum $Q^{(1)}$ of the form

$$Q^{(1)}(p) = Q_{\rm inj}\ p^{-\alpha_{\rm inj}}\ \theta(p-p_1), \tag{2.85}$$

where p_1 is the low-momentum cutoff. Steady state solutions, $\partial f_p^{(1)}/\partial t = 0$, of the Fokker-Planck equation are obtained neglecting Coulomb/hadronic losses for high/low CR momenta, respectively. The resulting momentum distribution function $f_p^{(1)}(p)$ is given by

$$f_p^{(1)}(p) = \frac{Q_{\rm inj} p^{-\alpha_{\rm inj}}}{(\alpha_{\rm inj}-1)A_{\rm Coul}} \times \begin{cases} p^3 & p_1 \ll p \ll p_* \\ p_*^3 & p \gg p_* \end{cases} \tag{2.86}$$

where p_* is the intersection momentum, which depends only on the ratio of the Coulomb-to-hadronic loss rates as $p_* = \sqrt[3]{A_{\rm Coul}/A_{\rm hadr}} \approx 1.1$. In the following, a matched asymptotic solution to the approximated steady-state solution is used, which reads

$$f_p^{(1)} = \frac{Q_{\rm inj}\ p^{-\alpha_{\rm inj}}\ \theta(p-p_1)}{(\alpha_{\rm inj}-1)\ A_{\rm Coul}\ (p_*^{-3}+p^{-3})}. \tag{2.87}$$

The CR energy loss rates can now readily be obtained. The Coulomb loss rate of the CR population yields

$$\Lambda_{\rm Coul} = \int_{p_1}^{\infty} f_p^{(1)} \left(\frac{{\rm d}E_p}{{\rm d}t}\right)_{\rm Coul} {\rm d}p = -2.78\times10^{-16} \left(\frac{n_e}{\rm cm^{-3}}\right)\left(\frac{\epsilon_{\rm cr}}{\rm erg\ cm^{-3}}\right) {\rm erg\ s^{-1}\ cm^{-3}}, \tag{2.88}$$

where the normalization of the injection function $Q_{\rm inj}$ is expressed through the CR energy density $\epsilon_{\rm cr}$. In agreement with CR injection by jets of AGNs, $p_1 = 0.1$ and $\alpha_{\rm inj} = 2.2$ are used. The Coulomb loss rate $\Lambda_{\rm Coul}$ depends only weakly on the exact cutoff value p_1 but more significantly on $\alpha_{\rm inj}$ as $\Lambda_{\rm Coul} = -1.35\times10^{-16}$ to -12.8×10^{-16}erg s^{-1} cm^{-3} for $\alpha_{\rm inj} = 2.1$ to 2.7.

Similarly, the following expression for the hadronic loss rate $\Lambda_{\rm hadr}$ is obtained, yielding

$$\Lambda_{\rm hadr} = \int_{p_1}^{\infty} f_p^{(1)} \left(\frac{{\rm d}E_p}{{\rm d}t}\right)_{\rm hadr} {\rm d}p = -7.44\times10^{-16} \left(\frac{n_e}{\rm cm^{-3}}\right)\left(\frac{\epsilon_{\rm cr}}{\rm erg\ cm^{-3}}\right) {\rm erg\ s^{-1}\ cm^{-3}}, \tag{2.89}$$

where the sensitivity to $\alpha_{\rm inj}$ is less severe as $\Lambda_{\rm Coul} = -8.1\times10^{-16}$ to -5.6×10^{-16}erg s^{-1} cm^{-3} for $\alpha_{\rm inj} = 2.1$ to 2.7. One can see that the Coulomb loss rate is sub-dominant for hard injection indexes $\alpha_{\rm inj} \lesssim 2.4$ whereas they dominate over hadronic losses for softer indexes.

In summary, the energy loss rate of CRs due to collisional losses can be described as $\Lambda_{\rm cr} = \Lambda_{\rm hadr} + \Lambda_{\rm Coul} = -\lambda_{\rm cr} n_{\rm e} \epsilon_{\rm cr}$ with rate coefficient $\lambda_{\rm cr} = 1.022\times10^{-15}$ cm^3 s^{-1}. Thus, the CR energy is updated following the solution

$$E_{\rm cr}(t) = E_{\rm cr}(t_0){\rm e}^{-\lambda_{\rm cr} n_e t} \tag{2.90}$$

Turning to the consequences for the thermal energy of the gas, all Coulomb losses of the CRs are heating the gas. For the hadronic losses the majority of energy escapes in the form of neutrinos

or γ-ray radiation. As mentioned above, only 1/6 of the energy ends up in secondary electrons. Their fate depends on the Lorentz factor of the electrons. On average secondary electrons are expected to have an energy of $\langle E_{e^\pm} \rangle = m_{\pi^\pm} c^2/4 = 35$ MeV $= 68\ m_\mathrm{e} c^2$, which corresponds to medium relativistic electrons that thermalize in the surrounding plasma. Consequently, the collisional heating rate of the gas is given by $\Gamma_\mathrm{th} = -\Lambda_\mathrm{Coul} - \Lambda_\mathrm{hadr}/6 = \lambda_\mathrm{th} n_e \epsilon_\mathrm{cr}$ with the rate coefficient for collisional heating of the ambient plasma $\lambda_\mathrm{th} = 4.02 \times 10^{-16}$ cm^3 s^{-1}. The thermal energy gain is then implemented as

$$E_\mathrm{th}(t) = E_\mathrm{cr}(t_0) \left(1 - \mathrm{e}^{-\lambda_\mathrm{cr} n_e t}\right) \tag{2.91}$$

The outlined approach is clearly valid if CR injection is balanced by collisional cooling and for a freely cooling CR population at late times. However at early times the Coulomb cooling rate is substantially lower in comparison to a more realistic spectral treatment (Pfrommer et al. 2017).

3 Methods

3.1 Magnetic field setup

To study the dynamics of an AGN inflated bubble rising buoyantly in the ICM, we model an idealized Perseus-like CC cluster. A compromise is made between a controllable setup and a realistic cluster environment. Modelling a turbulent magnetic field appears critical as it is expected to significantly stabilize the bubble (Section 2.1.5) and shape the dynamics of the escaping CRs that diffuse along magnetic field lines. The magnetic field is assumed to follow a Kolmogorov spectrum in k-space as required by observations (Bonafede et al. 2010). The magnetic field is scaled in such a way that a constant plasma beta factor is obtained throughout the cluster. This value is a compromise between purely isotropic collapse and pure contraction perpendicular to the magnetic field orientation (see Section 2.1.5).

The method for the setup of the turbulent magnetic field with average value $\langle \mathbf{B} \rangle = 0$ is based on Appendix A in Ruszkowski et al. (2007). Here, the simulation box is however significantly larger, which makes it necessary to combine multiple nested meshes with adaptive resolution such that expensive operations (regarding memory and calculation time) are still feasible during the mesh-generation process. A further complication in our setup is the unstructured nature of the mesh in AREPO. Because we utilize numerous Fourier transformations in the following, the magnetic field is setup on multiple Cartesian meshes and, after the final step interpolated to a mesh comprised of cubic cells with individual masses that agree with the mass refinement employed by the code. This mesh is then relaxed to a honeycomb-like structure, which is the more natural and most effective configuration of an AREPO mesh.

The three components of the magnetic field are treated independently of each other. The following explanation, focusing on one component B_i, thus applies to all three components ($i \in [0, 1, 2]$). Similarly, the following description focuses on the setup of a single mesh whereas we set up all meshes with different mesh spacings accordingly. The final Gaussian-distributed field component follows a one-dimensional power spectrum $P_{B_i}(k)$ of the form

$$P_{B_i}(k) \propto \begin{cases} k^2, & k < k_{\mathrm{inj}} \\ k^{-5/3}, & k_{\mathrm{inj}} \leq k \end{cases} \tag{3.1}$$

where the power spectrum is defined by $P_{B_i}(k) \propto k^2 |\tilde{B}_i(k)|^2$ with the Fourier transform of the magnetic field component $\tilde{B}_i(k)$. The magnetic field follows a white noise distribution from field fluctuations on the largest scale (smallest k-values) down to the injection scale k_{inj}. On scales smaller than k_{inj}, the spectrum declines as a power-law with a Kolmogorov spectral index. In discretized space the magnetic field component $B_{i,\boldsymbol{x}}$ is defined at a discrete set of vectors in real space $\boldsymbol{x}$. By analogy with the Fourier transforms of the magnetic field, $\tilde{B}_{i,\boldsymbol{k}}$ is defined at a discrete set of k-vectors $\boldsymbol{k}$. The algorithm starts in k-space where $\boldsymbol{k}$ is inserted into the auxiliary function $f_k(k)$ defined as

$$f_k(k) = \begin{cases} A, & k < k_{\mathrm{inj}} \\ \frac{A}{k_{\mathrm{inj}}^{-11/3}} k^{-11/3}, & k_{\mathrm{inj}} \leq k \end{cases} \tag{3.2}$$

with normalisation factor A. The function $f_k(k)$ is proportional to $\tilde{B}^2_{i,\boldsymbol{k}}$ and only depends on the absolute value of the k-vector $k = |\boldsymbol{k}|$. Now, the values of the magnetic field components

$\tilde{B}_{i,\boldsymbol{k}}$ are drawn from a Gaussian random sample with root mean square (RMS) given by the square root of $f_{\rm aux}(k)$ for each k value for the real and imaginary value of $\tilde{B}_{i,\boldsymbol{k}}$.

For two randomly drawn values $X_1, X_2 \in [0, 1)$, two Gaussian random variables Y_1, Y_2 can be drawn using

$$\begin{aligned} \phi &= 2\pi X_1, \\ r &= \sqrt{-2\sigma^2 \ln(X_2)}, \\ [Y_1, Y_2] &= [r\cos(\phi), r\sin(\phi)]\,, \end{aligned} \tag{3.3}$$

where σ_R^2 is the variance given by $f_{\rm aux}(k)$, i.e. $\sigma_R^2 = f_{\rm aux}(k)$. The two resulting values Y_1, Y_2 per cell in k-space are set to the imaginary and real part of the k-space magnetic field components $\mathrm{Im}(\tilde{B}_{i,\boldsymbol{k}}) = Y_1, \mathrm{Re}(\tilde{B}_{i,\boldsymbol{k}}) = Y_2$. The spectrum can then be normalized to the desired RMS value of the magnetic field components in real space σ_B using Parseval's theorem

$$\sigma_B^2 = \frac{1}{N^2} \sum_{\boldsymbol{k}} |B_{i,\boldsymbol{k}}|^2, \tag{3.4}$$

where the sum extends over all k-values, of which there are a total of N. Inverting the function yields the normalization A depending on the desired σ_B.

We employ the adaptive mesh refinement scheme in AREPO, which ensures that cell mass is on the order of the target mass and, analogously, the volume for the jet cells. Thus, the final magnetic field is interpolated to an unrelaxed mesh $M_{\rm ur}$, which is made up of cubic cells whose mass is in the range of the target cell mass $m_{\rm target}$ that AREPO will later refine/derefine to. Consequently, relatively small cells are expected in the denser center of the cluster. These are too small in order to initially create one magnetic field on a single Cartesian mesh $M_{\rm Ini}$ with the constraint that every cell of $M_{\rm Ini}$ is smaller than every cell of $M_{\rm ur}$. Instead, one starts out with an initial mesh M_0 placed in the center of the cluster with cell sizes equal to the smallest cell in $M_{\rm ur}$. The number of cells N in M_0 is chosen to be as high as possible while necessary algorithms for the magnetic field creation are still feasible concerning memory and computational time. Mesh M_1 with again N cells is then placed in the center of the cluster with cell sizes of the smallest cells bordering the outer edges of M_0. This process is continued until the biggest mesh covers the desired box size of the simulation. Hereby, coarser meshes are introduced in the outskirts of the magnetic field.

Continuing with the magnetic field creation, a loop over the following five steps is then responsible for creating an almost divergence free magnetic field with smooth transition areas so that a simple interpolation of the magnetic field from mesh M_i to M_{i+1} is possible.

(i) *Divergence cleaning in k-space.* The divergence in k-space simply corresponds to the multiplication $\boldsymbol{k} \cdot \boldsymbol{B}$. Thus, the divergence of the magnetic field can be projected out via the transformation

$$\tilde{\boldsymbol{B}}_{\boldsymbol{k}} \rightarrow \tilde{\boldsymbol{B}}_{\boldsymbol{k}} - \hat{\boldsymbol{k}}(\hat{\boldsymbol{k}} \cdot \tilde{\boldsymbol{B}}_{\boldsymbol{k}}) \tag{3.5}$$

(ii) *Inverse FFT of $\tilde{\boldsymbol{B}}_{\boldsymbol{k}}$ to $\boldsymbol{B}_{\boldsymbol{x}}$.* We use the scipy library *fft* for (inverse) Fourier transforms. The so-called *fast Fourier transform* (FFT) is an optimized algorithm of the Fourier transform, which in general would scale as N^2. However, through a divide and conquer strategy the scaling is drastically reduced to $N \log N$ (Cooley and Tukey 1965). As the magnetic field $\boldsymbol{B}_{\boldsymbol{x}}$ only has a real component and an identically vanishing imaginary part, only half the information is actually needed to calculate the FFT. Scipy would also provide an optimized algorithm for real FFT. However, for full control, we use the

normal algorithm. Consequently, the k-space magnetic field components $B_{i,\boldsymbol{k}}$ have to follow certain constraints to receive a real magnetic field $B_{i,\boldsymbol{x}}$. They are given by

$$\tilde{\boldsymbol{B}}^*_{i,\boldsymbol{k}} = \tilde{\boldsymbol{B}}^*_{i,-\boldsymbol{k}} \tag{3.6}$$

where the asterisk donates the complex conjugate.

(iii) *Rescaling of the magnetic field to achieve an on average constant magnetic-to-thermal pressure ratio.* The average magnetic field between radii r_i and r_{i+1} in a shell around the center of the cluster is rescaled such that the average magnetic-to-thermal pressure ratio $x_{B,\mathrm{ext}} = \overline{P_B/P_{\mathrm{th}}}$ within the resulting shell is constant.

(iv) *Applying a projection operator to isolate meshes magnetically.* As described above, the magnetic field is created on multiple meshes M_j with $j \in [0, 1, ..., \Omega]$. Overlapping regions of the meshes should not be interpolated in order to not double count contributions at a certain distance from the center $\boldsymbol{r}$. Only a thin merging layer at radius $\boldsymbol{r}_m$ with width d_m is created through a spline which smoothly sets the magnetic field values to zero. This layer is comprised of two independent fields and thus, possesses magnetic divergences. These divergences are removed by projecting out field lines that cross the interface. For this, a projection of the following form is used

$$\boldsymbol{B}_{\boldsymbol{x}} \rightarrow \boldsymbol{B}_{\boldsymbol{x}} - g(r_{\boldsymbol{x}})\hat{\boldsymbol{r}}_{\boldsymbol{x}}(\hat{\boldsymbol{r}}_{\boldsymbol{x}} \cdot \boldsymbol{B}_{\boldsymbol{x}}), \tag{3.7}$$

where $\hat{\boldsymbol{x}}$ is the normalized distance to the border from cell $\boldsymbol{x}$ and the function $g(r_{\boldsymbol{x}})$ is given by

$$g(r_{\boldsymbol{x}}) = \begin{cases} 1 - \left|\cos\left(\pi \frac{y+\Delta y-1}{2\Delta y}\right)\right|, & 1-\Delta y < y < 1+\Delta y \\ 0, & \text{otherwise} \end{cases} \tag{3.8}$$

with $y = r/r_{\mathrm{sph}}$, $\Delta y = 0.05$ and the radius of the to be isolated spherical shell r_{sph} which is for simplicity set to r_m . The expression $2\Delta y$ corresponds to the width of the resulting layer where the normal component to the shell surface has been smoothly removed.

(v) *Creating smooth transitions between neighboring meshes M_j and M_{j+1}.* Now, the magnetic field lines $B_{\boldsymbol{x},j}$ of mesh M_j are smoothly removed beyond the merging radius r_m out to the width of the merging layer d_m and completely removed beyond this point. This is done by multiplying $\boldsymbol{B}_{x,j}$ of mesh M_j with the spline $f_S(x)$ given by

$$f_S(x) = \begin{cases} 1, & 0 < r < r_m \\ \frac{1}{2}\left(\cos\left(\frac{\pi(r-r_m)}{d_m}\right) + 1\right), & r_m \leq r \leq r_m + d_m \\ 0, & r_m + d_m < r \end{cases} \tag{3.9}$$

smoothly setting its outer regions to zero. For the larger mesh M_{j+1}, the matching spline $\hat{f}_S(x)$ is given by

$$\hat{f}_S(x) = \begin{cases} 0, & 0 < r < r_m \\ 1 - \frac{1}{2}\left(\cos\left(\frac{\pi(r-r_m)}{d_m}\right) + 1\right), & r_m \leq r \leq r_m + d_m \\ 1, & r_m + d_m < r \end{cases} \tag{3.10}$$

and is then multiplied with $B_{\boldsymbol{x},j+1}$ to smoothly remove the inner shell at $r_m + d_m$. Only the outer shell of M_Ω and the inner shell of M_0 remain untouched. The width of the smoothly dropping region d_m is set to the larger cell size of the two bordering meshes. The latter

is a harsh criteria for the larger mesh of the two as the spline is basically constructed in only one cell. We require cell sizes of M_j to be smaller at any point than in mesh $M_{\rm ur}$, which turns out to be a challenging constraint, at least for the initial conditions used for the high resolution runs ($m_{\rm target} = 1.5 \times 10^6 M_\odot$, $N = (2^9)^3 \sim 10^8$).

The described operations (iii) through (v) introduce magnetic divergence. Analogously to Ruszkowski et al. (2007), we find that the divergence continuously decreases when iterating over steps (i) through (v). The iteration process does not converge quickly so that the number of iterations becomes a trade-off between smaller divergence and computational time. Fortunately, the Powell scheme seems to be very stable in handling residual divergences similarily to the results by Pakmor and Springel (2013).

An illustrative example of a created magnetic field at the lower resolution employed later is shown in Figure 3.1. Two 2D slices of the same magnetic field component are shown. On the left, we show the magnetic field after creation (before step (i)). The right-hand side shows the magnetic field component after the divergence cleaning algorithm as described in step (i) has been used, employing the same color bar that ranges from high magnetic field strengths (dark red) to the extrema in the opposite direction (dark blue). The axis labels give the distance in Mpc from the center of the cluster. The sharp unrealistic drops in magnetic field strength seen on the left are clearly smoothed out to a more realistic magnetic field landscape.

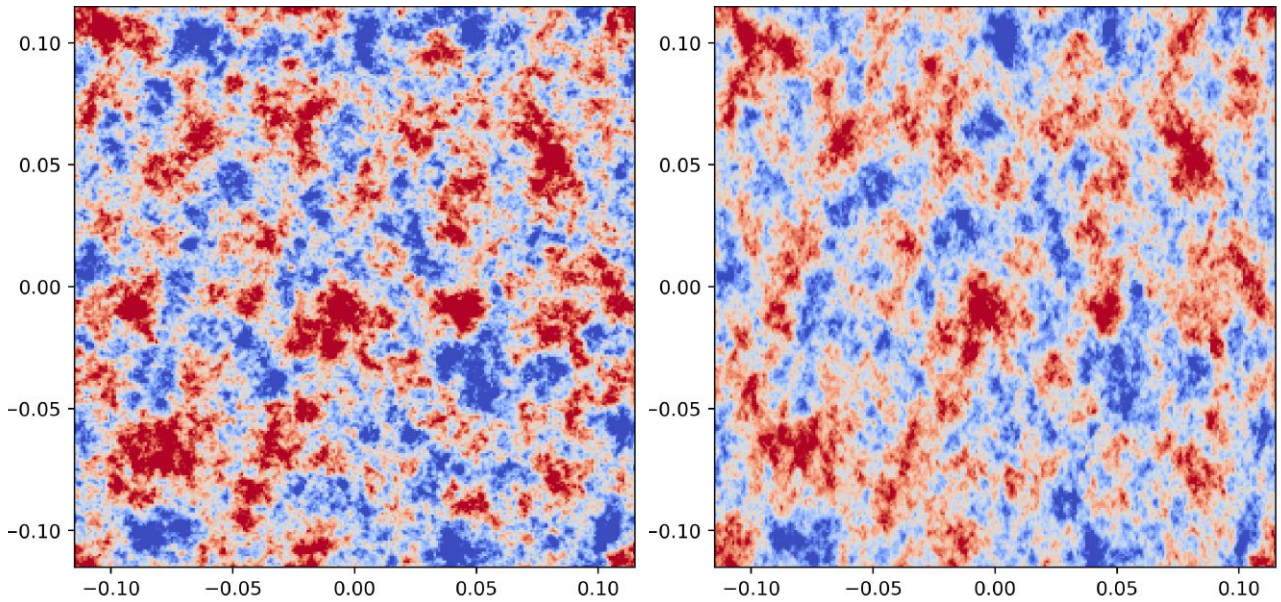

Figure 3.1: On the left, we show the magnetic field component directly after setup in k-space. On the right, we show the same magnetic field component after divergence has been cleaned in k-space. The magnetic field is clearly smoothed out to a more realistic continuous magnetic field with shadings through the process of divergence cleaning.

The same magnetic field component but for meshes M_0 and M_1 is shown in Figure 3.2 after the spline and smoothing has been applied. To cover the whole simulation box (1.5 Mpc), a third mesh (not shown) is needed where the spline has only been applied at the center of that mesh using the same color bar as for Figure 3.1. The magnetic field shows the required decrease in its radial profile and the effect of the spline at its edges.

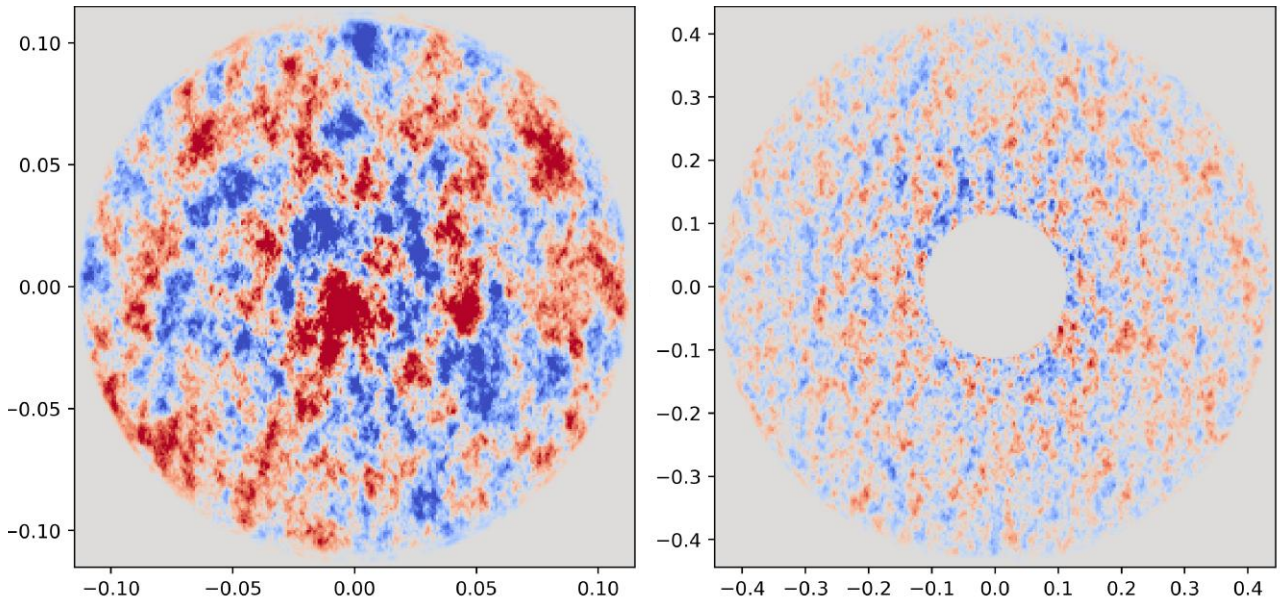

Figure 3.2: On the left we show the magnetic field component of mesh M_0 after the magnetic field in direction of the edge component has been projected out. On the right we show the same magnetic field component of the next coarser mesh M_1.

For the extrapolation, the magnetic field of meshes M_{j+1} are simply added onto the respective cells of meshes M_j, which has become possible through the usage of the splines $f_S(x)$ and $\hat{f}_S(x)$ as discussed in step (v). Afterwards, the magnetic field of all meshes M_j is interpolated onto mesh M_{ur} that is used for the relaxation step resulting in the creation of the actual initial conditions. The interpolation to the magnetic field $B_{z,\text{ur}}$ of mesh M_{ur} is done in a volume weighted fashion

$$\boldsymbol{B}_{z,\text{ur}} = \frac{\sum_{\boldsymbol{x},j} V_{\boldsymbol{x},j} \boldsymbol{B}_{\boldsymbol{x},j}}{\sum_{\boldsymbol{x},j} V_{\boldsymbol{x},j}} \tag{3.11}$$

where the sum goes over all cells $\boldsymbol{x}$ of all meshes M_j that overlap with cell z with a nonzero magnetic field contribution. The cell size of all cells $\boldsymbol{x}$ is by construction smaller or equal to the cell size of cell z, i.e. $V_{\boldsymbol{x}} \leq V_z$. Consequently, there will always be magnetic field contributions from more than one cell making up the magnetic field of cell z.

Due to the vector nature of the magnetic field, magnetic field contributions will cancel each other when applying Equation 3.11, which reduces the magnetic field strength. Thus, the magnetic field is uniformly rescaled, which leaves the magnetic divergence invariant. Outer cells, which are much larger in comparison to the cells in the center of the cluster, will suffer more significantly from this effect. Due to this inhomogeneity, the rescaling factor is chosen such that the desired average value of $x_{B,\text{ext}}$ is maintained in the inner 300 kpc of the cluster, which includes the for the analysis relevant region.

A rescaled and extrapolated magnetic field component is shown in Figure 3.3 including a zoomed in image of the same magnetic field. The field component again runs in vertical direction. The drop in magnetic field in the transition area between two neighboring meshes M_j is still visible in the vertical direction.

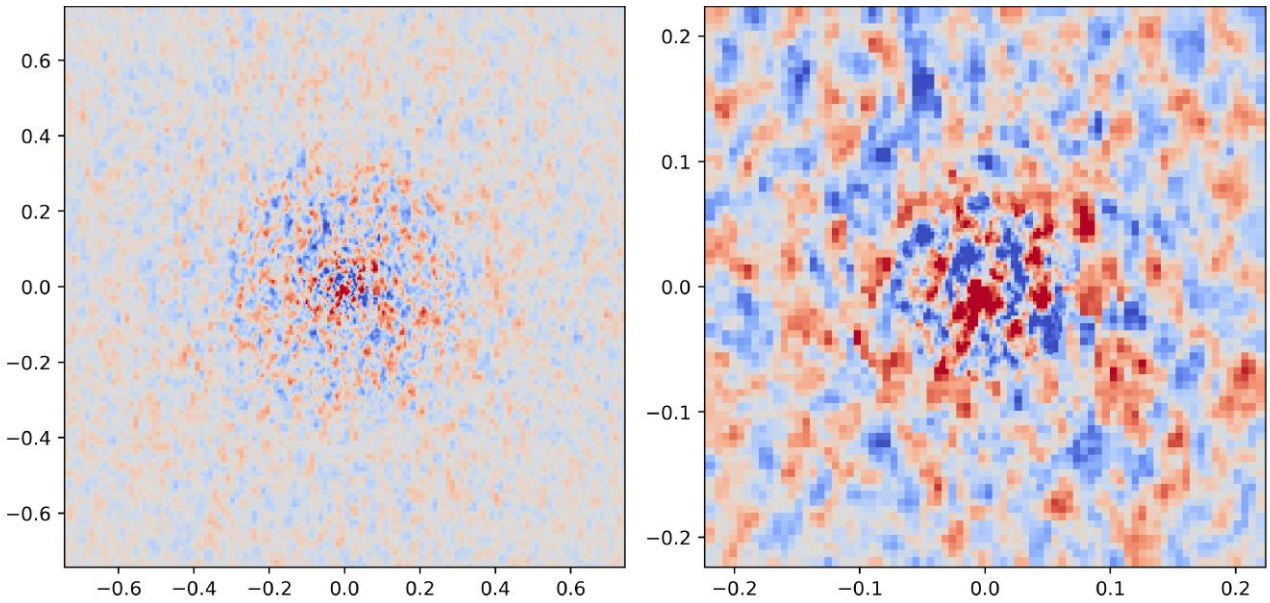

Figure 3.3: On the left we show the whole rescaled extrapolated magnetic field component onto mesh $M_{\rm ur}$ in vertical direction. On the right we show the same magnetic field component zoomed onto the center of the cluster.

Finally, the mesh is relaxed prior to the actual run of the simulation. This is done in order to relax the cubic cells to a honeycomb-like structure. For Cartesian meshes, the mesh construction is challenging for the algorithm as it corresponds to a special case of the Voronoi tessellation, which slows down the computation significantly. Thus, the initial conditions are prepared in this way to run the following simulations more smoothly. Relaxing a turbulent magnetic field has the obvious effect of reducing the turbulence and thereby the amplitude of the magnetic field. The relaxation process is thereby a compromise between mesh relaxation and maintaining magnetic field fluctuations. The chosen relaxation time $t_{\rm relax} \sim 3$ Myr is also used by the code to advect part of the remaining magnetic divergences. After completion the same rescaling algorithm is applied to start the simulation with the desired $x_{B,\rm ext}$.

3.2 Jet implementation

Jet physics spans ~ 10 orders of magnitude in scale starting from the scales of SMBH, which powers the jets, up to the Mpc scale of lobes created by the jet. Thus, as our numerical models focus on the bubble physics, we have to resort to subscale modeling of the jet. The implementation is described in detail in Weinberger et al. (2017). In the following, a summary of the implementation details will be given, which was tested thoroughly as part of this thesis.

The jet module is designed in order to produce extragalactic jets at a linear resolution of 400 pc but, most importantly, its applicability in the future to more complex self-regulated systems to test the viability of CR heating as a major heating mechanism for CCs has to be maintained. This point is crucial for the injection step. In addition, the module should give viable results in cosmological simulations to test the CR heating theory in the most realistic environments possible. For the latter, downscaling of the resolution while still obtaining essentially similar results to the high resolution runs is crucial and the module runs on local timesteps (Weinberger et al. 2017).

As discussed before, the actual launch mechanism is not simulated due to computational constraints and the exact mechanism is still an open question of research. Instead, the collimated under-dense jet is set up in pressure equilibrium with initially dominant kinetic energy.

A toroidal magnetic field and CRs can be added. We ensure energy conservation while setting up the jet. The jet is active when the available energy to the jet, $\dot{E}_{\rm jet}$, exceeds the required energy to redistribute the gas and inject the required amount of CRs, $\Delta E_{\rm redist}$, as well as the predefined amount of magnetic field strength, ΔE_B. The remaining energy is put into kinetic energy, $\Delta E_{\rm kin}$. Conclusively, the jet is active after time t of the last injection event at time $t_{\rm last}$ if injection and redistribution energy amount to less than the acquired jet energy during this period, i.e.,

$$\Delta E_{\rm kin} \geq \int_{t_{\rm last}}^{t} \dot{E}_{\rm jet}(t)\mathrm{d}t - \Delta E_B - \Delta E_{\rm redist}. \tag{3.12}$$

Thus, the jet is not continuously injecting energy into the ambient medium but rather during single injection events. During a typical interval of jet activity of 50 Myr, several thousand injection events occur (Weinberger et al. 2017). Here, the available energy to the jet $\dot{E}_{\rm jet}$ is constantly added every time step. However, the available power can also be coupled to the time-dependent accretion process of the SMBH to mimic a realistic situation.

The amount of injected CRs and magnetic field strength can be set through the desired CR-to-thermal pressure ratio $x_{\rm cr,jet}$ and the desired average magnetic-to-thermal pressure $x_{B,\rm jet}$ in the jet, respectively. The actual bipolar injection process occurs in two circular regions with radius $h = 5$ kpc aligned with the BH. A slice through a mesh with the injection regions (1,2) is shown in Figure 3.4 with the bigger enclosing circle marking the buffer region (3). The buffer region is used for the redistribution of mass and thermal energy from the two injection regions, also referred to as jet regions. The black dot in the center marks the BH particle. The two jets are launched in vertical direction away from the BH. The jet direction is referred to as $\hat{\boldsymbol{n}}$ throughout the paper.

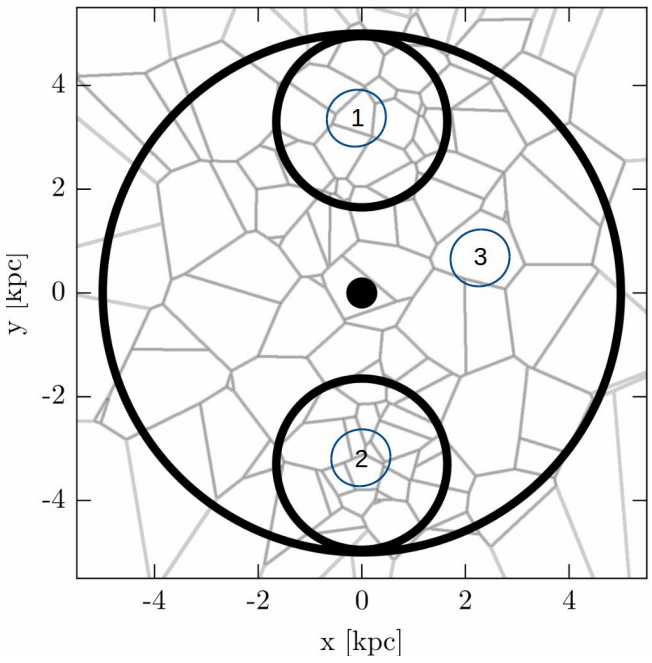

Figure 3.4: The two small circles (1,2) mark the injection (jet) region (with radius $0.33h$) of the jet, which is launched in the direction opposite to the BH (black dot) in the center. The enclosing circle (3) marks the buffer region (with radius h), which is used for redistributing mass and thermal energy to setup up the jets (adopted from Figure 1 of Weinberger et al. 2017).

To set up the jet the density in the jet regions, we set $\rho_{1,2}$ to the desired $\rho_{\rm target}$ constant value

as

$$\rho_{1,2} = \rho_{\text{target}} \frac{V_1 + V_2}{2V_{1,2}}. \tag{3.13}$$

The volume factor is necessary to ensure the same amount of mass in 1 and 2 as generally $V_1 \neq V_2$. The specific thermal energy $u_{1,2}$ in both regions is determined employing the following formula

$$u_{1,2} = \frac{P_{\text{target}}}{(1 + x_{\text{cr,jet}} + x_{B,\text{jet}})(\gamma - 1)\rho_{1,2}}, \tag{3.14}$$

with the adiabatic index of the gas $\gamma = 5/3$ and the kernel-weighted pressure of the gas in the buffer region. A SPH-smoothing kernel $w(r, h)$ of the following type has been employed

$$w(r,h) = \frac{8}{\pi h^3} \begin{cases} 1 - 6\left(\frac{r}{h}\right)^2 + 6\left(\frac{r}{h}\right)^3, & 0 < \frac{r}{h} < \frac{1}{2} \\ 2\left(1 - \frac{r}{h}\right)^3, & \frac{1}{2} < \frac{r}{h} \leq 1 \\ 0, & \frac{r}{h} > 1 \end{cases} \tag{3.15}$$

where r is the distance to the BH. The CR specific energy can then readily be calculated as

$$u_{\text{cr},1,2} = \frac{P_{\text{target}}}{(1 + x_{\text{cr,jet}}^{-1} + x_{\text{cr,jet}}^{-1} x_{B,\text{jet}})(\gamma_{\text{cr}} - 1)\rho_{1,2}} \tag{3.16}$$

where $\gamma_{\text{cr}} = 4/3$ is the adiabatic index of the CRs. As a certain density in the jet regions is specified, mass has to be removed from (added to) the jet regions and added to (removed from) the buffer region adiabatically in a mass-weighted fashion. The attributed change in momentum is compensated for in the buffer region. In addition, the total thermal energy change in the jet region is compensated for as this energy is added to (removed from) the buffer region using $w(r, h)$. The overall change in energy due to the various described redistribution steps ΔE_{redist} can be expressed as

$$\begin{aligned} \Delta E_{\text{redist}} = \sum_{\text{regions } 1,2,3} \Big[& \frac{m_{i,\text{final}}}{2} v_{i,\text{final}}^2 - \frac{m_{i,\text{init}}}{2} v_{i,\text{init}}^2 + \\ & (u_{i,\text{final}} + u_{\text{cr},i,\text{final}}) m_{i,\text{final}} - (u_{i,\text{init}} + u_{\text{cr},i,\text{init}}) m_{i,\text{init}} \Big] \end{aligned} \tag{3.17}$$

with the sum extending over all regions $1, 2, 3$ and considering the masses m, velocities v and thermal energies of gas u and CRs u_{cr} of cell i at the beginning (*init*) and at the end (*final*) of the redistribution process.

A purely toroidal magnetic field is injected in the direction

$$\hat{\boldsymbol{B}}_i = \frac{\boldsymbol{r}_i \times \hat{\boldsymbol{n}}}{|\boldsymbol{r}_i \times \hat{\boldsymbol{n}}|}, \tag{3.18}$$

where the vector $\boldsymbol{r}_i$ points from cell i into the direction of the BH. The injected magnetic field is parametrized in the following way:

$$\Delta \boldsymbol{B}_i = w_{\boldsymbol{B},i} f_{\boldsymbol{B}} \hat{\boldsymbol{B}}_i. \tag{3.19}$$

Here, the factor $f_{\boldsymbol{B}}$ denotes the scaling factor to acquire the desired average $x_{B,\text{jet}}$. It is determined by solving the following equation of the total change in magnetic field energy

$$\Delta E_B = \sum_i (\boldsymbol{B}_{i,\text{init}} + \Delta \boldsymbol{B}_i)^2 V_i (8\pi)^{-1} - \sum_i \boldsymbol{B}_{i,\text{init}}^2 V_i (8\pi)^{-1}, \tag{3.20}$$

where $\boldsymbol{B}_{i,\mathrm{init}}$ is the magnetic field before injection. The kernel $w(r, h)$ is used to derive the weights of the magnetic field $w_{\boldsymbol{B},i}$ in each cell i according to

$$w_{\boldsymbol{B}} = w(s_i, 0.33\ h) \left(\frac{\boldsymbol{s}_i^2 - (\boldsymbol{s}_i \cdot \hat{\boldsymbol{n}})^2}{(0.33\ h)^2} \right)^4, \tag{3.21}$$

with the vector $\boldsymbol{s}_i$ pointing from the center of the respective jet region to cell i and $0.33\ h$ corresponds to the radius of the individual jet regions.

Finally, the kinetic energy is injected where the exact value is derived from Equation 3.12. The momentum is injected following

$$\Delta \boldsymbol{p}_i = w(s_i, 0.33\ h)\ m_i\ f_{\boldsymbol{p}}\ \frac{\hat{\boldsymbol{n}} \cdot \boldsymbol{r}_i}{|\hat{\boldsymbol{n}} \cdot \boldsymbol{r}_i|}, \tag{3.22}$$

where the factor $f_{\boldsymbol{p}}$ can be calculated from the total available kinetic energy ΔE_{kin} by analogy with the procedure for the magnetic field. Here, the formula describing ΔE_{kin} is given by

$$\Delta E_{\mathrm{kin}} = \sum_i \frac{(\boldsymbol{p}_{i,\mathrm{ini}}^2 + \Delta \boldsymbol{p}_i)^2}{2m_i} - \frac{\boldsymbol{p}_{i,\mathrm{old}}^2}{2m_i}. \tag{3.23}$$

In addition to the desired amount of CRs and magnetic fields, we inject a passive scalar. During each injection event, the mass fraction of the jet material x_{jet} is set to one. The mass fraction is only advected with the flow.

To optimize computation and focus on relevant lobe physics, three different refinement criteria are used. Normally, the refinement criteria is based on maintaining the mass of each cell. The cell is refined/derefined if the mass in this cell exceeds/drops below a certain specified target mass $m_{\mathrm{target},0}$ (Vogelsberger et al. 2012). This mass-based refinement criteria is employed to keep the computations in the outskirts of the cluster to a minimum.

As we focus our attention to the center for the lobes, we additionally use a crucial volume-based refinement criterion. The lobes are about three orders of magnitude more dilute than the surrounding medium in the center of the cluster such that the mass-based refinement would immediately create very large cells resulting in poorly resolved lobe dynamics. Summarizing the two mentioned criteria an effective target mass $m_{\mathrm{target},i}$ is calculated in each cell

$$m_{\mathrm{target},i} = f \rho_i V_{\mathrm{target}} + (1 - f) m_{\mathrm{target},0}, \tag{3.24}$$

which is used for refinement with

$$f = 0.5 + 0.5 \tanh \left(\frac{x_{\mathrm{tracer},i} - 10^{-4}}{10^{-5}} \right). \tag{3.25}$$

This has proven to achieve uniform spatial resolution of the jet and lobe structure. Due to the low diffusivity of AREPO, the exterior regions are not significantly affected by the refinement criteria (Weinberger et al. 2017). In contrast, the boundary layer between under-dense lobe and surrounding is very relevant. To capture interface effects in more detail, a third refinement criterion is employed which is based on the steepness of the density gradient $|\nabla \rho|$. This form of refinement is utilized and then replaces the previously mentioned criteria in cell i if

$$V_i^{1/3} |\nabla \rho_i| > 0.5 \rho_i. \tag{3.26}$$

To prevent runaway refinement, the volume of every cell is restricted to a certain minimum volume V_{min} which is in general set to $V_{\mathrm{min}} = V_{\mathrm{target}}/2$. To impede very large differences in

resolution between neighbouring cells, refinement is applied when adjacent cells have volumes deviating by a factor of three or larger. To follow the flow more accurately, heavily distorted cells are refined more easily (Weinberger et al. 2017).

We allow CRs to anisotropically diffuse out of the bubbles following magnetic field lines. Jets are assumed to posses a magnetic field that is isolated from the magnetic field of the cluster. To replicate this scenario, special care is taken of the magnetic isolation of the injection zone. Otherwise, CRs would be able to immediately diffuse out of the bubbles. In practice, this is enforced through application of the same projection operator employed at the interface of the magnetic fields on different meshes when setting up the magnetic field. Analogously, the operation given in Equation 3.7 is now employed on the fly in AREPO. In contrast, the width of the interface layer $\Delta x = 0.165$ is set to a less intervening value. The whole circular injection zone is also only considered initially. Later this would impede the structure of the magnetic field in the direction of the moving jet. Consequently, to only include cells in a cone at the back of the injection region, we require for isolation

$$r_i^2 < 0.8(0.67\ h)^2, \tag{3.27}$$

where r_i is the distance of cell i to the BH, which seems to work in practice. The routine is applied every timestep during which the jet is injecting. Thus, the jet region is magnetically isolated at the beginning of every individual injection process. The removed magnetic field strength is later added with the respective kernel to the injected magnetic field during the respective injection event.

3.3 Cluster properties

To study the evolution of the lobes and CRs generated by the jet module, we set up an idealized cluster. The turbulent magnetic field is set up in an otherwise ordinary NFW potential (Equation 2.1) in static equilibrium. The turbulent nature of the magnetic field will however initiate motions in the thermal gas. The free parameters of the NFW profile have been chosen to model the Perseus cluster, one of the best studied CCs. The mass within $r_{200} = 2.12$ Mpc is chosen to be $M_{200} = 10^{15} M_\odot$ with concentration parameter $c = 5$. The analytical potential sets the gravitational force on each cell.

The gas component of the cluster set up is based on a double-beta profile (Equation 2.17) fit to the electron number density by Churazov et al. (2003). In addition, a gas fraction of 16% within r_{200} is assumed to scale the number electron number density n to

$$n = 26.9\times10^{-3}\left(1+\left(\frac{r}{57\ \mathrm{kpc}}\right)^2\right)^{-1.8}\mathrm{cm}^{-3} + 2.8\times10^{-3}\left(1+\left(\frac{r}{200\ \mathrm{kpc}}\right)^2\right)^{-0.87}\mathrm{cm}^{-3}. \tag{3.28}$$

The pressure of each individual cell is obtained from the condition of hydrostatic equilibrium and the constraint that the pressure vanishes at a radius of 3 Mpc. Here, also the pressure contributions from the magnetic field fluctuations are corrected for by applying the opposite perturbations to temperature.

3.4 Configuration and parameters

Jet and magnetic field parameters that were left unchanged for the analysis are summarized in Table 3.1 as well as the parameters that concern the resolution. An overview of the suite of simulations analyzed is given in Table 3.2.

Jet parameters		
Jet density	ρ_{target}	10^{-28} g cm^{-3}
Black hole region	h	5 kpc
CR fraction	$x_{\text{cr,jet}}$	1.0
Magnetic field parameters		
Injection scale	k_{inj}	37.5^{-1} kpc^{-1}
Resolution		
Target mass	$m_{\text{target,0}}$	low res: 1.5×10^7 M$_\odot$ fid. res: 1.5×10^6 M$_\odot$
Target volume	$V_{\text{target}}^{1/3}$	low res: 872 pc fid. res: 405 pc
Minimum volume	V_{min}	$V_{\text{target}}/2$

Table 3.1: A summary of the fixed parameters of the simulation and the two different resolution setups.

Name	P_{jet} [erg s^{-1}]	$x_{B,\text{ext}}$	$x_{B,\text{jet}}$	t_{jet} [Myr]	κ [cm^2 s^{-1}]	Turb.
fid (MY1)	3×10^{44}	0.05	0.1	10	1×10^{29}	Yes
X5M0	3×10^{44}	0.05	0	10	1×10^{29}	Yes
X5M10	3×10^{44}	0.05	1	10	1×10^{29}	Yes
X1M1	3×10^{44}	0.01	0.1	10	1×10^{29}	Yes
NX0M0	3×10^{44}	0	0	10	0	Yes
NX0M1	3×10^{44}	0	0.1	10	0	Yes
NX0M0P	3×10^{44}	0	0	10	0	No
NX0M1P	3×10^{44}	0	0.1	10	0	No
E743X5M1	7×10^{43}	0.05	0.1	10	1×10^{29}	Yes
E44X5M1	1×10^{44}	0.05	0.1	10	1×10^{29}	Yes
E45X5M1	1×10^{45}	0.05	0.1	10	1×10^{29}	Yes
X5M1MY2	3×10^{44}	0.05	0.1	20	1×10^{29}	Yes
X5M1MY5	3×10^{44}	0.05	0.1	20	1×10^{29}	Yes

Table 3.2: Jet parameters of the different models with jet power P_{jet}, external magnetic pressure $x_{B,\text{ext}}$, jet magnetic fraction $x_{B,\text{jet}}$, time of activity of the jet t_{jet}, CR diffusion coefficient κ and whether the ICM is turbulent.

The lobes always contain a population of CR protons in our simulations. Their assumed pressure fraction $x_{\text{cr,jet}}$ can be justified as follows. As discussed in Section 2.1.3, the lobes of FRI sources need an additional pressure component in addition to radiating leptons. Initially entrained protons by the jet seem to be a likely candidate. These protons could then, by analog with the electrons, be accelerated in the jet and create a relativistic population of protons in the lobes (Pfrommer 2013). The observed diffuse radio emission of radio mini halos in CCs is also in agreement with such a hadronic model as discussed in Section 2.2.1. The higher detection rate for warmer CCs cluster with presumably on-going feedback processes supports this theory (Jacob and Pfrommer 2017b).

The injected CR pressure fraction $x_{\rm cr,jet} = P_{\rm cr,jet}/P_{\rm th,jet}$ in our simulations is up to two orders of magnitude lower than observed values (Croston 2008). This is due to numerical issues that arise with the current implementation. However, the dynamical effect, which is mostly relevant in the following discussion, is assumed to be sub-dominant.

We create one turbulent realization of the magnetic field and scale the amplitude of $\boldsymbol{B}$. To mimic the effect of turbulence in the ICM without intra-cluster MHD effects, we also model thermal pressure fluctuations with amplitudes equal to our MHD perturbations, i.e. $x_{\rm turb} = \rho v^2/P_{\rm th} \sim 0.05$.

In the following not all simulations will be discussed in detail but the for the section relevant insights from varying parameters will be discussed.

4 Analysis

In this section, an overview of the general evolution of the rising bubble is given (Section 4.1). The magnetic field in the wake of the bubble is amplified in the simulation and the bubble is stabilized by the magnetic field that is draped around the bubble interface. Both effects are discussed in Section 4.2. Finally, we analyze the dynamics and distribution of the injected CRs in Section 4.3.

4.1 Characteristic evolution of rising bubble

4.1.1 General evolution

The identified phases of bubble evolution are largely independent of resolution (m_{target} ,V_{target}) and other free parameters of the models with regard to the CRs (κ_{cr}, x_{cr}), external magnetic field ($x_{B,\text{ext}}$) and the jet itself (P_{jet}, t_{jet}, $x_{B,\text{jet}}$).

The evolution of the fiducial run can be seen in Figure 4.1. The figure shows the density ρ, the velocity in units of the sound speed v/c_{s}, the tension to total force ratio $x_{B_{\text{tens}}}$, the kinetic-to-thermal pressure ratio $x_{\text{kin}} = P_{\text{kin}}/P_{\text{th}}$, the magnetic-to-thermal pressure ratio $x_B = P_{\text{B}}/P_{\text{th}}$ and the CR-to-thermal pressure ratio $x_{\text{cr}} = P_{\text{cr}}/P_{\text{th}}$. The tension force is derived from the Lorentz force density in the momentum equation, which reads $ne/c\ (\boldsymbol{v} \times \boldsymbol{B}) = 1/c\ (\boldsymbol{J} \times \boldsymbol{B}) = 1/(4\pi)\ \left[(\boldsymbol{B} \cdot \nabla)\, \boldsymbol{B} - \nabla\left(1/2\ \boldsymbol{B}^2\right)\right]$ where n is the number density of charges and $\boldsymbol{J} = ne\boldsymbol{v} = c/(4\pi)\ (\nabla \times \boldsymbol{B})$ is the current density. The first term describes the tension force and the second the magnetic pressure force. Here, the absolute value of the specific tension force is defined as $F_{B_{\text{tens}}} = |(\boldsymbol{B} \cdot \nabla)\, \boldsymbol{B}|\,/(4\pi\rho)$. The value of $x_{B_{\text{tens}}}$ is then computed as the ratio between $F_{B_{\text{tens}}}$ and the other forces acting on the system including the thermal, magnetic and CR specific pressure forces and the specific gravitational force.

The jet is injected and accelerated in the center of the cluster. A quasi-isotropic subsonic shock wave is observed, which is initiated by the jet. Secondly, the lobe is inflated by jet material that is deflected at the contact discontinuity between the jet and the shock. After the jet ceases to power the lobes, the lobes decouple from the BH. Bubbles rise buoyantly in the atmosphere of the cluster. Dense and cool cluster material streams down to the center of the cluster and fills the low-density wake of the bubble. The bubble drags magnetic field lines, which are amplified. Finally, the bubble fragments due to vorticity that is generated in the wake. The under-dense, high-entropy gas moves upward until isentropy is established. A more detailed description follows:

(i) **Propagating shock wave:** The evolution of the jet and lobes has been studied in previous simulations (Lind et al. 1989; Reynolds et al. 2002) with very similar results. Throughout the injection phase a shock is driven by the accelerated material. In the fiducial model, the jet can be identified at 10 Myr in Figure 4.1 as a kinetically dominated, supersonic ($v/c_{\text{s}} \approx 1$) outflow.

The jet material drives a large, initially elliptical shock into the ambient medium. The backflow of the ICM fills in the under-pressured wake. In addition, the lobe is inflated by material that is deflected at the contact discontinuity between the jet and the shock.

The extend of the working surface of the shock causes the initial momentum of the jet to be distributed on a larger area. Thereby, lower speeds can be reached if instead the jet would drill into the ambient medium. The backflow gradually slows down and forms an extended lobe around the jet. The width of this expansion appears limited by the magnetic tension force such that a highly oblique bow shock develops.

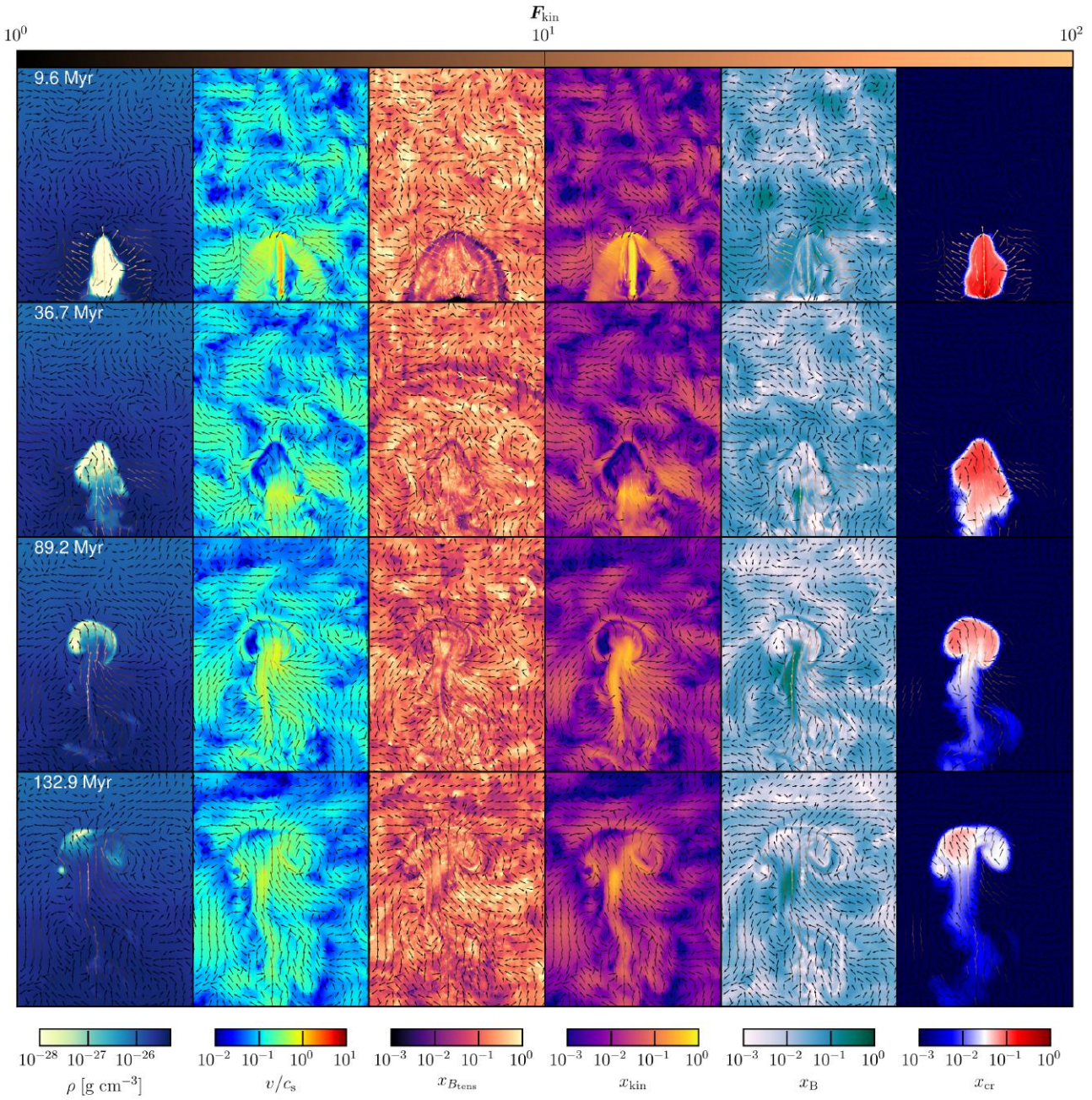

Figure 4.1: The density ρ, velocity in units of sound speed v/c_s, tension to total force ratio $x_{B_{\rm tens}}$, kinetic-to-thermal pressure ratio $x_{\rm kin}$, magnetic-to-thermal pressure ratio x_B and CR-to-thermal pressure ratio $x_{\rm cr}$ are portrayed of the fiducial run. The images correspond to thin 80 kpc $-$ 60 kpc $-$ 2 kpc projections weighted with the jet tracer mass fraction to highlight the features of the jet centered at $(40, 0, 0)$. The arrows show the kinetic energy flux $\boldsymbol{F}_{\rm kin}$ where arrow length and color are scaled logarithmically with respect to the absolute value $|\boldsymbol{F}_{\rm kin}|_{x,z}$ in the $x-z$ plane that is shown. The color scales are fixed for different times shown, respectively.

After the jet is switched off at 10 Myr, the kinetic energy fraction $x_{\rm kin}$ drops significantly within the lobe. Consequently, the working surface disappears and the previously strong backflow ceases. The jet's head slows down to subsonic speeds.

The kinetic energy is converted to thermal energy. However, this happens on time scales that are not resolved by the simulation. It can be deduced from the energy contributions of the lobes, which are the magnetic field energy, the CR energy, the kinetic energy and the thermal energy. Figure 4.2 shows that from 10 Myr the majority of the kinetic energy is converted into thermal energy. The accelerated shock front is faster than the bubble and escapes into the ambient medium. The figure shows a stationary total energy density $\epsilon_{\rm tot}$. The kinetic energy contribution $\epsilon_{\rm kin}/\epsilon_{\rm tot}$ decreases at the expanse of an increasing thermal energy contribution $\epsilon_u/\epsilon_{\rm tot}$. The CR $\epsilon_{\rm cr}/\epsilon_{\rm tot}$ and magnetic energy $\epsilon_B/\epsilon_{\rm tot}$ contribution stay approximately constant. The CRs are concentrated in the lower part. The magnetic field is energetically subdominant in the bulk of the ICM and is enhanced at the rim of the bubbles.

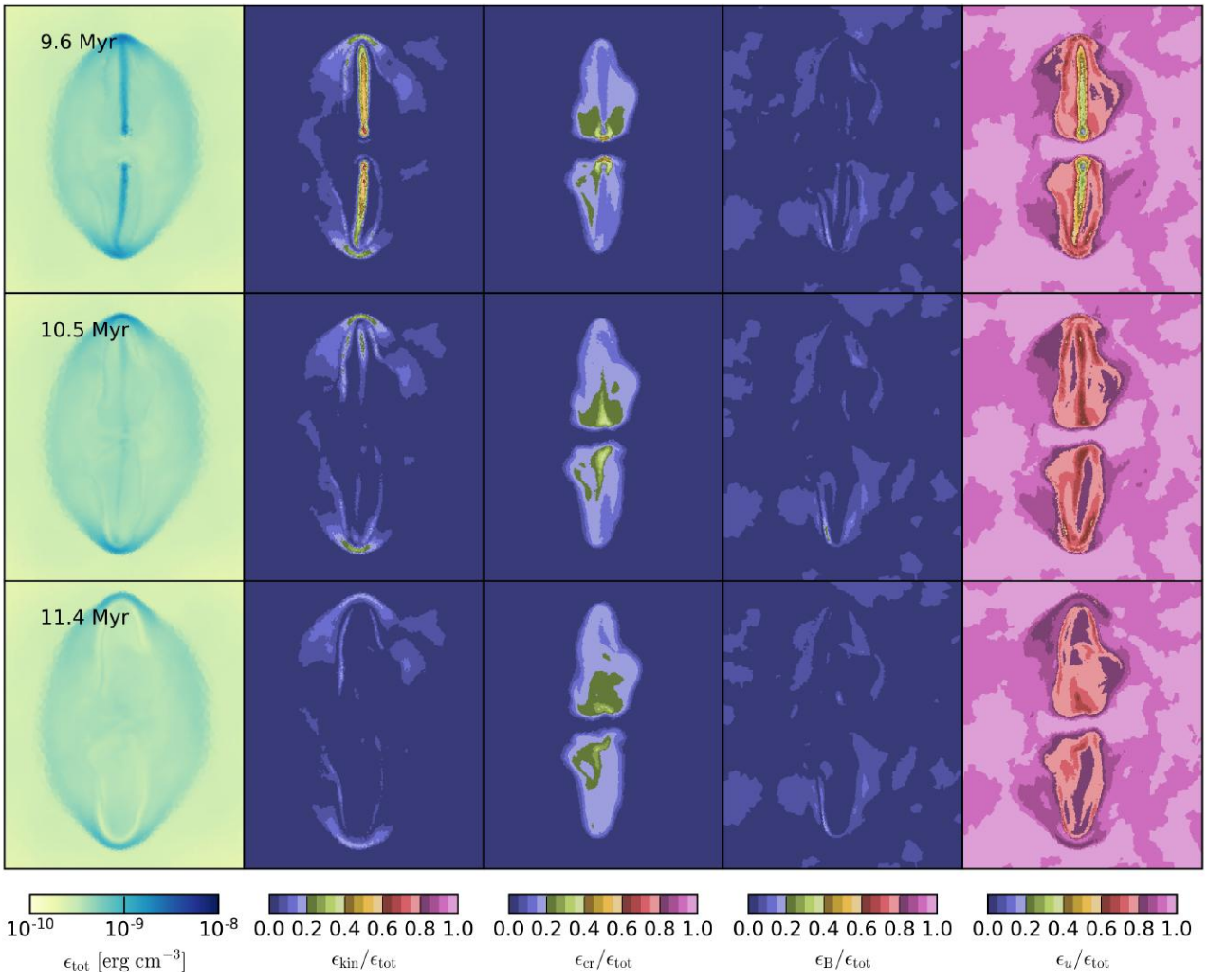

Figure 4.2: The kinetic $\epsilon_{\rm kin}$, CR $\epsilon_{\rm cr}$, thermal ϵ_u and magnetic ϵ_B energy density, which are normalized to the total energy density $\epsilon_{\rm tot} = \epsilon_{\rm kin} + \epsilon_{\rm cr} + \epsilon_u + \epsilon_B$, are shown just after injection. The projections have dimensions 60 kpc $-$ 50 kpc $-$ 2 kpc and are weighted with the jet mass $x_{{\rm jet},i}\ m_i$.

(ii) **Rising bubble:** After jet activity ceases, the system represents a configuration of a high entropy concentration in the center of a stratified gravitational potential. According to

the Schwarzschild condition for buoyancy instability $\mathrm{d}S/\mathrm{d}r < 0$, the system is highly unstable. The bubble rises until $S_{\mathrm{int}} = S_{\mathrm{ext}}$. The former bubble becomes part of the cluster atmosphere.

As evident from Figure 4.1, the bubble leaves a low-density cavity in its wake. Instreaming gas is accelerated into this region. As it passes the lobe, it induces a high degree of vorticity, especially in the lower half of the bubble. As a result, the bubble gets magnetically connected to the wake region, thereby enabling CRs to diffuse out. Purely hydrodynamical jets propagating into an unmagnetized ICM are quickly disrupted by the overshooting gas that impinges on the lower envelope of the bubbles (see Figure A.1). The bubble is prone to powerful Rayleigh-Taylor and Kelvin-Helmholtz instabilities, which disrupt the lobe on a short time-scale. Our results reproduce well-known findings in the literature (e.g., Reynolds et al. 2005; Ruszkowski et al. 2007). The longevity of bubbles in X-ray and radio observations excludes this purely hydrodynamical model; thus, we will not discuss this model any further in the following.

On the other hand in a magnetized cluster atmosphere, i.e., $x_{B,\mathrm{ext}} \neq 0$, the external magnetic field provides a strong tension force that is able to stabilize the lobe against the up-flowing gas. This becomes evident from the tension-to-total force ratio that shows values on the order of unity along the rim of the bubble. The force ratio includes contributions from gravity as well as thermal, magnetic and CR pressure forces. Although the initial magnetic field with $x_B = 0.05$ is energetically negligible the magnetic tension force is still relevant because of strongly bend field lines. The other forces balance each other. In addition, the magnetic tension is enhanced at the rim of the bubble via draping of magnetic fields.

In contrast, Figure 4.3 shows run NX0M1P in a quiet, unmagnetized cluster with only CR advection. The bubble shows higher degrees of fragmentation. This can be determined from the CR fraction as diffusion is not active. Thus, fragmentation represents the only mechanism for CRs to leave the bubble. By analogy with the fiducial run, we see a high level of vorticity in the bubble. The spherical bubble transforms into a torus-like structure due to the upwards accelerating backflow. The torus is maintained due to the circulation flow resulting from vorticity conservation. The magnetic tension is not able to provide sufficient stability. This difference in stability can be explained with the lack of an external magnetic field, which would otherwise provide the crucial stabilizing effect in terms of magnetic draping (see Section 4.2.1).

The shearing motion of the upwards moving bubble represents conditions for the development of Kelvin-Helmholtz (KH) instabilities. These are expected to be significantly suppressed by the surface tension that is provided by magnetic fields. Earlier simulations (Churazov et al. 2001; Reynolds et al. 2002) without magnetic fields show the bubble to be disrupted by a combination of KH and Rayleigh-Taylor (RT) instabilities. However, simulations with magnetic fields or viscosity significantly increase the disruption timescale (Reynolds et al. 2005; Guo 2015). In addition to the inclusion of magnetic fields, our simulations are able to resolve a high density contrast. Artificial mixing between interface cells through numerical diffusion is significantly suppressed. This is due to more aggressive refinement criteria compared to previous simulations.

The explicit timescales for both the KH and the RT instability, τ_{KH} and τ_{RT}, are given

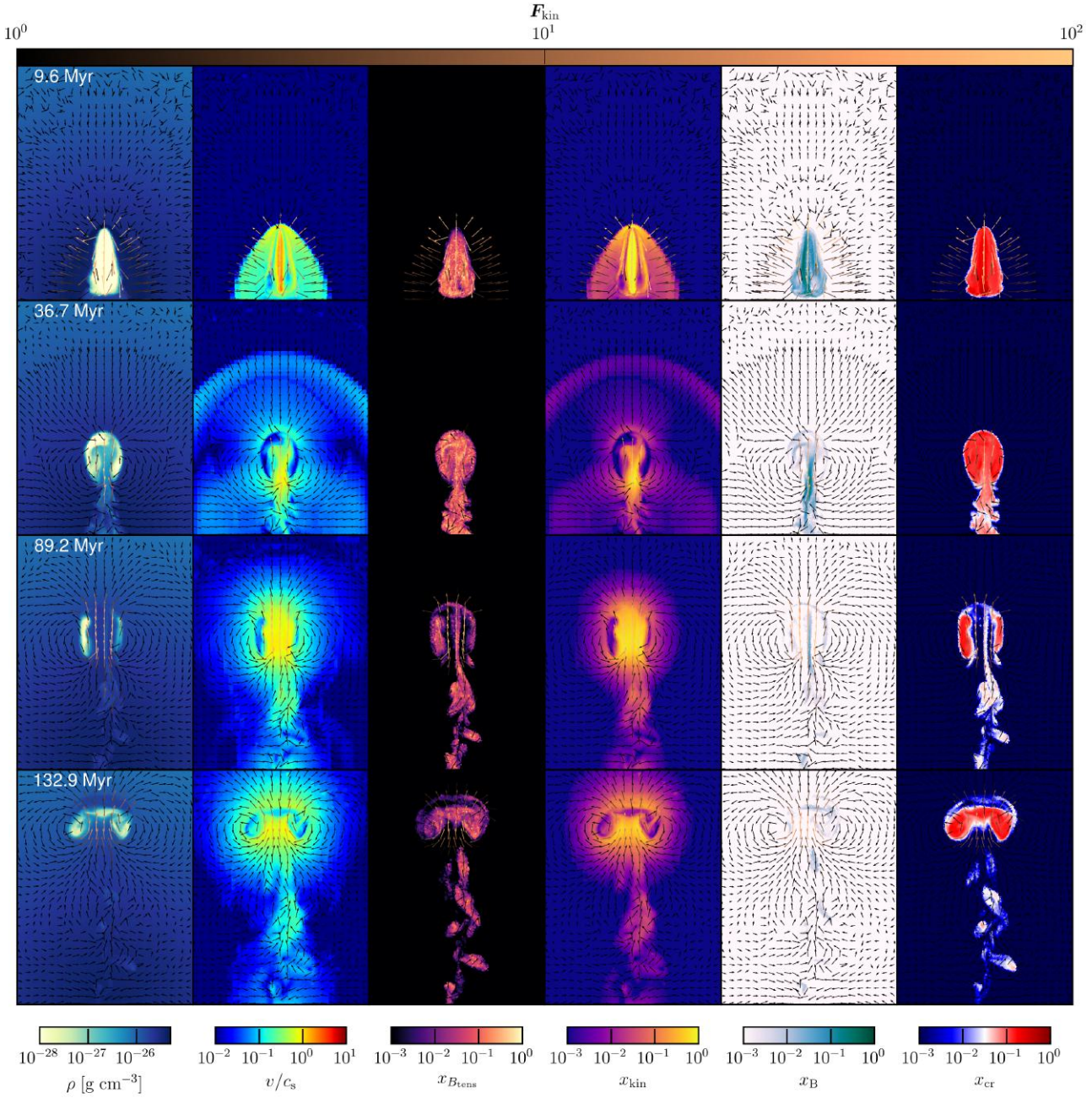

Figure 4.3: Same as in Figure 4.1 but now run NX0M1P is shown, i.e. $x_{B,\rm jet} = 0.1$ and a quiet, unmagnetized cluster.

by (Chandrasekhar 1981):

$$\begin{aligned} \tau_{\rm KH} &= \frac{\rho_1 + \rho_2}{(\rho_1\rho_2)^{0.5}} \frac{1}{\Delta v k} \approx \left(\frac{\rho_2}{\rho_1}\right)^{0.5} \\ \tau_{\rm RT} &= \left| \frac{\rho_1 + \rho_2}{\rho_1 - \rho_2} \frac{1}{\dot{v} k} \right| \approx \frac{1}{|\dot{v} k|^{0.5}}, \end{aligned} \tag{4.1}$$

where ρ_1 is the density of the lobe, ρ_2 is the density of surrounding medium, Δv is the relative velocity of the shear flow at interface, $\dot{v}$ is the acceleration of the lobe and k is the wavenumber of the perturbation. Typical values for our simulations ($\Delta v \approx 500$ km s^{-1},

$\rho_1/\rho_2 \approx 10^{-3}$) yield the following timescales

$$\begin{aligned} \tau_{\mathrm{KH}} &\approx 600\ (k\ 10\mathrm{kpc})^{-1}\ \mathrm{Myr} \\ \tau_{\mathrm{RT}} &\approx 30\ (k\ 10\mathrm{kpc})^{-0.5}\ \mathrm{Myr} \end{aligned} \tag{4.2}$$

Consequently, KH instabilities are not expected to arise on scales $\lambda < 10$ kpc.

Figure 4.4 shows the early lobe evolution of runs with different magnetic field parameters. Thin projections of the jet tracer mass fraction x_{jet} are portrayed. Developing KH instabilities can be seen in run NX0M1 and NX0M1P and possibly in run X1M1. The magnetization of the lobe does not seem relevant, probably due to the low magnetic field strength there (e.g., see Figure 4.11). The strength of the magnetic field in the fiducial run is sufficient to suppress KH instabilities. In contrast, the lower external magnetic field strength in run X1M1 does not completely suppress them.

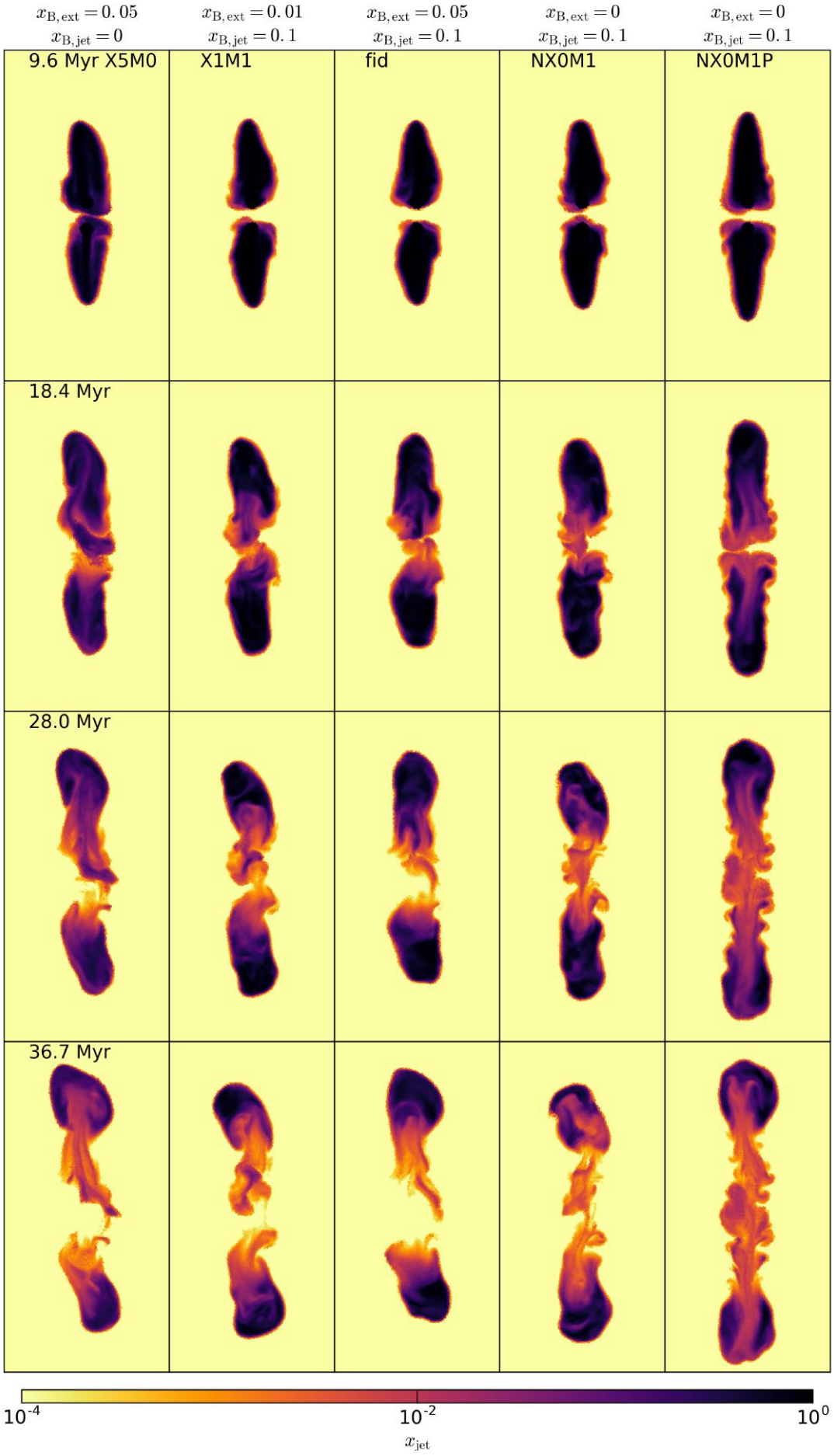

Figure 4.4: Projections of the jet tracer mass fraction x_{jet} are shown for runs with different degrees of magnetization in the lobes ('M') and the cluster ('X'). The projections have dimensions 80 kpc − 40 kpc − 4 kpc and are weighted with the jet mass $x_{\mathrm{jet},i}\, m_i$.

(iii) **Disruption of the bubble:** Figure 4.5 shows the long-term evolution of a bubble in the fiducial run. The symmetry of the bubble is quickly disturbed, which impedes the analysis. Consequently, the projections show the simulation rotated by $\pi/4$ from left to right. At later times (> 100 Myr), the curved bubble surface stretches out and becomes more elongated. This is mainly due to the effect of gravity, which points towards the center of the cluster. To stay in local hydrostatic equilibrium, the bubble aligns with the equipotential surface.

At some point the surface tension of the bubble is not able to confine the bubble any longer. The bubble breaks into two and both bubbles continue to rise. The inflowing gas still causes the inner part of the bubble to mix heavily with the cluster material and stir turbulence within the bubble. All runs show the creation of vorticity in the wake of the bubble and to varying degrees inside the bubble. This crucial feature is identified as a general characteristic of a RT instability. It is explored in the following with regard to mixing and disruption of the bubble.

a) **Mixing** The prevalence of mixing can be seen when looking at the evolution of the jet tracer x_{jet} in Figure 4.5. The fraction decreases significantly over time. The vorticity-dominated center of the bubble becomes completely diluted over time. Only the outer shell of the bubble stays confined. Figure 4.6 shows the evolution of the cumulative volume fraction up to a certain density ρ. Only cells within the bubble are considered here, which is defined as cells with a tracer value of $x_{\text{jet}} > 10^{-3}$.

If mostly cells with $x_{\text{jet}} \sim 10^{-3}$ make up the lobe, then by definition, the lobe will contain a lot of mass from the exterior material. This causes the lobe material density to increase. Initially, around $40-50\%$ of the volume of the lobe is filled with low-density gas ($\rho_{\text{jet}} = 1 \times 10^{-28}$ gcm^{-3}) in all runs.

The material becomes denser over time with significant difference between setups. Jets without any injected magnetic field in their lobes ('M0', $x_{\mathbf{B},\text{jet}} = 0$) generally show more rapid mixing. Magnetic fields make the fluid more viscous through their pressure and tension forces, irrespective of their exact strengths. The runs in a quiet atmosphere ('P') show significant initial mixing. However, on longer timescales these bubbles reach a stable state that impedes mixing. The absence of external disruption limits the degree of mixing, which is in agreement with Bourne and Sijacki (2017).

As discussed in the previous section, the strength of the external magnetic field sets the degree of KH instabilities. Figure 4.8 shows the full projection of the jet tracer. Early fragmentation is visible in all runs. Partly, this can be explained with KH instabilities. However, a clear correlation between mixing and external magnetic field strength cannot explain the result. In addition, the degree of magnetization of the lobes appears crucial, where magnetized lobes provide more stability.

The discussed trend can also be seen in Figure 4.7. Here, the cumulative volume fraction of gas with higher jet mass fractions is depicted as a function of the jet mass fraction. The run with magnetized lobes is able to retain larger volume fractions with high jet mass fractions early on. Magnetic fields keep the gas confined. Projections of the vorticity in Figure 4.9 support this idea. The vorticity of runs X1M1 and fid appear to originate from the wake of bubble fragments. On the other hand, in run NX0M1 more tracks can be identified. The setup of a quiet atmosphere (especially with magnetized lobes) retains a high jet fraction on large timescales. Run NX0M1 shows slightly higher levels of mixing. The bubbles appear to fragment more often. However, due to the magnetized lobes, the newly formed bubbles still retain their

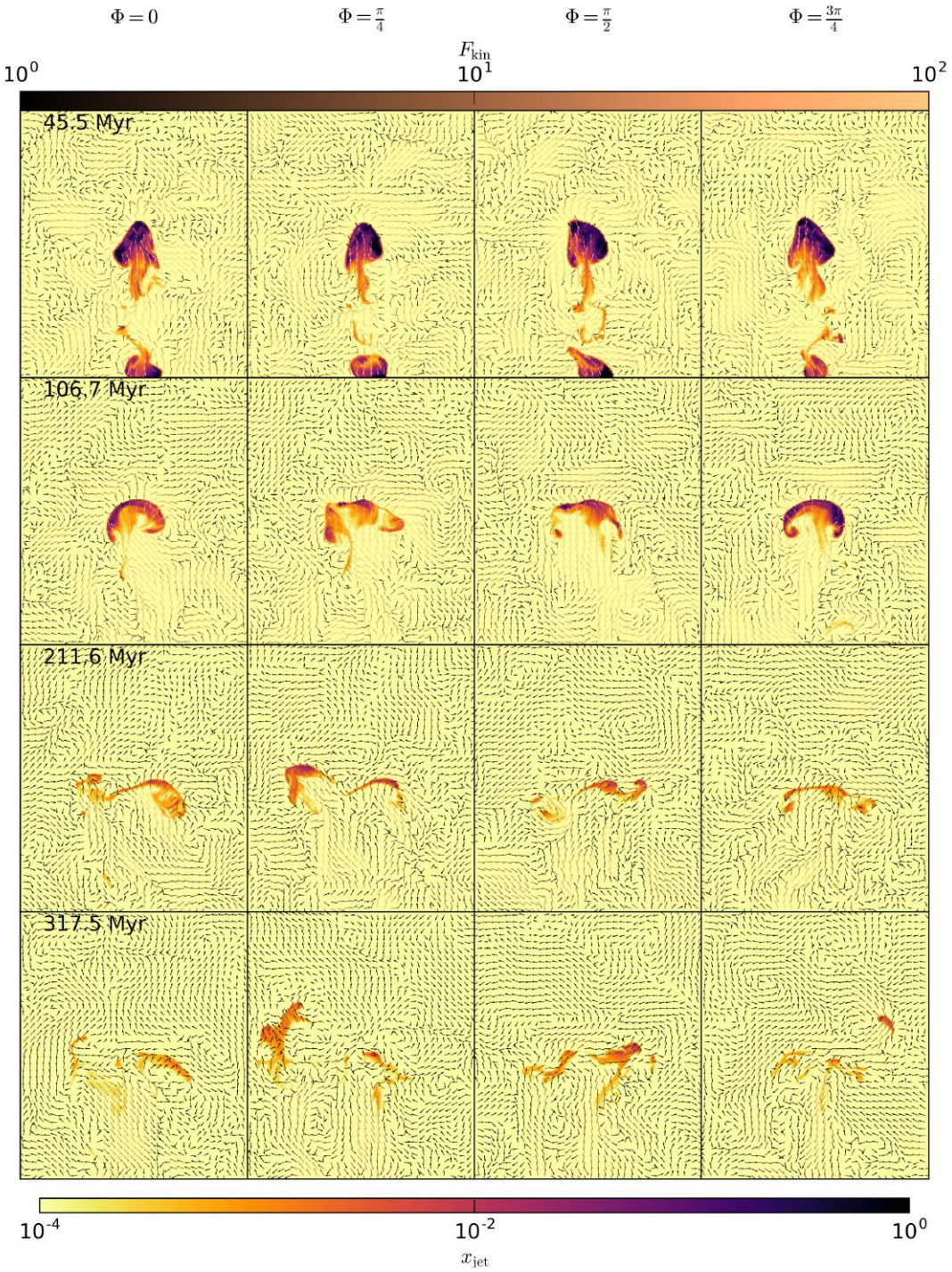

Figure 4.5: The jet tracer mass fraction x_{jet} of the fiducial run is shown with a quiver plot of the kinetic energy flux F_{kin}. The simulation is rotated by $\pi/4$ along the vertical axis from left to right. Thin projections, which are weighted with the jet mass $x_{\mathrm{jet},i}\ m_i$, with 100 kpc $-$ 85 kpc $-$ 4 kpc for both the arrows and the background image are depicted.

jet mass fraction. This explains the observed trend in Figure 4.7 with higher volume fractions for runs with magnetized lobes as well as magnetized atmospheres, where the former effect dominates.

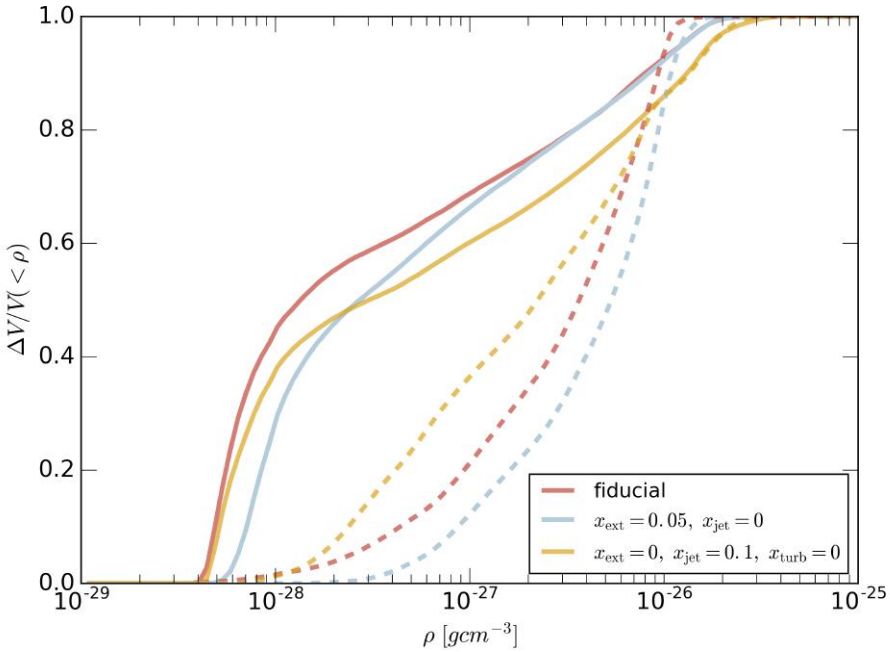

Figure 4.6: The volume fraction up to a certain density ρ as a function of density for different simulations within the bubble ($x_{\rm jet} > 10^{-3}$) at times 9 Myr (line) and 107 Myr (dashed).

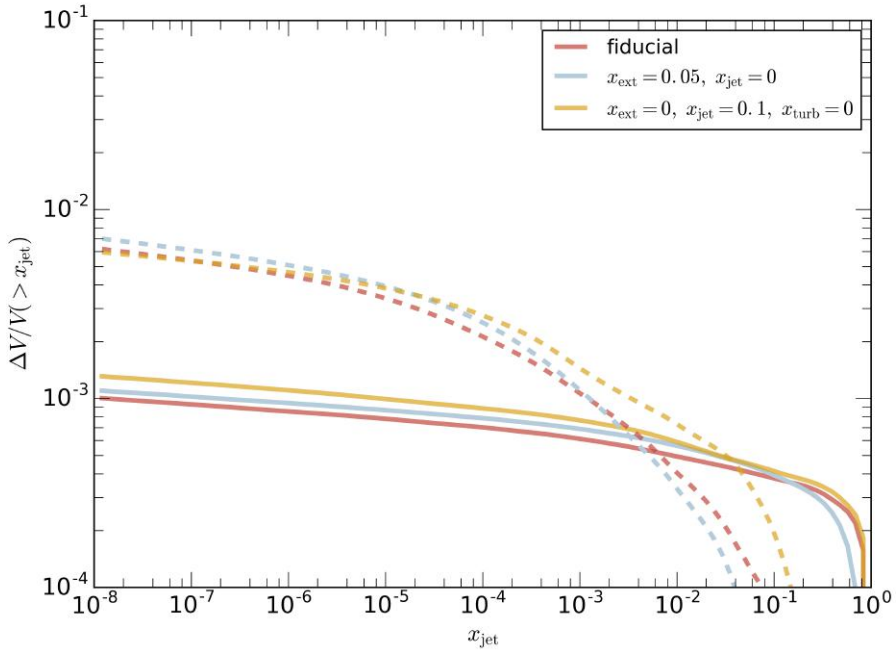

Figure 4.7: The volume fraction $\Delta V/V(< x_{\rm jet})$ of gas below a certain jet tracer fraction as a function of the jet tracer density $x_{\rm jet}$ for different simulations within 100 kpc of the cluster center at times 9 Myr (line) and 107 Myr (dashed).

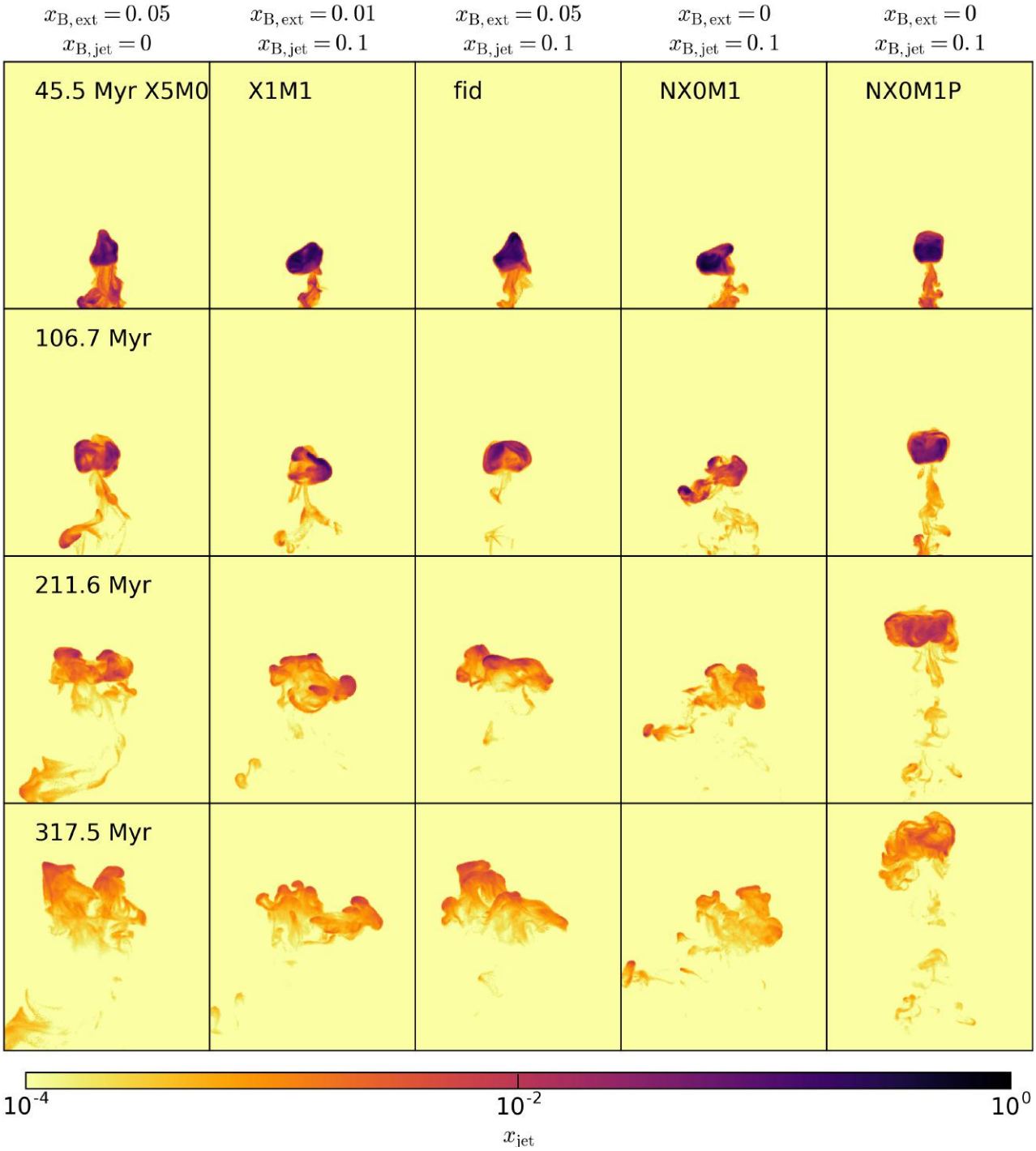

Figure 4.8: Evolution of the jet tracer mass fraction x_{jet} for indicated runs (left-right) and times (top-bottom). Projections have dimensions 120kpc − 100kpc − 100kpc centered at $(60, 0, 0)$ and are weighted with the jet mass $x_{\mathrm{jet},i}\ m_i$.

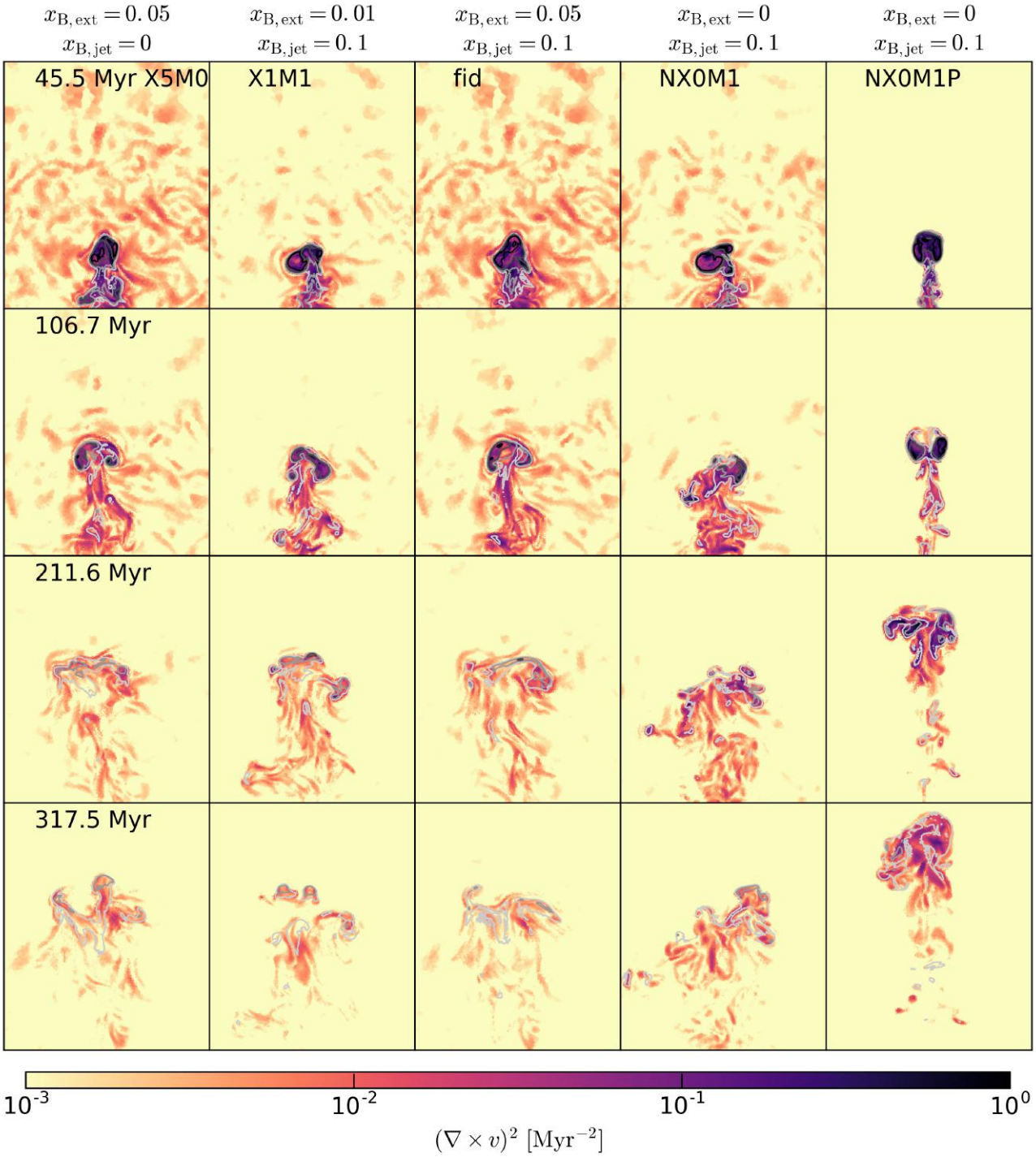

Figure 4.9: Evolution of the vorticity $(\nabla \times v)^2$ for indicated runs (left-right) and times (top-bottom). Projections have dimensions 120kpc − 100kpc − 4kpc each centered at $(60, 0, 0)$ and are weighted with the jet mass $x_{\mathrm{jet},i}\ m_i$. Contours represent x_{jet} from light to dark at 10^{-4}, 10^{-3}, 10^{-2}, 10^{-1} and are volume-weighted.

b) **Time of disruption** Defining the exact time of disruption of a bubble in the simulations is ambiguous. There are different disruption times depending on whether one requires the low-density bubble to simply be connected or whether one is interested in the time of maximum energy deposition into the IGM.

The vertical spread of the shell and the lower magnetic field energy (at later times / higher altitudes) decreases the stability of the bubble. The central region of the bubble appears the most vulnerable part. The vortex flows can interact and cancel their respective horizontal velocity contributions such that the vertical component dominates. The vertex-flows might push bubble material to either side of the lobe and penetrate the bubble at late times. Consequently, the bubble splits and two independent bubbles are created.

For the quiescent case, the disruption of the bubble surface occurs early as the vorticity-induced, upwards-moving flow is able to penetrate the center of the bubble surface (Figure 4.8). However, the remaining torus continues its path upwards in the cluster atmosphere. Also, if the strong vorticity in the wake of a turbulent environment has disrupted a bubble, the bubble normally is split in half. If enough material remains in the two newly created low density concentrations, these two new bubbles continue to rise. This can be deduced from Figure 4.8, where all simulations but the quiescent case show such a behavior.

As discussed, the magnetic field affects the morphology of the bubble and the concentration of bubble material. Interestingly, no significant differences in the final tracer distribution (Figure 4.8) become apparent. In the absence of turbulence, the bubble can freely rise upwards, which explains the higher altitude of run NX0M1P. Run NX0M1 is more prone to the KH instability that leads to larger degrees of mixing. The buoyancy rise time of the diluted gas density increases.

4.1.2 Dependence of jet parameters on evolution

So far, we studied the impact of the external and internal magnetic field of the jet on the morphology of the bubbles and their evolution. Now, we focus on

- duration of jet activity $t_{\rm jet}$,
- resolution,
- jet power $P_{\rm jet}$.

They affect the outcome of the simulation with regard to the traveled distance of the jet and the final anisotropy of the jet material. These properties are crucial for assessing the viability of jets as sources of the feedback in CC clusters.

Jet power

To compare the influence of varying the power of the jet $P_{\rm jet}$ (a free parameter in the current model), we show projections of the density in Figure 4.10 for runs with varying jet power at 81 Myr after jet launch. The simulations are rotated (bottom-up) to account for projection effects. The jet activity $t_{\rm jet}$ in all simulations was left at the fiducial value of $t_{\rm jet} = 10$ Myr. It can be seen that, for higher jet powers, the lobes propagate further and the bubbles become significantly larger. This can be explained with a surplus of kinetic energy in the high-powered jets.

Initially, low-power bubbles show a larger angle of deflection in the horizontal direction than the higher-power runs (Figure A.2). At around 200 Myr, bubbles start to break up and the remnants continue to rise (Figure A.3). The timescale appears independent of power, which will be studied in more detail in the future. The fragmentation process continues, especially for the high power runs, spreading their lobe material in horizontal directions (Figure A.4). In summary, the jet tracer distribution of low-power jets is confined to the center with significant relative spread in direction perpendicular to the jet.

On the other hand, the jet tracers of high-power jets fragments and spreads vertically at similar time as the low-power bubbles. In addition, jet material can reach higher altitudes, where a significant vertical spread is observable. Buoyancy forces are active for longer and the bubbles reach higher altitudes. Mixing in the bubble appears to affect a fraction of the bubble material. The presumably higher amount of vorticity created by a faster bubble cannot compensate for this.

The jet tracer distribution is relevant with regard to CR heating as it traces the CR distribution (for CR diffusion coefficients $\lesssim 10^{29}$ cm^2 s^{-1}). Consequently, to heat the inner cluster region, lower-power jets are most efficient. If the power of the jet is larger than $P_{\rm jet} \gtrsim 5 \times 10^{44}$ erg s^{-1} (with $t_{\rm jet} = 10$ Myr), the bubble will be disrupted and fragment at rather high altitudes. As shown in the next section, the jet activity has a similar effect on the CR distribution. Thus, the combination of the parameters proves crucial for the jet tracer contribution.

Figure 4.11 shows the magnetic field strength of the discussed runs. At least qualitatively, the magnetic field in the wake of the bubbles of high-power jets is significantly more enhanced than for the bubbles of low-power jets. The kinetic energy flux shows higher values in these regions. This observation and the coincidence of magnetic field amplifications and high vorticity in Figure 4.16 suggests that the cluster magnetic field is magnified through shear flows. Consequently, higher/lower kinetic energies in high-power/lower-power jets lead to stronger/smaller field amplifications.

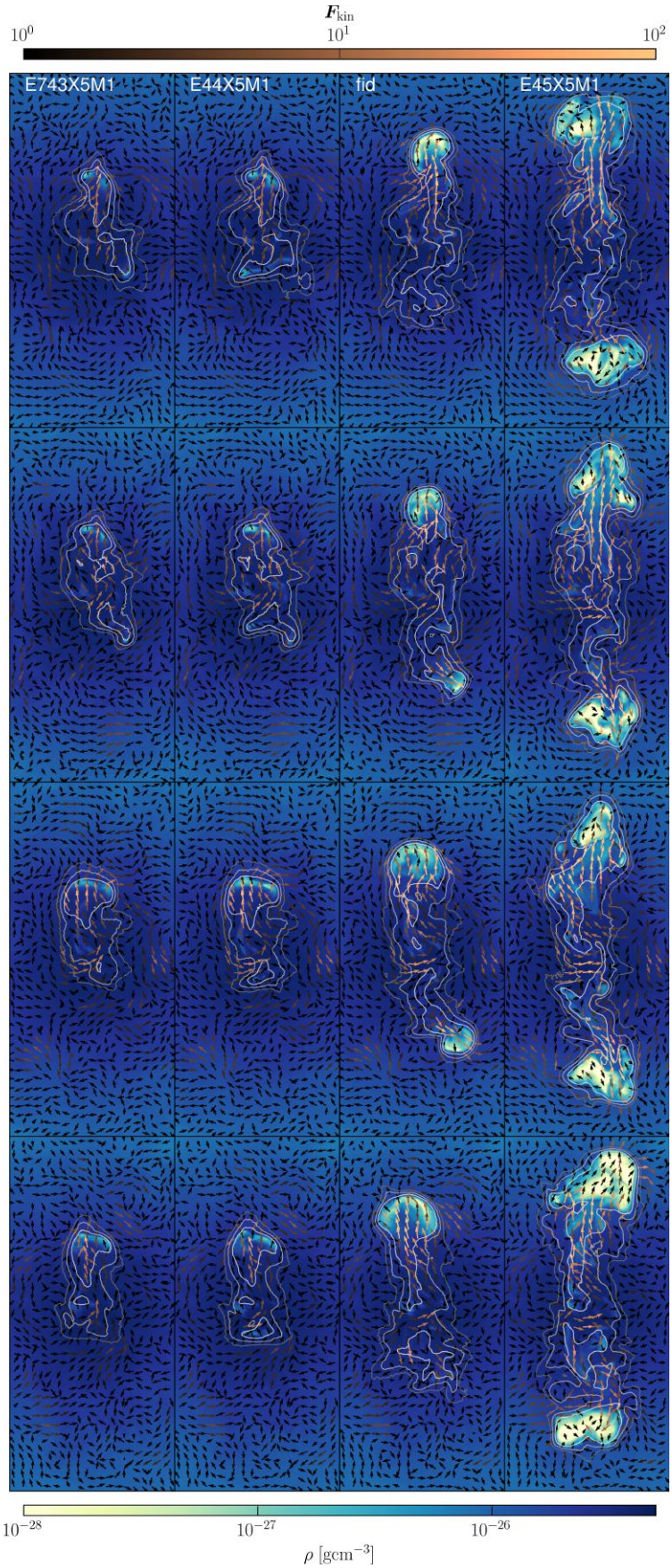

Figure 4.10: The density is shown for simulations with increasing power from left to right ($7 \times 10^{43} - 10^{44} - 3 \times 10^{44} - 10^{45}$ erg s^{-1}) at 81 Myr. A kinetic energy flux $F_{\rm kin}$ arrow plot and CR energy density $\epsilon_{\rm cr}$ contours are overlaid. Contours correspond to $10^{-13} - 10^{-12} - 10^{-11}$ erg cm^{-3} from dark to light. We display thin projections of all quantities (150kpc $-$ 70kpc $-$ 4kpc), weighted with the jet mass except for the arrows, which were obtained from a slice. The simulation has been subsequently rotated by $\pi/4$ around the vertical axis (top to bottom).

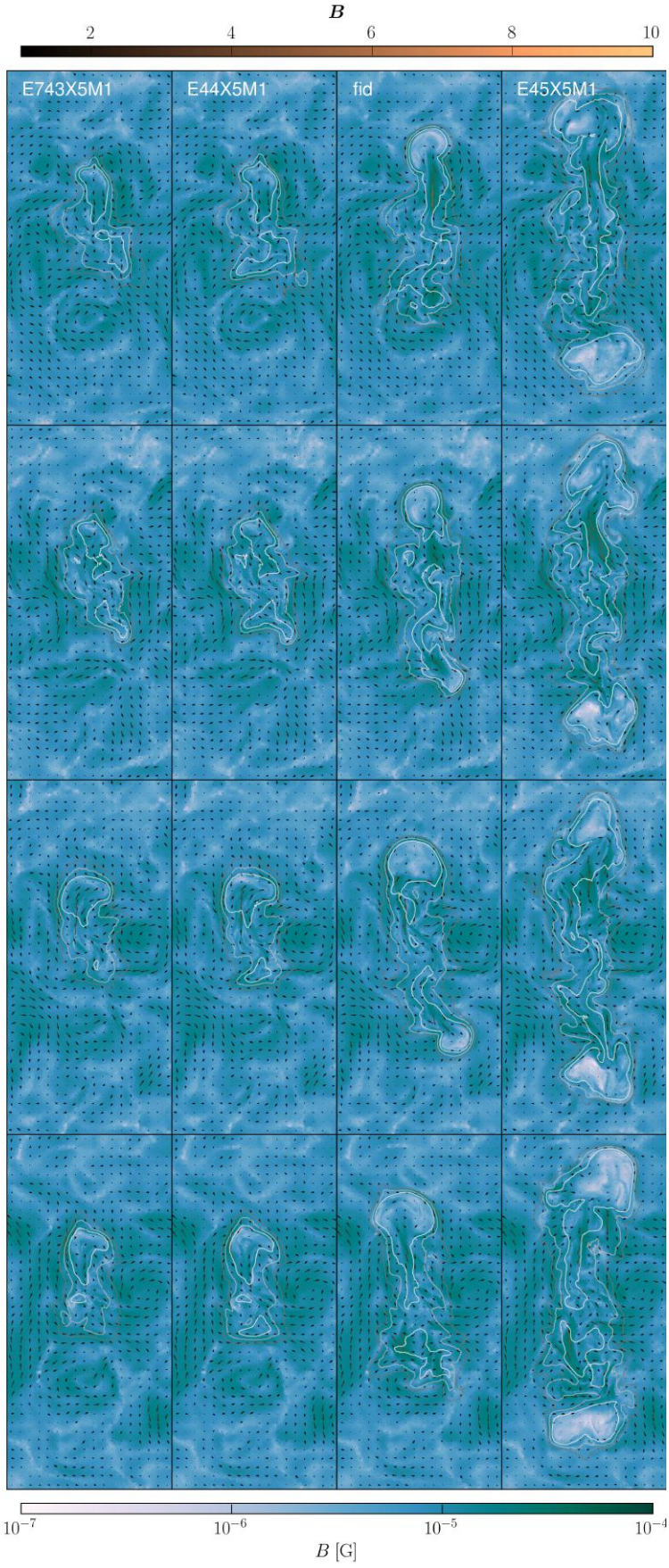

Figure 4.11: Same as in Figure 4.10, but showing the root mean squared value of the magnetic field with color and $\boldsymbol{B}$ in the $x - z$ plane with arrows.

Duration of jet activity

To study the impact of the duration of the jet activity t_{jet} with constant jet power ($P_{\mathrm{jet}} = 3 \times 10^{43}$ erg/s), runs with $t_{\mathrm{jet}} = 10, 20, 50$ Myr are portrayed in Figure 4.12. The observed trend is similar to the trend with jet power. Initially, jets with lower t_{jet} have lower kinetic energies. Their lobes/bubbles fragment at lower altitudes (Figure A.5). The relative spread of the jet tracers in horizontal to vertical direction increases for lower t_{jet}. At around 200 Myr, the bubbles break up (see Figure A.6). A smaller bubble rises from the center of run X5M1MY5, which is possibly an artifact of the jet implementation (see below). At later times, the bubbles in runs with larger t_{jet} fragment in the cluster atmosphere and spread more in horizontal direction. The bubbles with high t_{jet}, seen in Figure A.7 at 422 Myr, still have significant jet tracer fractions and their subsequent spread appears to be limited by the runtime of the simulation.

Conclusively, the energy of the bubble appears to be the relevant quantity rather than the activity of the jet or the power of the jet. In the future one could try to vary P_{jet} and t_{jet} such that the total injected energy stays constant, i.e. $P_{\mathrm{jet}} t_{\mathrm{jet}} = \mathrm{const}$. This would allow for more quantitative statements.

In run XM1LO, a central peculiar low density blob is visible in the east of the central BH. The blob presumably originates from backflows in the two lobes, when the jet is still active. The long activity of jet allows the material in the two backflows to combine and to form the small bubble. The bubble deattaches from the main bubbles and rises slowly in the ICM. Its initial velocity is low compared to the velocity of the material in the lobes due to these interactions. This explains the small final distance to the center of the cluster compared to either lobes.

The magnetic field strength of the central region is extraordinary low, as seen in Figure 4.13. This is the result of the magnetic isolation of the bubble. The algorithm projects the radial magnetic field component threading the jet surface. As no additional magnetic field is injected in the center and the cleaning process is active for a long time, the removal of magnetic fields becomes significant (see Section 4.2.2). However, this effect should not have a significant impact on our work.

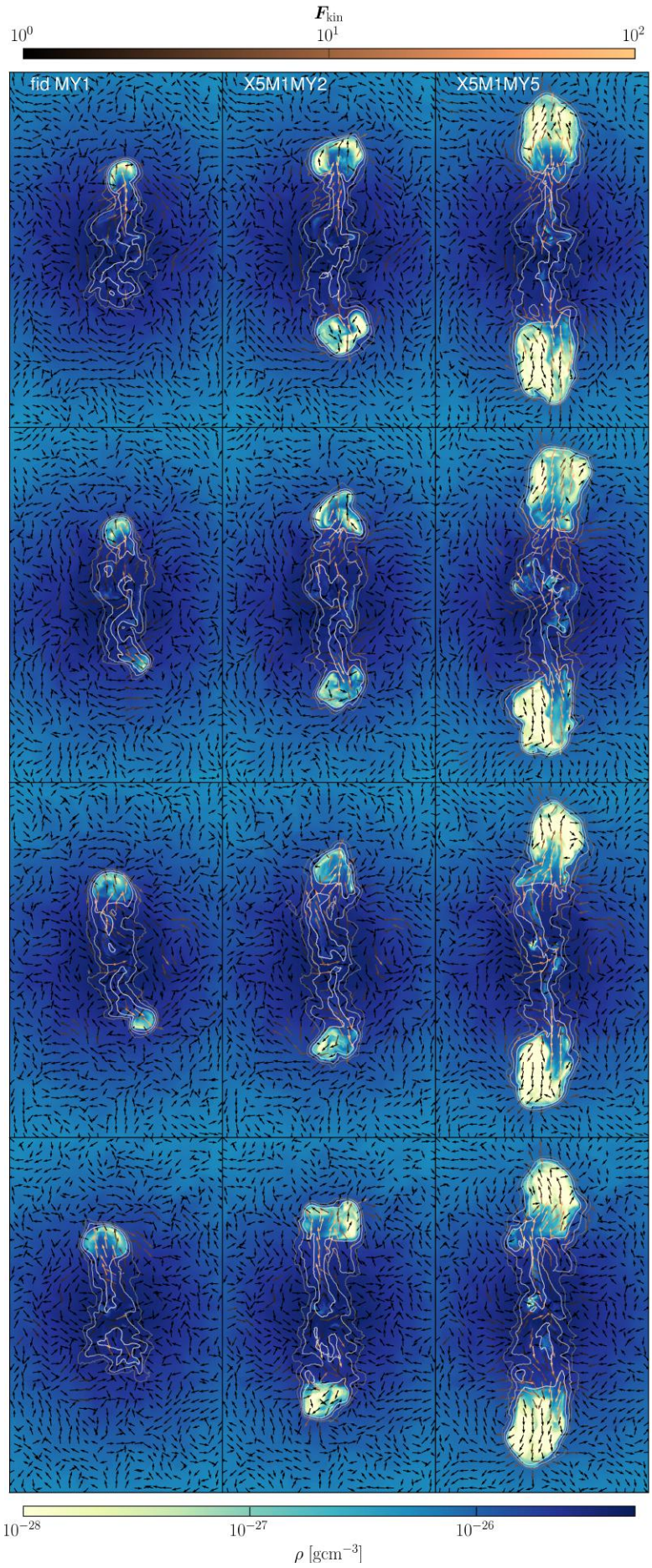

Figure 4.12: Same as Figure 4.10. Here, the density is shown for simulations with increasing jet activity from left to right ($t_{\rm jet} = 10, 20, 50$ Myr). The dimensions of the projection box also changed to 200kpc − 120kpc − 4kpc.

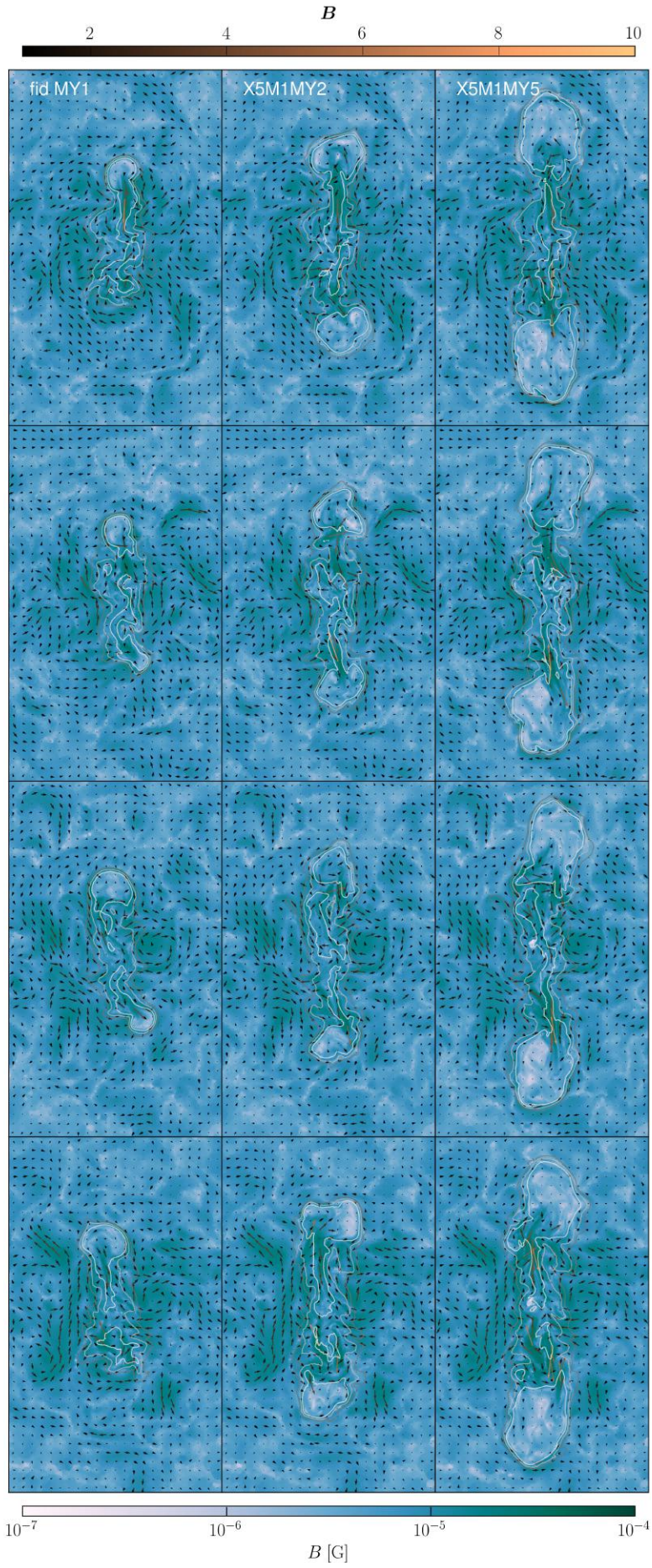

Figure 4.13: Same as in Figure 4.12, but showing the root mean squared value of the magnetic field with color and $\boldsymbol{B}$ in the $x-z$ plane with arrows.

Resolution

Turning to the resolution dependence of evolutionary features of the bubble, we show the evolution of a low resolution run with otherwise fiducial parameters in Figure 4.14. From the density evolution, the bubbles are observed to mix more than in the fiducial run. The velocity in the low resolution jet is lower compared to the jet in the high resolution run. Here, the kinetic energy flux is injected in larger cells. To resolve the contrast in velocity between jet and surrounding lobes a minimum number of cells is required. In the fiducial run, on the order of five cells are affected. Correspondingly, a similar number of cells is required to resolve the low resolution jet, which increases its radius.

In the low resolution run, a backflow combines the two forming lobes. The newly formed low-density bubble rises independently from the two main bubbles. The stronger backflow possibly arises from residual magnetic lines that still connect the two injection regions. Gas from one region can flow along the field lines and mix with the gas from the other region. Their momenta partially cancel and the newly formed buoyantly bubble rises.

In addition, the two main bubbles are observed to rise to considerably lower altitudes compared to the run with fiducial resolution. The wider jet creates a wider working surface, which spread its momentum. The bubble is assumed to rise to lower altitudes. In addition, more efficient mixing dilutes the material, which lowers its buoyant velocity.

From the general evolution of the bubble and Figure 4.15 the process of draping is independent of resolution. However, the magnetic field amplification seems to be absent in Figures 4.15, 4.14. The lower velocity results in a considerably smaller amount of vorticity, which appears crucial to enhance the magnetic field.

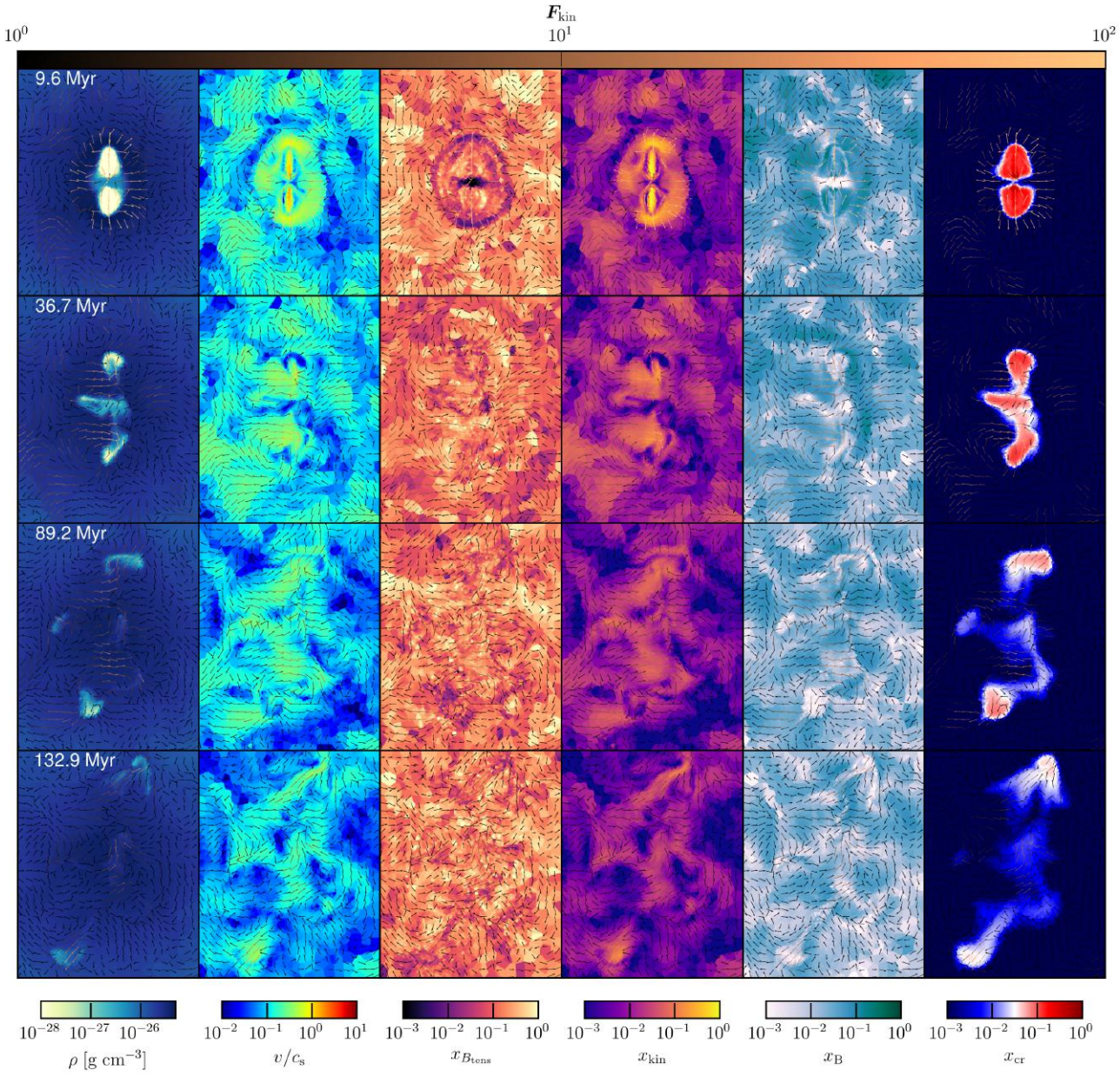

Figure 4.14: Same as Figure 4.1 for the low resolution run as defined in Table 3.1. Here, the dimensions of the box are 100kpc − 80kpc − 4kpc centered on the BH.

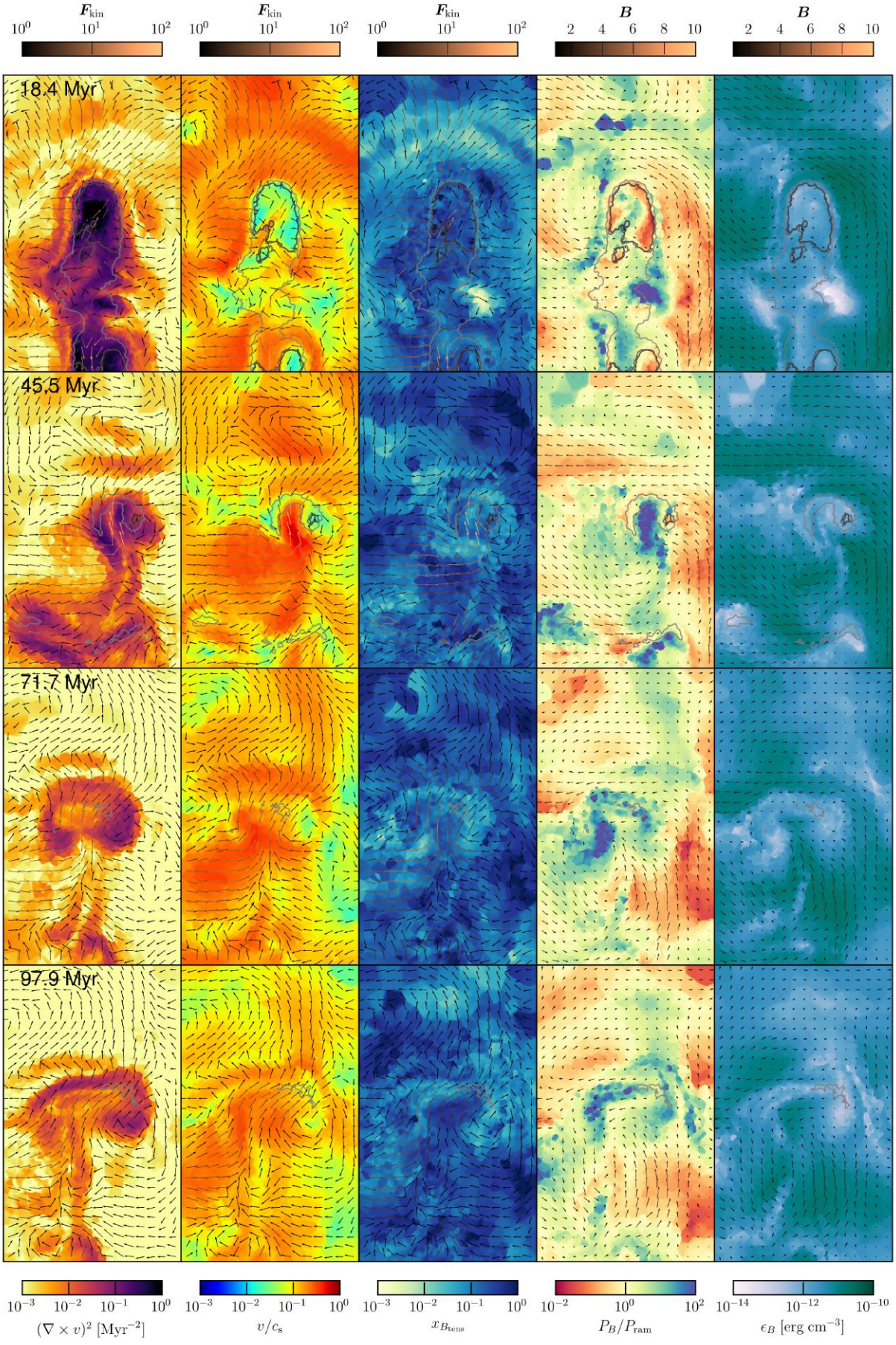

Figure 4.15: Same as in Figure 4.16 for the low resolution run.

4.2 Bubble influence on external magnetic field

4.2.1 Draping of bubble

As discussed in Section 4.1.1, the external magnetic field provides significant stability to the bubble. The external magnetic field lines are swept up by the buoyantly rising bubble. They provide stabilizing magnetic tension to the shell of the bubble. The density of field lines is limited by the resulting magnetic pressure. Excess field lines are advected over the hull of the bubble. This process is referred to as (magnetic) draping by Dursi and Pfrommer (2008). The draped layer of magnetic fields constrains anisotropically diffusing CRs within the bubble to only escape at the lower end of the bubble, which is not draped.

Dursi and Pfrommer (2008) find the ratio of magnetic-to-ram pressure $P_B/P_{\rm ram}$ to be the crucial parameter to identify the draping layer, where $P_B/P_{\rm ram} \approx 1$. This ratio, the gas-to-signal speed $v/c_{\rm s}$, magnetic tension to total forces $P_B/P_{\rm ram}$ and the magnetic energy density ϵ_B are shown in Figure 4.16. The bubble can be identified as a low-density cavity with low degrees of magnetization and high temperature, which results in a higher signal speed (lower $v/c_{\rm s}$). The outer density contour approximately traces the boundary layer of the bubble. The magnetic-to-ram pressure ratio is observed to increase at this layer.

The value of $P_B/P_{\rm ram} \approx 1$ is approximately reached. In addition, the magnetic field shows enhancement as a magnetic layer ($\boldsymbol{B}$) with the field vectors pointing along the bubble. For similar simulations with a turbulent atmosphere (Ruszkowski et al. 2008) the effect of draping is also observed. As becomes evident from Figure 4.16, the bubble is constantly redirected by the ambient medium. However, it stays confined for longer than 100 Myr and constantly changes its morphology due to the combination of external turbulence, magnetic field alignment (magnetic tension), magnetic pressure and strong turbulence within the bubble (4.16).

Studying the magnetic field structure close to the surface of the bubble is severely impeded by the turbulent nature of the background. Figure 4.17 shows a slice of the absolute value of the magnetic field of the bubble at 98 Myr. Each consecutive image has been rotated along the vertical axis by $\pi/3$ (from left to right). The average of the magnetic field is computed along the indicated cylinder, which is tilted with respect to the vertical axis. The cylinder is oriented such that it threads the surface of the bubble approximately along the normal of its surface and passes through the center of the bubble.

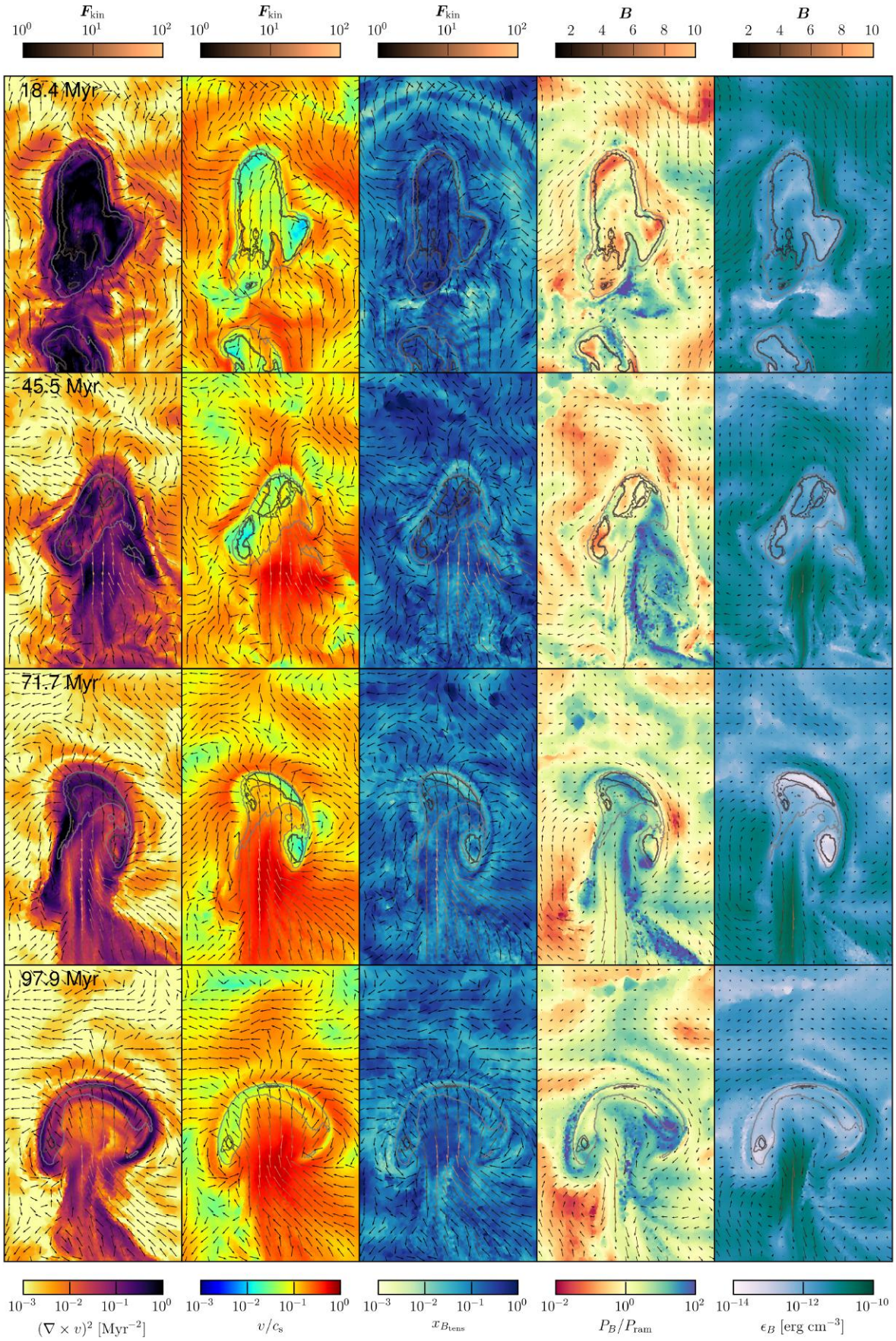

Figure 4.16: The velocity in units of the sound speed $v/c_{\rm s}$, the magnetic tension to total forces ratio $P_B/P_{\rm ram}$, the magnetic-to-ram pressure ratio $P_B/P_{\rm ram}$ and the magnetic field energy density ϵ_B are shown for intermediate times of the fiducial simulation. Arrows show the relative kinetic energy flux $F_{\rm kin}$ and the magnetic field $\boldsymbol{B}$ on top of (jet mass-weighted) projections with 50 kpc − 30 kpc − 4 kpc. Contour lines corresponding to gas densities ρ of $8 \times 10^{-28}, 10^{-27}, 7 \times 10^{-27}$ cm^{-3} are overlaid.

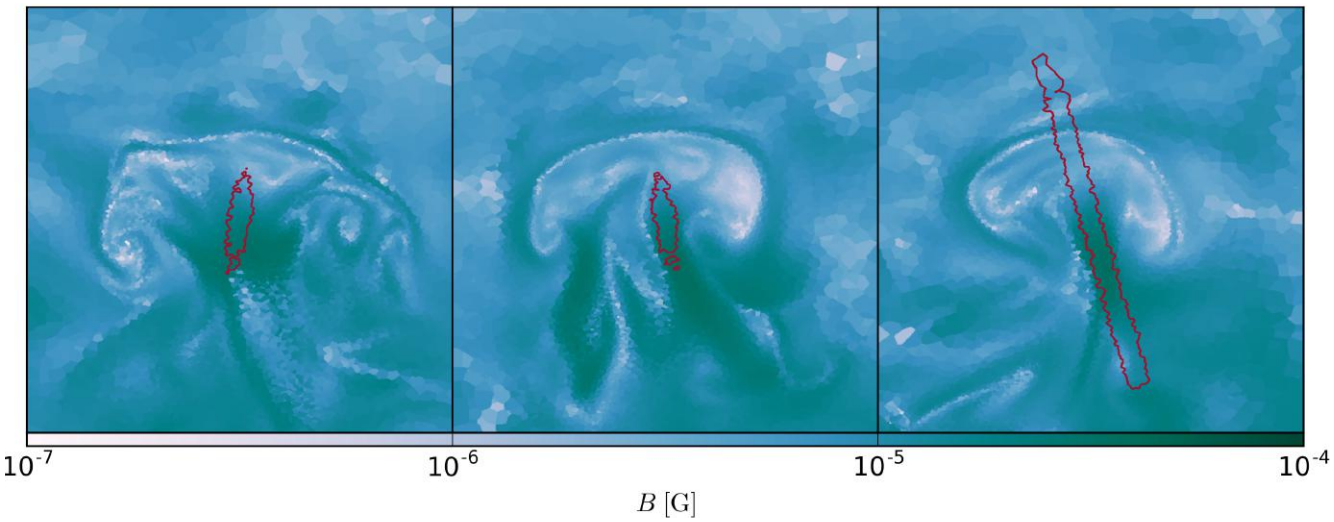

Figure 4.17: The absolute value of the magnetic field B is shown at 98 Myr. The second and third image are rotated by $\pi/3$ and $2\pi/3$ $\pi/3$ around the vertical axis. Contour lines correspond to the extend of the cylinder with radius $r = 1$ kpc, which is used to average the magnetic field as shown in Figure 4.18. All quantities correspond to slices with dimensions 50 kpc − 40 kpc centered on the bubble.

We show the volume-weighted average of the absolute magnetic field along the cylinder in Figure 4.18 with bins containing the same amount of cells. The dominant peak in the magnetic field profile is due to magnetic field amplifications in the wake of the bubble, which will be described in the next section. At a distance of 10 kpc from the center of the bubble the magnetic field is also increased. Comparing the position with the outer layer of the bubble in Figure 4.17, enables us to identify this as the draped magnetic field layer. The result is in agreement with previous idealized simulations (Dursi and Pfrommer 2008) as described in Section 2.1.5. However, the layer is less well-defined. Irregularities due to the turbulence impair the accuracy of the radial profile.

We also show the distribution of selected cells N_{cell} in equidistant bins. The number of available cells traces the resolution of the simulation that is given by the refinement criteria (see Section 3.2). The excess of cells in the bubble results from the volume and jet tracer criteria. To resolve the draping layer, the criterion based on the density gradient proves crucial. The draping layer appears reasonably resolved. Increasing the radius of the cylinder increases the statistics but at the expanse of smearing the surface layer.

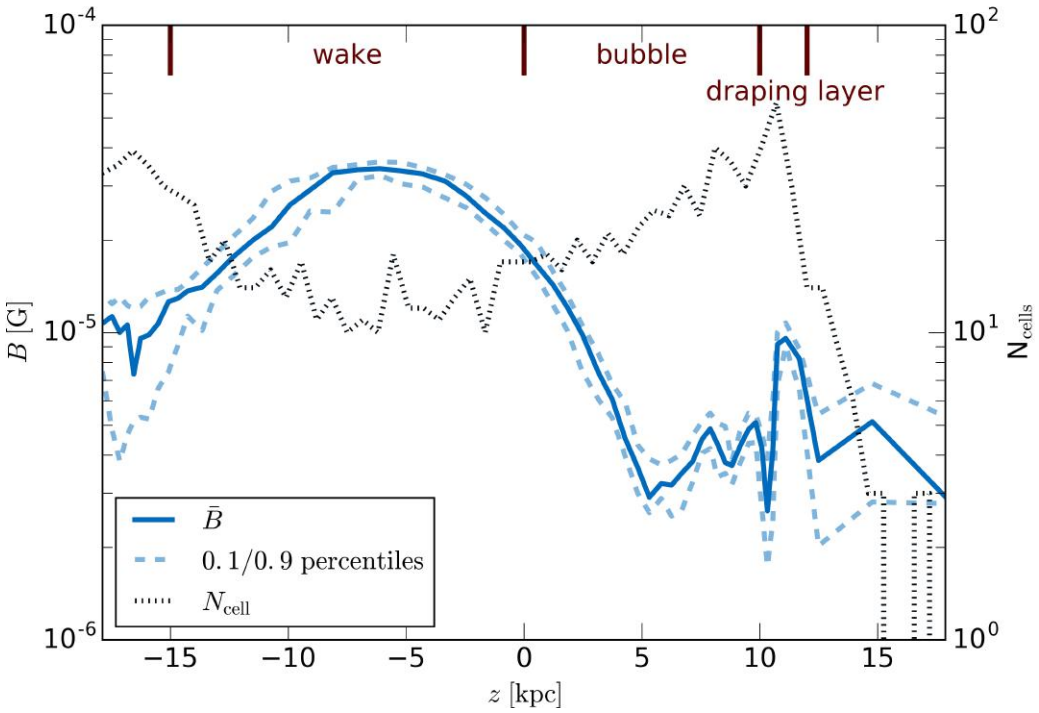

Figure 4.18: The average magnetic field along the stagnation line is shown as a function of distance from the center to the bubble. The dark blue line corresponds to the volume averaged magnetic field with upper (90%) and lower (10%) percentiles indicated as lighter dashed lines for bins with equal number of cells. The black dashed line characterizes the number of cells in equidistant bins, which traces the morphology of the bubble. The magnetic field is significantly amplified in the wake of the bubble ($z \lesssim 0$) and peaks around 10 kpc which corresponds to the draped magnetic field layer.

4.2.2 Dynamo in wake

In the wake of the bubble, the magnetic field is amplified. In Figure 4.16, the magnetic field just below the bubble is increased by an order compared to the environment. This mechanism becomes active between 20-50 Myr. Correlation analysis suggests that the mechanism is based on a dynamo effect and/or adiabatic compression induced by the significant level of vorticity in the wake of the bubbles. To study the evolution and parameter dependence in more detail, the average magnetic energy density is shown as a function of time for runs with varying magnetic field parameters (Figure 4.19) and jet parameters (Figure 4.20). The magnetic field energy density ϵ_B has been averaged in a cylinder $C_{\parallel}$ with radius 10 kpc, which is centered on the BH extending between the bottom of the two bubbles. For comparison, ϵ_B is averaged in a cylinder $C_{\perp}$ with the same dimensions perpendicular to the original one. In Figure 4.21, both cylinders are superimposed on the magnetic field energy density of the fiducial run at 90 Myr.

Initially, all runs have a larger magnetic field in $C_{\perp}$ than in $C_{\parallel}$. At this time, the height of the cylinder is smaller than its radius. This effectively causes the regions that $C_{\perp}$ and $C_{\parallel}$ probe to switch. In addition, the depletion of magnetic fields due to the magnetic isolation of the jet region has to be kept in mind. For this, Figure 4.23 shows the magnetic field strength around the BH at 18.4 Myr for the fiducial run as well as for a run without magnetic isolation.

In the fiducial run, the low magnetic field residuals from the isolation are advected from the jet injection region. On the contrary, high magnetic fields connect the two jet regions in the

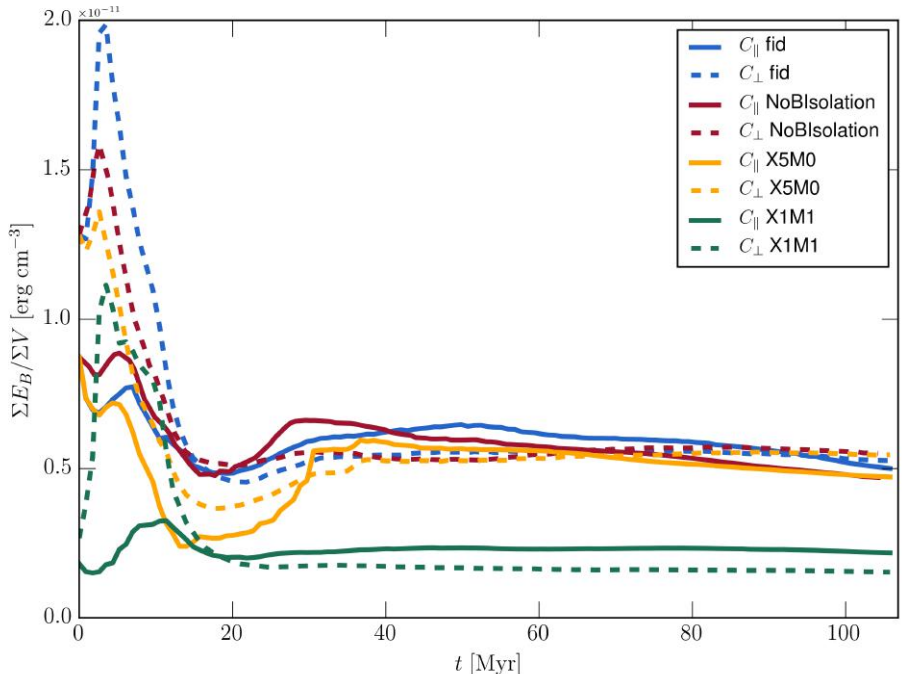

Figure 4.19: The average magnetic energy density $\Sigma E_B/\Sigma V$ is plotted as a function of time of runs with different magnetic fields parameters. The average was computed in cylinders centered on the BH with radius 10 kpc and a height spanning in between the bottoms of the bubbles at respective times. For the dashed lines the same average was taken within a cylinder, that was rotated by $\pi/2$ with respect to the original cylinder.

comparing run. The result of the magnetic field structure can be seen in the density evolution, which is shown in Figure 4.22. In the fiducial run, the two lobes are clearly separated, which is in agreement with observations (Section 2.1.3). On the contrary, the run without magnetic isolation shows interactions between regions. Here, magnetic field lines connect the two regions spatially and thereby dynamically.

A low-density cavity is observed in the central region. The under-dense jet leads to the expulsion of a significant mass fraction from the central region. The redistribution process leads to a net mass loss in the center. For the fiducial jet powers and periods of activity, the density contrast of the cavity corresponds merely to a factor of three. In the regime of higher $P_{\rm jet}$ and $t_{\rm jet}$, this corresponds to a significant mass depletion in the center. Then, major consequences are expected for the stability of the simulation. In general, this magnetically-depleted region represents a low-density cavity, which is unstable to buoyancy and subsequently rises in the cluster atmosphere, in many cases, in the wake of either bubble. Consequently, the magnetic field strength in $C_\parallel$ is decreased.

In Figure 4.19, at intermediate times ($\sim$ 30 Myr) the magnetic field enhancement in region $C_\parallel$ compared to $C_\perp$ is visible. The ratio approaches unity at $\sim$ 90 Myr. The decrease of the enhancement is partly due to the horizontal distance of the lower bubble, whose wake is not fully included in $C_\parallel$ anymore. On the other hand, run X1M1 shows the clearest amplification. The weaker magnetic field less severely deflects the bubble, which makes the dynamo more efficient. In addition, the cylinders are well suited to follow the evolution of the bubbles. In run X5M0, the amplification is only detected for a short period. As discussed in Section 4.1.1, unmagnetized bubbles fragment more often and thereby mix more efficiently. Consequently, a decrease in the buoyancy velocity is expected, which decreases the vorticity in the wake of the

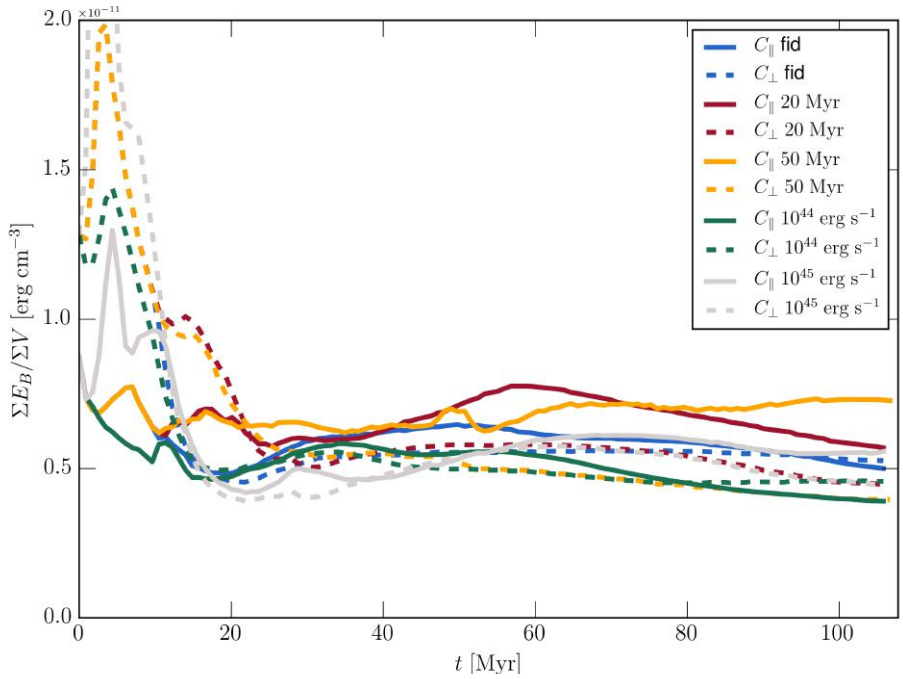

Figure 4.20: Same as Figure 4.19 for runs with different jet powers and jet activity.

bubble. The dynamo becomes less efficient.

In Figure 4.20, the ratio of magnetic field amplification scales with the duration of the jet activity $t_{\rm jet}$. As discussed in Section 4.1.2, higher $t_{\rm jet}$ translates to higher velocities of bubbles and consequently, higher vorticity in the wake of the bubble. The dynamo is more effective. In the case of run X5M1MY5, a significant magnetic field depletion in the central region is present, which can be compensated by the gain in magnetic field amplification.

Interestingly, run X5M1MY2 shows stronger enhancement than run E45X5M1, even though more energy was injected in run E45X5M1. In the case of high jet powers (run E45X5M1), a clear central magnetically-depleted cavity exists. The strong backflows in the two jets is able to connect the two lobes. The two rising bubbles drag material along their wake. Consequently, the magnetic field starts out with lower initial field strengths, which weakens the dynamo. The vorticity is also spread over a larger area. Thus, magnetic enhancement through adiabatic compression becomes less efficient.

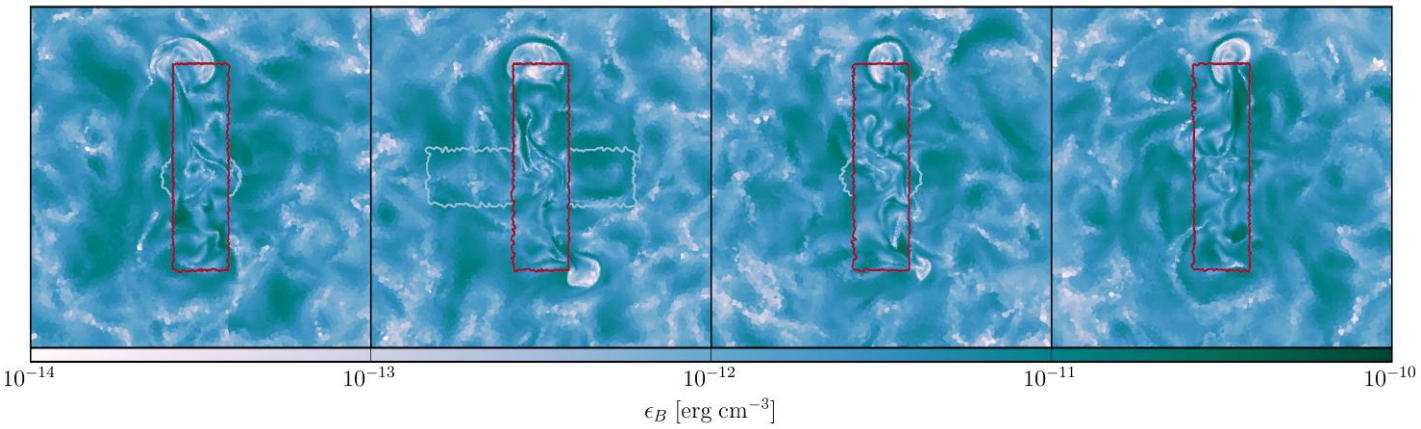

Figure 4.21: A slice of the magnetic field energy density ϵ_B of the fiducial run at 81 Myr. From left to right the images have been rotated by $\pi/4$, respectively. The red contour line corresponds to the cylinder approximately enclosed between the two bottoms of the bubbles. The enclosed cells are used to determine the average magnetic energy density. The cylinder with the same dimension has then been rotated by $\pi/2$ (shown in grey) to calculate an averaged comparison value. The slice have dimensions 120 kpc − 120 kpc centered on the BH.

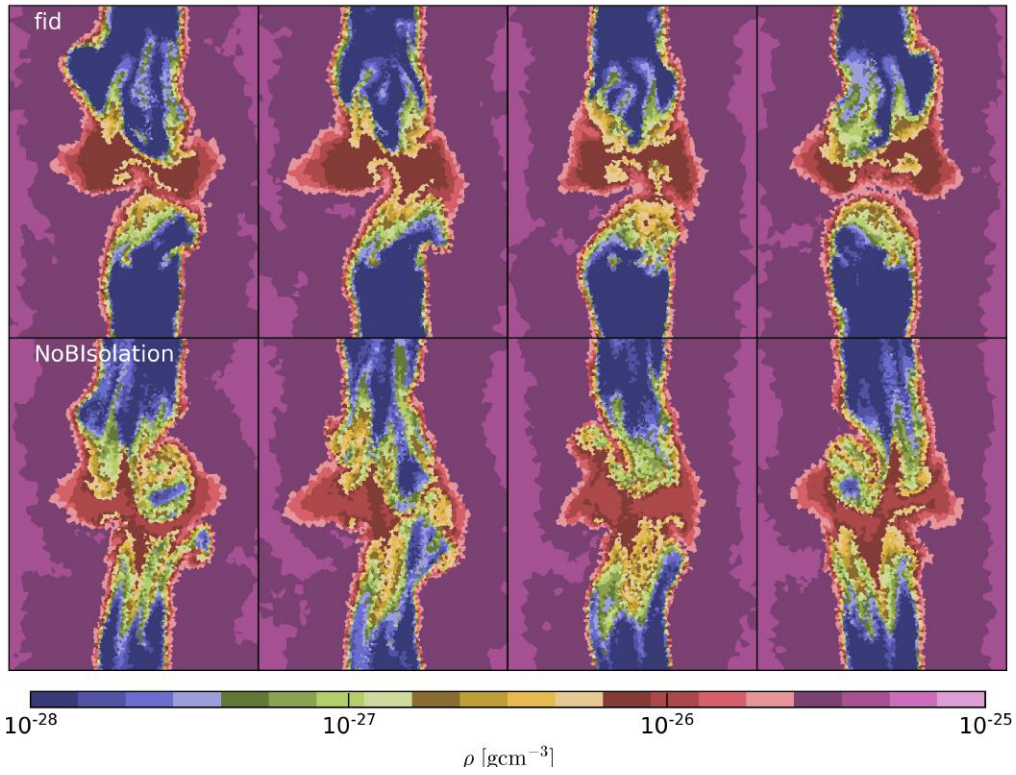

Figure 4.22: Slices of the central cluster density ρ at 18.4 Myr. From left to right the images have been rotated by $\pi/4$, respectively. The slices are centered on the black hole and have dimensions 40 kpc − 30 kpc.

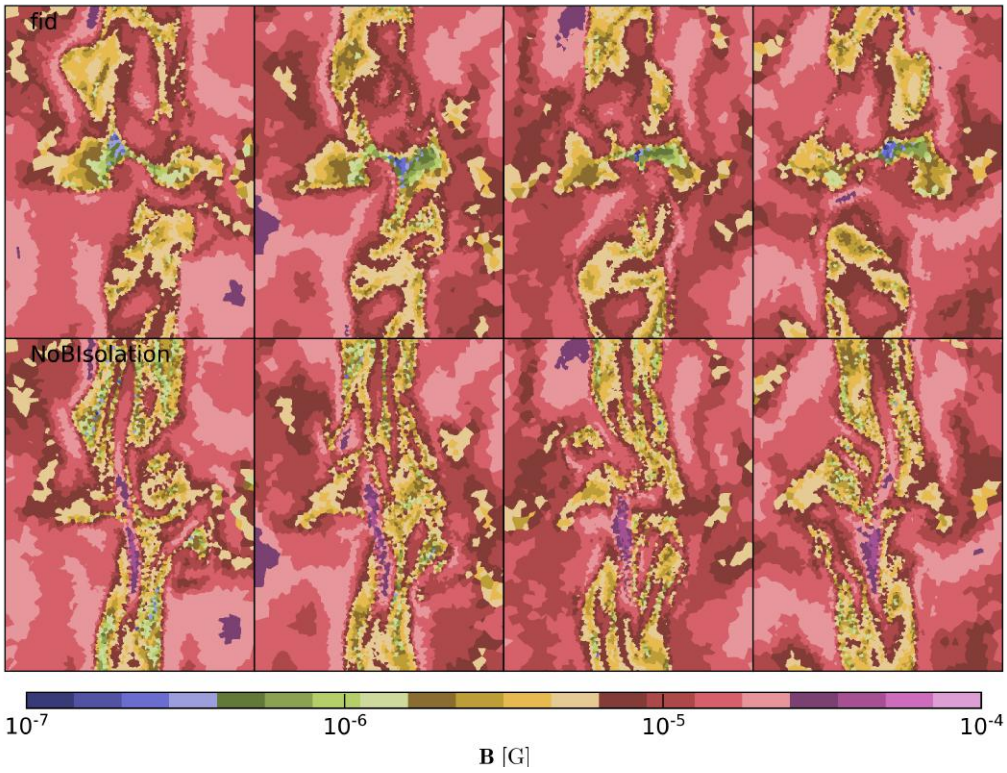

Figure 4.23: Same as in Figure 4.22 for the absolute magnetic field strength.

4.3 CR distribution

We now examine the spatial distribution of CRs for different CR transport processes and discuss the impact of a single AGN outburst on CR Alfvén cooling. The volume covering fraction and isotropy of the CRs, which are initially contained in the bubble, is essential for the viability of the CR heating model for CC clusters (Section 2.1.4). We note that in order to study study self-regulated heating and radiative cooling CC cluster multiple injection events have to be considered. In addition, jet energies may differ considerably.

4.3.1 Diffusion coefficient and cooling timescale

In the CR fluid model, CRs are to first order confined to the magnetic field that is flux frozen in the plasma. Thus, they are only advected with the gas. In addition, they can stream and diffuse relative to the gas. Here, we consider the streaming instability, which causes the CRs to move along magnetic field lines with a drift velocity relative to the gas. In a cluster environment, we have shown that the drift velocity $v_{\rm D}$ approximately corresponds to the Alfvén speed, $v_{\rm A}$ (Section 2.2.2), i.e., $v_{\rm D} - v_{\rm A} = c^2/\nu L_{\rm cr}$, where ν is the pitch-angle scattering rate and $L_{\rm cr} \sim P_{\rm cr}/\nabla P_{\rm cr}$ is the CR gradient scale (Kulsrud 2005). In addition, CRs diffuse along the field lines with a diffusion coefficient $D_{\parallel} = c^2/\nu = (v_{\rm D} - v_{\rm A})L_{\rm cr}$. Thus, spatial diffusion is negligible here. Analogously to Sharma et al. (2009), we interpret the numerical diffusion coefficient of the CRs, κ, as an effective diffusion coefficient that combines spatial diffusion as well as CR streaming. Its value can then be estimated by $\kappa_{\rm cr} \sim v_{\rm A} L_{\rm cr}$. In practice, the Alfvén velocity and the CR diffusion length scale depend on the CR injection mechanism and the cluster environment. We chose a fiducial value of $\kappa \sim 10^{29}$ cm^2 s^{-1} as it yields approximately self-consistent results in the cluster environment. The value is also in agreement with the measured Galactic diffusion coefficient $\kappa_{\rm MW} \sim 10^{28}$ cm^2 s^{-1} for $\sim$ GeV particles, since $v_{\rm A} \sim 30$ km s^{-1} and $L_{\rm cr} \sim 3$ kpc (Berezinskii et al. 1990).

In Figure 4.24, we show projections of the CR energy density $\epsilon_{\rm cr}$, the Alfvén cooling timescale $t_{\rm A} \sim \epsilon_{\rm cr}/\Delta\dot{\epsilon}_{\rm cr,A} \sim \epsilon_{\rm cr}/(v_{\rm A}\nabla P_{\rm cr}) \sim L_{\rm cr}/v_{\rm A}$ (see Section 2.3.2), the Alfvén velocity $v_{\rm A}$, the estimated CR diffusion coefficient $\kappa_{\rm cr,A} = v_{\rm A} L_{\rm cr}$, the Alfvén heating rate $\mathcal{H}_{\rm A} = -\Delta\dot{\epsilon}_{\rm cr,A} = v_{\rm A}\nabla P_{\rm cr}$ and the jet mass fraction $x_{\rm jet}$ in the fiducial run. Here, we include CR cooling in the form of Alfvén and non-adiabatic losses (see Section 2.3.2). In practice, the hadronic and Coulomb losses are sub-dominant to the Alfvén losses. However, all cooling processes ('full cooling') are active in the runs, which we analyze in this section.

Figure 4.24 shows that the employed CR diffusion coefficient $\kappa = 10^{29}$ cm^2 s^{-1} is roughly in agreement with the value expected in the CR streaming picture. However, in the wake of the bubble values in excess of the adopted values by one order of magnitude are reached.

In a low-density, highly magnetized environment, a stratified CR population is expected to cool fast. This is the configuration in the initial lobe (see Figure 4.24). Here, the Alfvén cooling time $t_{\rm A}$ is on the order of ~ 1 Myr. We assume that the CR population is accelerated and quickly establishes a uniform distribution within the bubble so that the CR population does not suffer from significant Alfvén wave losses. Thus, we prevent unrealistically high CR losses in the bubble due to numerical small-scale gradient fluctuations by disabling Alfvén cooling in cells where $x_{\rm jet} \geq 10^{-3}$. The overall cooling timescale outside the lobe is on the order of $10 - 100$ Myr. Thus, in the following the resulting CR distribution is analyzed at ~ 70 Myr for the early and at ~ 200 Myr for the late evolution.

In addition, significant deviations from this cooling times scale are observed in the wake of the bubble. As described in Section 4.2.2, the magnetic field is substantially amplified here, causing the Alfvén cooling time to reach values of order 1 Myr. In addition, the Alfvén heating

rate $\mathcal{H}_\mathrm{A}$ reaches its maximum outside the bubble. Results for a cooling CR population are limited to the fiducial run. However, this region can only correctly be accounted for if CR cooling processes are taken into account. In the future, runs with various parameters related to CRs, magnetic fields and the jet will be analyzed to quantify the robustness of our conclusions.

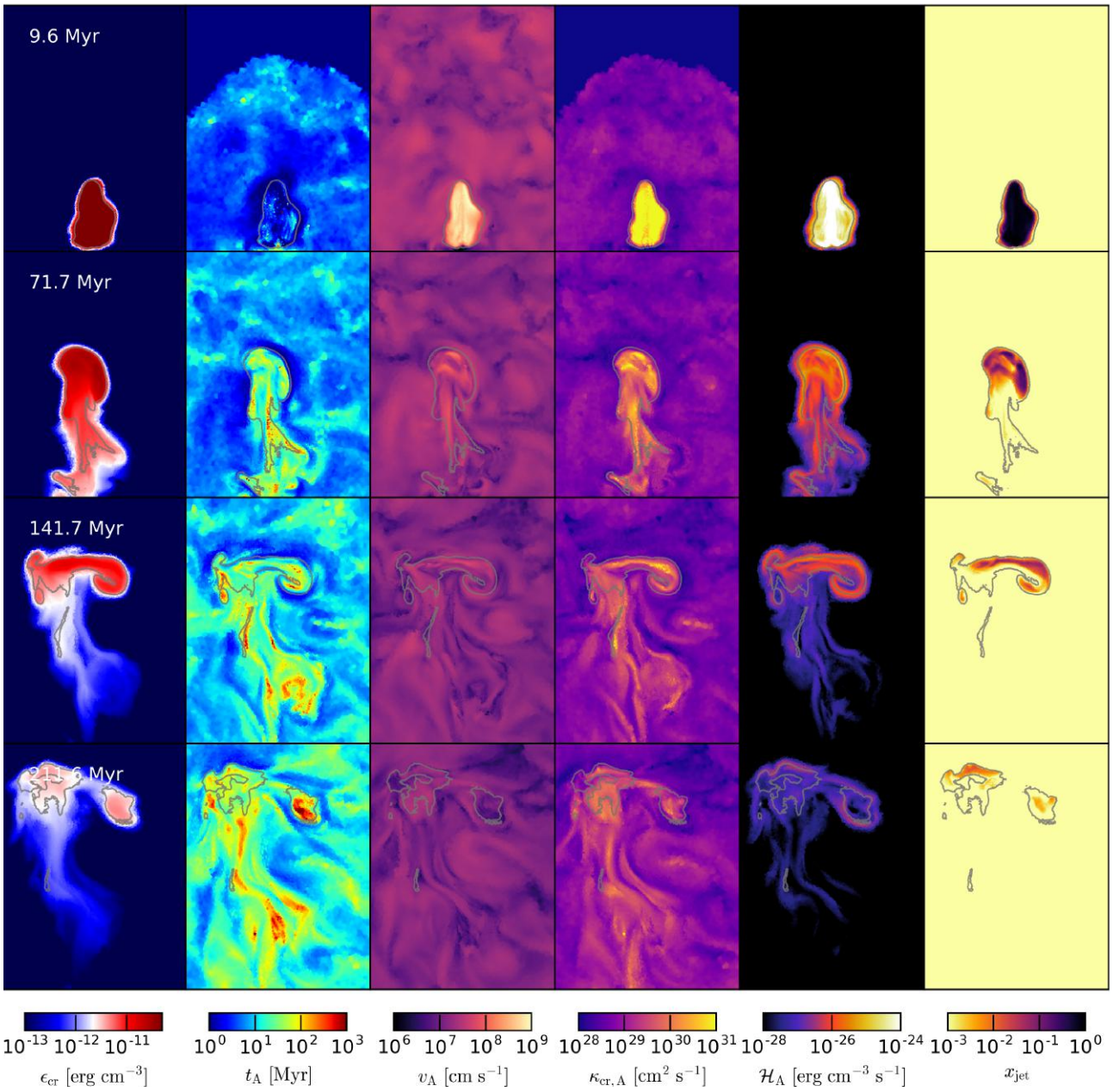

Figure 4.24: The CR energy density ϵ_cr, the Alfvén cooling timescale t_A, the Alfvén velocity v_A, the estimated CR diffusion coefficient $\kappa_\mathrm{cr,A}$, the Alfvén heating rate $\mathcal{H}_\mathrm{A}$ and the jet mass fraction x_jet are shown of the fiducial run with full CR cooling. See text for their definitions. The images correspond to thin 80 kpc − 60 kpc − 4 kpc projections weighted with the jet tracer mass fraction. The box extends from the BH at the bottom and cuts through the central region of the bubble. The grey contour corresponds to $x_\mathrm{jet} = 10^{-4}$ and is a projection of the same dimensions weighted with the volume.

4.3.2 CR covering fraction

Relevance of diffusion Semi-analytical, steady-state models of the CR-heating mechanism in CC clusters rely on one-dimensional CR injection functions (e.g., Guo and Oh 2008; Jacob and Pfrommer 2017a). To test this assumption, a self-regulating simulation is necessary. In Figure 4.25, we show the radial profile of the CR distribution for the fiducial run, the same run without diffusion, as well as a run with full CR cooling and diffusion at 72 Myr and 212 Myr. While CRs are confined to the bubble in the advection-only simulations, CRs are conducted out of the bubble along the magnetic filaments in our CR diffusion model. The run including diffusion shows a smoothly declining CR distribution terminating in an increase of $\epsilon_{\rm cr}$ at the position of the bubbles at all times. CR cooling solemnly decreases the normalization of the profile.

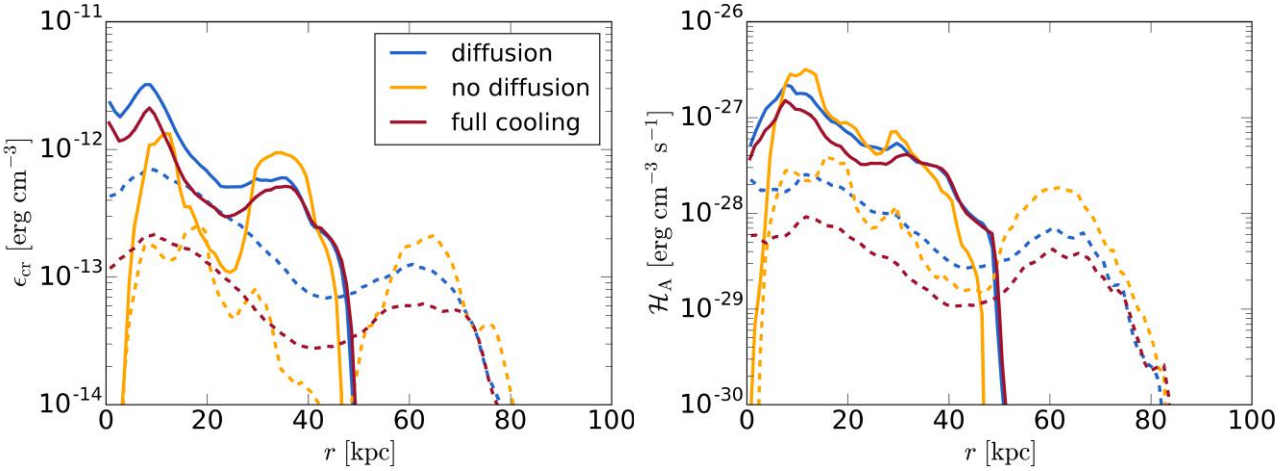

Figure 4.25: Radial profile of the CR energy density $\epsilon_{\rm cr}$ (left) and the Alfvén heating rate $\mathcal{H}_{\rm A}$ (right) of the fiducial run with CR diffusion (blue), without CR diffusion (yellow) as well as with full CR cooling and diffusion (red) at 72 Myr (solid) and 212 Myr (dashed). We obtained the profile by taking the volume-weighted mean of $\epsilon_{\rm cr}$ or $\mathcal{H}_{\rm A}$ in each radial bin.

On the other hand, if CRs are only allowed to advect, they follow closely the distribution of the bubble or its fragments. At early times, the peak close to the cluster center can be attributed to early fragmentation of the bubble (see Figure 4.8). The bubble corresponds to the second peak. More CRs remain inside the bubble such that the second peak predominates in the run with only advecting CRs compared to runs with CR diffusion. At later times, the bubble fragments and its material spreads horizontally. The wide second peak shows this trend. Inside the cluster, CRs are distributed by means of turbulent mixing.

A similar trend can be seen in the radial profile of the Alfvén heating rate. The larger isotropy of CRs amounts to a larger heating rate in the center of the cluster. In addition, the enhanced magnetic fields and high concentrations of escaping CRs lead to an increase of $\mathcal{H}_{\rm A}$ in the wake of the bubbles. Diffusion does not smooth the gradients of the purely advecting CRs, which show larger peak heating rates in comparison to simulations with CR diffusion. At 212 Myr, the more pronounced peak at the position of the bubble traces out the location of bubble fragments at this time. They exhibit larger gradients than the smoother distribution in the bubble.

The radial profile is misleading in conditions where the CR distribution is highly anisotropic. This is the case for advecting CRs and diffusing CRs at larger radii. This can be seen in Figure

4.29. Here, we show a two-dimensional phase diagram of volume in the phase diagram of the CR energy density $\epsilon_{\rm cr}$ and radius r for the fiducial run and the run without CR diffusion. Each bin is normalized with the volume of each radial shell. Collapsing this distribution along the vertical axis yields the volume fraction at each radial bin. Note the different scale of $\epsilon_{\rm cr}$ compared to Figure 4.25.

The purely advected CRs are confined to insignificant volume fractions of the cluster. The level of turbulence is insufficient in mixing them in a volume-filling fashion. On the other hand, the diffusing CRs effectively fill the inner $20-30$ kpc. However, their energy density decreases, which has an impact on the efficiency of Alfvén wave heating.

Effect of cooling The evolution of the volume occupied by $\epsilon_{\rm cr}$ as a function of radius is depicted in Figures 4.28 in the full cooling model. The cooling of CRs decreases the CR energy density. The bubble is still able to sustain high energy fractions out to large radii. One can see a clear decrease in isotropy of the cooling CR population to the fiducial run.

Initially, CRs are confined to the bubble. By construction, they are not allowed to cool. However, as discernable in Figure 4.24 or 4.5 the threshold value of $x_{\rm jet}$ only includes the outer shell of the bubble. This is the reason for the depletion of CRs in the lower part of the bubbles in Figure 4.24. However, the cooling time becomes up to three orders of magnitude smaller in the bubble. Until 212 Myr, highly concentrated CRs cool in the central region. The bubble can still be identified in both runs and contains a large fraction of the total CR population. At this point, the bubble is in the process of fragmentation, which causes the material to spread horizontally (Figure 4.8).

CR distribution and heating rates The continuous dilution of bubble material allows larger fractions of CRs in the bubble to be cooled. On the other hand, the dilution comes with an increase in cooling time. Thus, the volume filling fraction of CRs in the cluster, especially at larger radii, depends on the time scale of CR depletion. This can also be concluded from the Alfvén heating rate, $\mathcal{H}_{\rm A}$. Figure 4.30 shows the volume occupied by $\mathcal{H}_{\rm A}$ as a function of radius in the fiducial run with CR cooling at 72 Myr and 212 Myr. By analogy with the phase diagram of $\epsilon_{\rm cr}$, we normalize each bin with the volume of the radial shells.

At 72 Myr, the maximum heating rate declines from the bubble towards the center due to the increase of the CR pressure gradient and the enhanced magnetic fields. The slope is only modulated by a peak at ~ 10 kpc, which appears to correspond to CR-filled bubble fragments. At 212 Myr, the overall heating rate decreases while the bubble represents a local maximum of $\mathcal{H}_{\rm A}$.

To test for numerical resolution, Figure 4.31 shows the same phase diagram for the fiducial run and the fiducial run at lower resolution at 212 Myr. The low-resolution run shows a more centrally concentrated heating rate. The low resolution bubble disrupts earlier and the CRs are more uniformly distributed in the inner region. As mentioned above, a third bubble arises in this run, which drains entropy from the main bubbles. In addition, mixing appears to be more significant. The exact impact of numerical resolution in self-regulated systems will be analyzed in the future as it may prove critical for heating the inner-most core of the cluster. The reason for the formation and evolution of the third bubble will be more closely examined.

Interestingly, varying the degree of magnetization of the lobes or the external magnetic field shows no significant effect on the CR distribution. Figure 4.26 shows the cumulative CR energy for runs with different MHD parameters. They all show very similar trends. Thus, the difference in mixing and early fragmentation is a secondary effect. The CR diffusion timescale out of the bubbles is independent of these parameters. In addition, the final disruption of the bubbles results in similar final jet tracer configurations (see Figure 4.8). The timescales

of fragmentation are too similar to significantly alter the buoyancy timescale. However, the magnetic enhancement in the wake of the bubbles varies. In the future, CR cooling should be included in these runs to determine its importance.

In Figure 4.26, the bubble in the run without diffusion deposits only $\sim 10\%$ of the total CR energy in the inner 50 kpc. The run without magnetized lobes shows a very similar behavior to the run where the bubble was not magnetically isolated. The early CR losses due to diffusion through the shell of the bubble in the run without magnetically isolated lobes and the loss of CRs due to bubble fragmentation in the case of the run with unmagnetized lobes show a very similar trend at small radii. However, the fragmentation process translates to a continuous CR loss from the bubble in the run with unmagnetized lobes. Thus, the trends diverge at ~ 50 kpc.

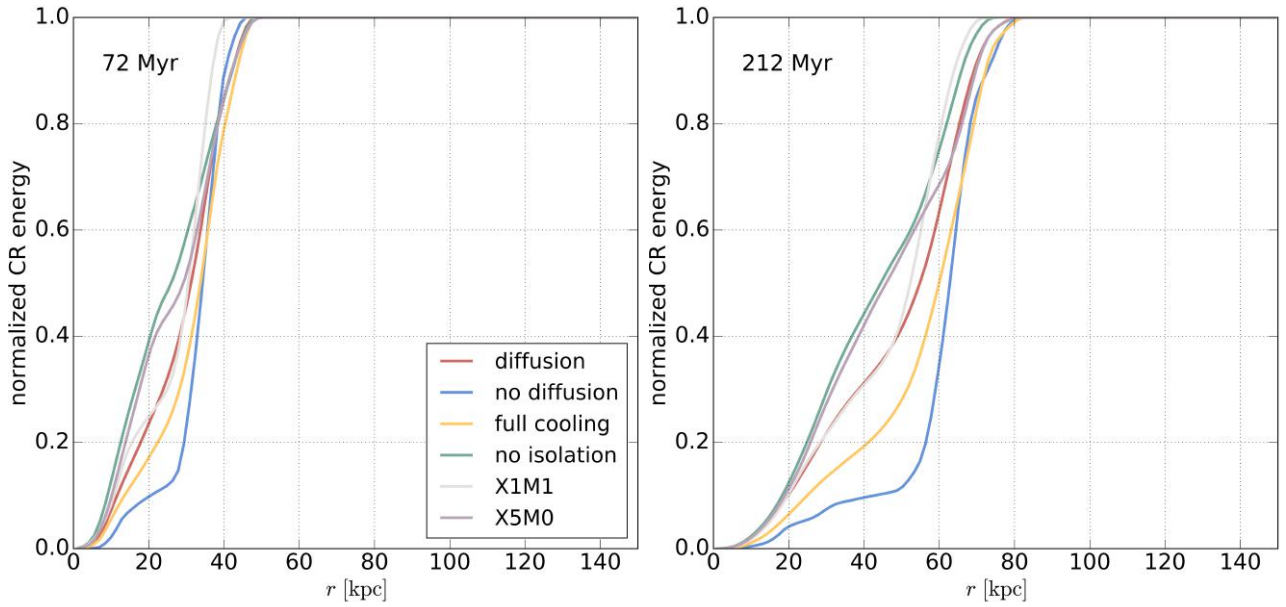

Figure 4.26: The cumulative, normalized sum of the CR energy in the indicated runs at times 72 Myr (left) and 212 Myr (right). The profiles are normalized to the total CR energy present at the respective time in the individual runs.

On the other hand, the amount of injected jet energy into the bubble is expected to significantly alter the CR distribution and thereby the CR heating rate. This parameter is responsible for the traveled distance and travel time of the bubble as argued in Section 4.1.2. Figure 4.27 shows the cumulative, normalized energy of fiducial runs with varying jet powers, resolution and time of jet activity. Energy correlates strongly with the distance of deposited CR energy for runs at the same resolution, where the higher the energy, the further the CRs are transported. The large gradient at the end of each line corresponds to the bubble, which contains a larger fraction of energy for more energetic jets. The diffusion timescale appears to vary insignificantly. A different diffusion coefficient should alter this result.

Figure 4.27 emphasizes the complexity of the resulting CR distribution in a self-regulated system. Highly energetic jets penetrate much further into the IGM. CRs will have less time to escape and heat the center of the cluster. Initial low cooling rates lead to low powered jets which stay confined to the center of the cluster and inject their energy here. In addition, the higher magnetic field enhancement in the wake of more energetic bubbles leads to stronger cooling and might increase the anisotropy of the CR distribution. Recent simulations of self-regulated systems (Yang and Reynolds 2016a; Ruszkowski et al. 2017) show energetic jets. However, the energy of the bubble depends also on the expulsion timescale of the lobe from the jet. The details of this will be modeled in future simulations.

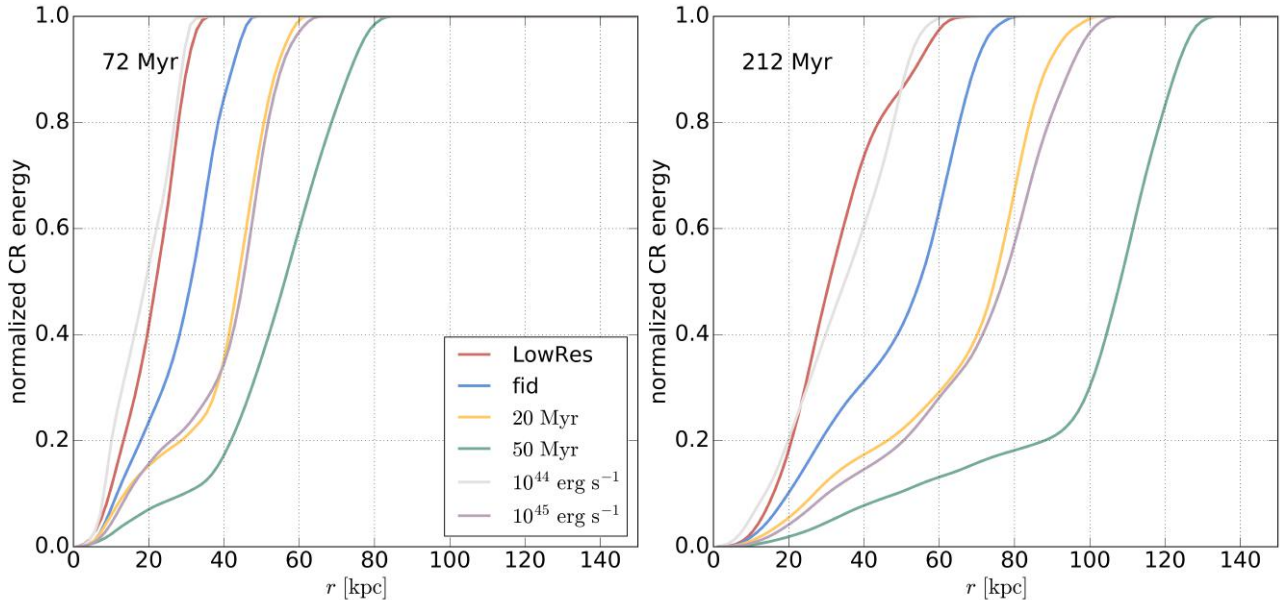

Figure 4.27: The cumulative, normalized sum of the CR energy in the indicated runs at times 72 Myr (left) and 212 Myr (right). The profiles are normalized to the total CR energy present at the respective time in the individual runs.

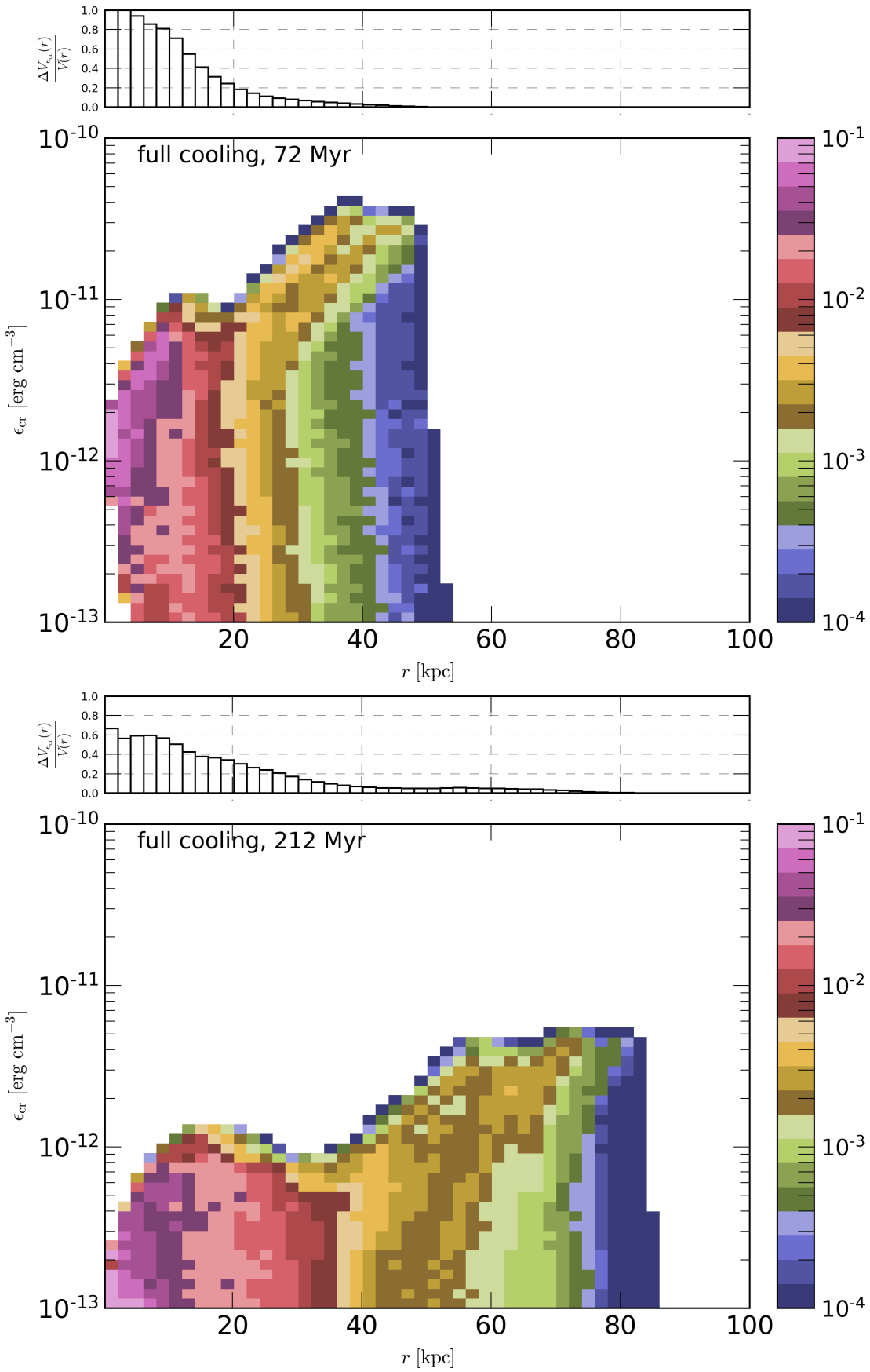

Figure 4.28: Phase diagram of the CR energy density $\epsilon_{\rm cr}$ of the fiducial run including full CR cooling at 72 Myr (top) and 240 Myr (bottom). The volume fraction covered by a radial bin of CR energy density, $V_{\rm cr}(r)$, is normalized by the total volume of the spherical shell that contains the radial bin, $V(r)$. Summing over the volume faction in each radial bin yields the histograms at the top.

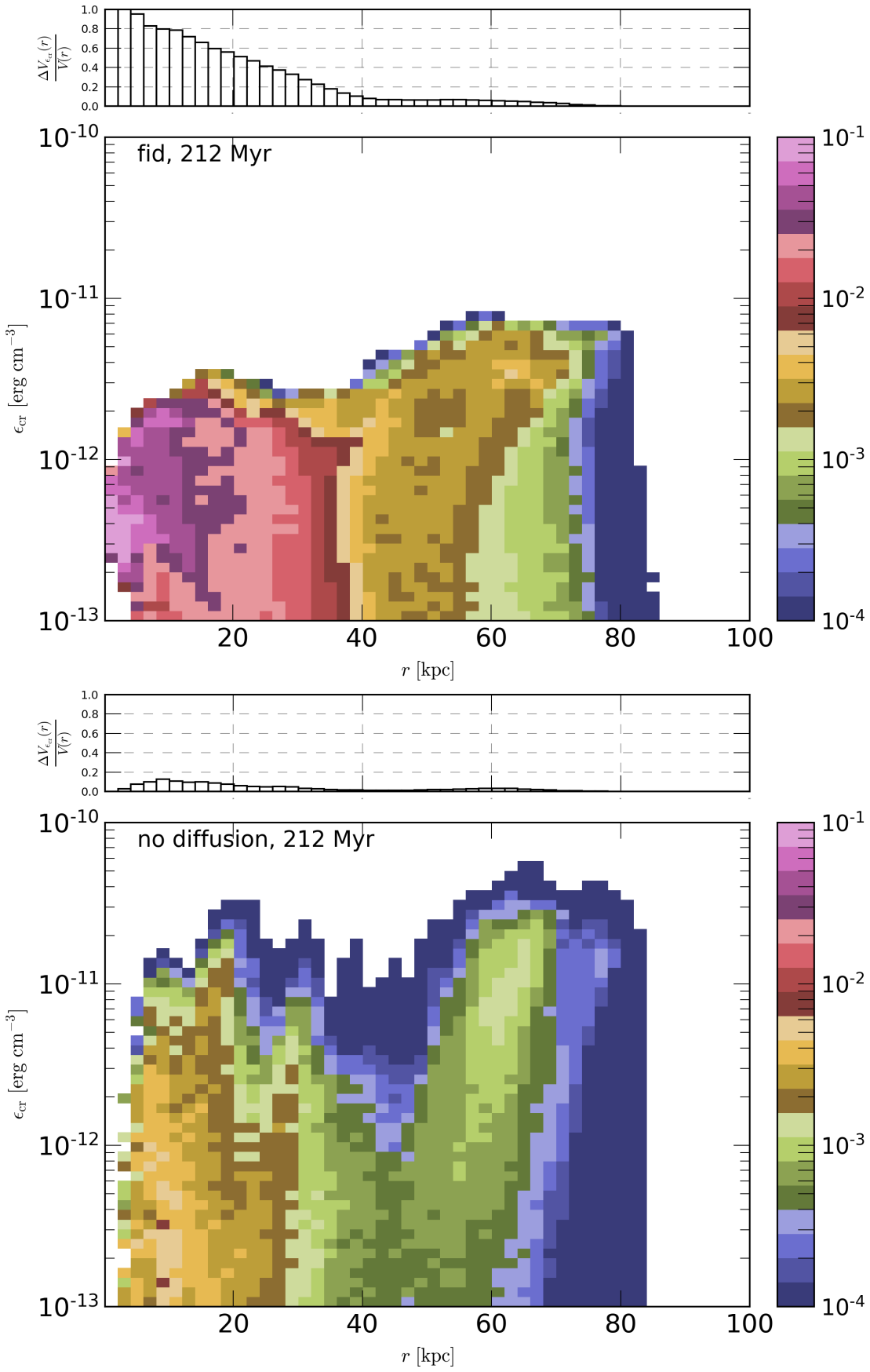

Figure 4.29: Same as Figure 4.28 for the fiducial run and the fiducial run without CR diffusion.

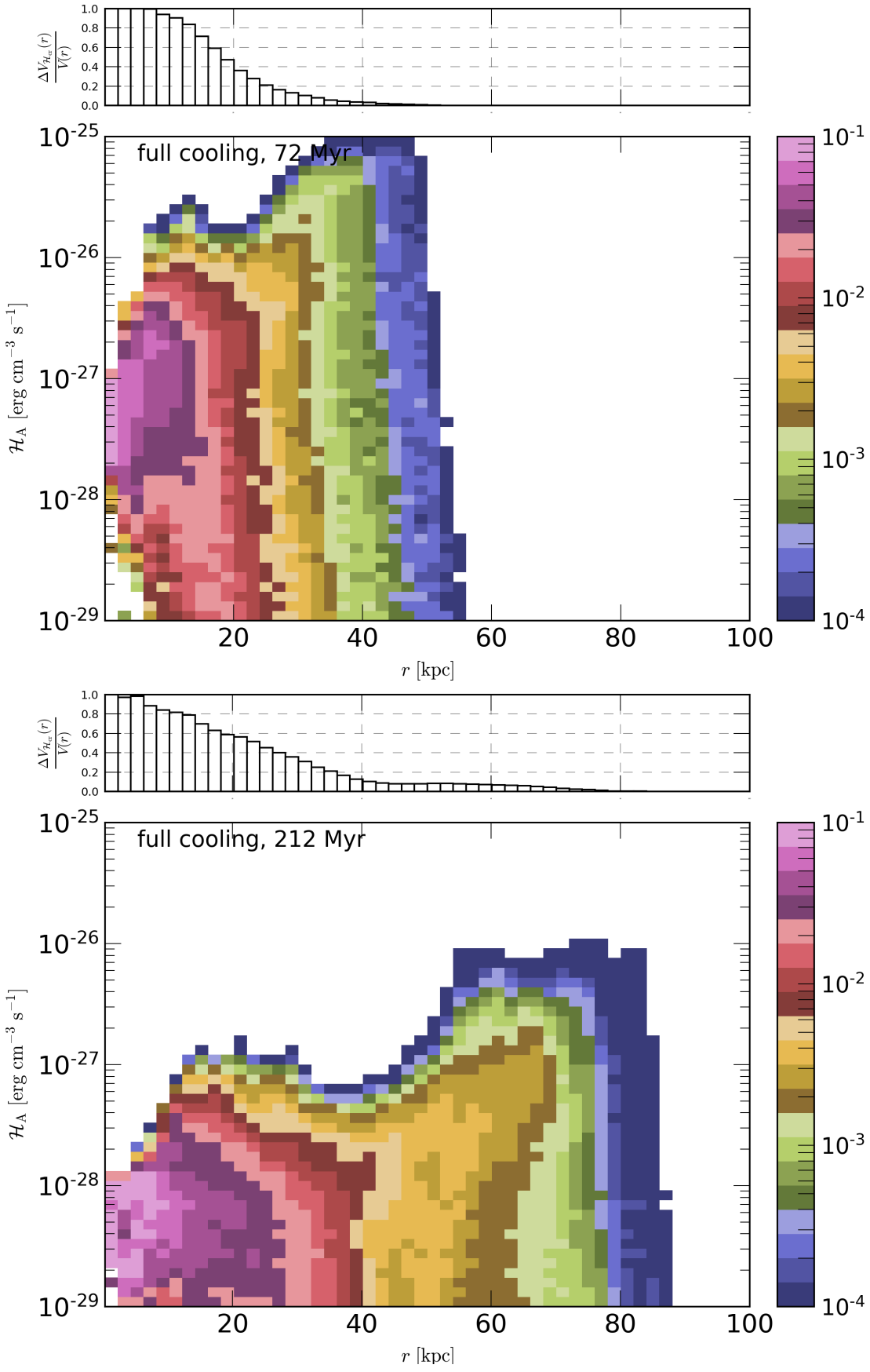

Figure 4.30: Same as Figure 4.28 for the instantaneous Alfvén heating rate.

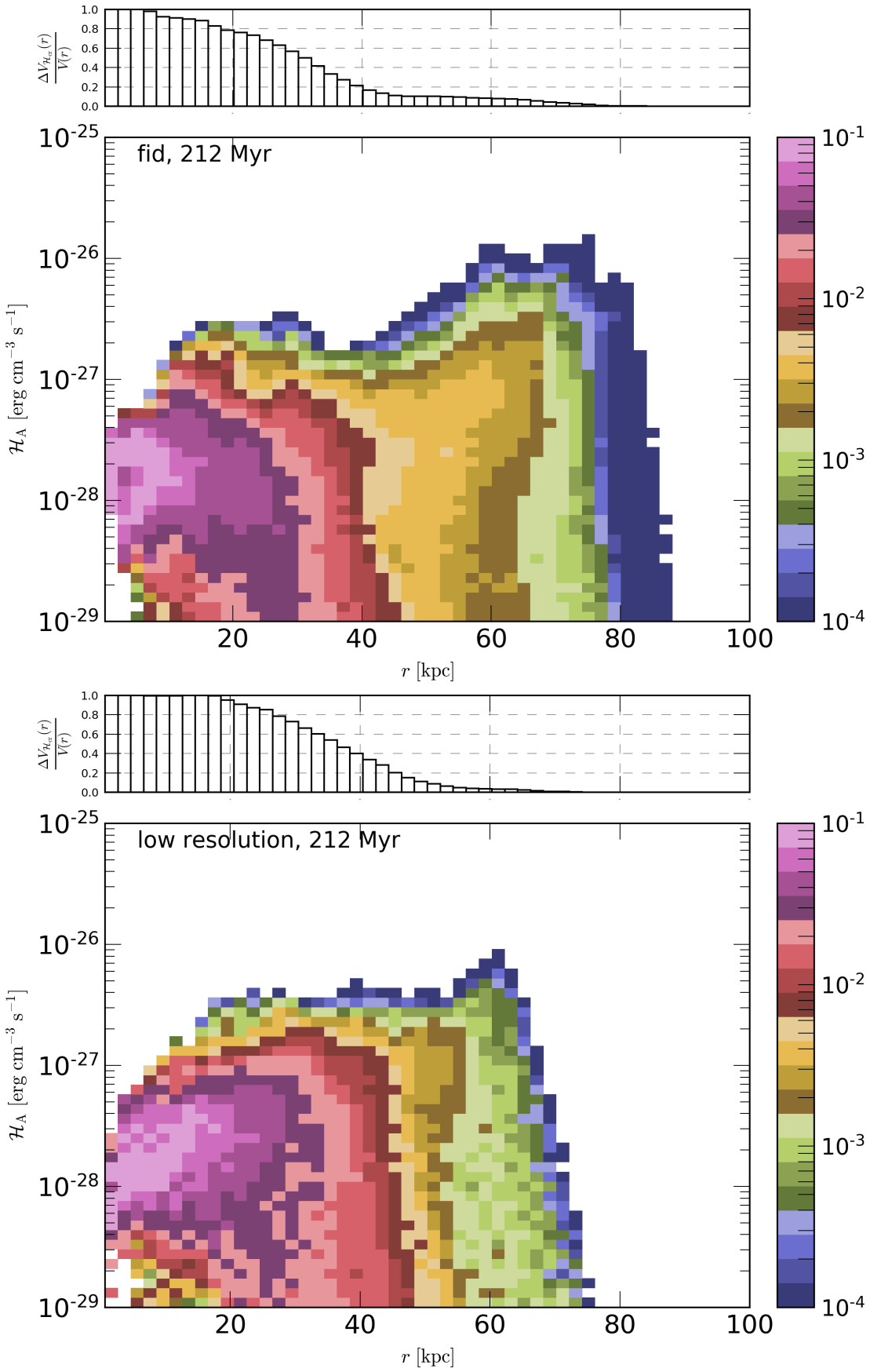

Figure 4.31: Same as Figure 4.30 for the fiducial run and a low resolution run with fiducial parameters.

5 Conclusion

A promising heating mechanism for CC clusters is the dissipation of Alfvén waves, which are excited by streaming CRs. In this picture, CRs originate from lobes that are inflated by relativistic jets from the central galactic nuclei. Here, we study the evolution of these bubbles and their effect on the cluster atmosphere with numerical simulations. This allows us to constrain models of cluster heating in general and specifically, it enables us to study the resulting three-dimensional distribution of CRs in the Alfvén wave-heating model.

In this thesis, we assisted in the development of a jet module that allows us to self-consistently inflate bubbles and study their interaction with the ICM. The presence of turbulent cluster magnetic fields changes the bubble evolution and proves critical for estimating realistic heating rate. To this end, we create a Gaussian-distributed magnetic field on a nested mesh in order to model a magnetized, turbulent cluster atmosphere. We analyze runs with varying magnetic field strength, degree of lobe magnetization, jet power and duration of jet activity and find the following main results.

After a jet-inflated lobe detaches from its source, it rises buoyantly in the cluster atmosphere. This causes an under-pressured wake, which accelerates gas towards it. As this flow focuses past the bubble, it acquires vorticity, moves up again, overshoots and pierces through the bottom of the bubble. We show that the bubble fragmentation timescale increases for nonzero cluster magnetic field strengths. This is explained by magnetic draping around the rising bubble. The magnetic draping layer provides stabilizing magnetic tension against these Rayleigh-Taylor instabilities. Kelvin-Helmholtz instabilities are additionally suppressed in magnetized clusters, which impedes mixing. On the other hand, we demonstrate that turbulent environments enhance mixing in comparison to a quiet atmosphere.

As expected, we find that the jet energy determines the evolution of the jet while the exact jet time of activity and jet power are only secondary parameters. Numerical resolution determines how far bubbles propagate in the atmosphere. Lowering the resolution broadens the jet width that is required to resolve the velocity gradient. This causes the jet momentum to be distributed over a larger area. Consequently, the jet encounters a larger ram pressure and slows down faster.

We show that adiabatic compression and possibly a dynamical dynamo enhance magnetic field strengths in the wake of the bubbles. The degree of enhancement is larger for more energetic jets, which reach larger distances from the cluster center. Consequently, they induce stronger back flows in their wake.

CR diffusion is crucial for transporting the CRs from the bubble into the central ICM. We find relatively isotropic CR distributions in the cluster core for low-luminosity jets while the degree of isotropy decreases with increasing jet luminosity. For purely advected cosmic rays, the effects of bubble fragmentation and consecutive mixing yields insufficient volume covering fractions for CR heating to offset radiative gas cooling after one outburst. Jet energy rather than degree of magnetization is found to be the important parameter that governs the distribution of CRs. More energetic jets reduce the CR escape time, which is further modulated by the diffusion coefficient.

CR cooling alters this picture as it decreases the isotropy and the overall normalization of the CR heating rate. The magnetic field amplification and the high CR gradient in the wake of the bubbles translate to efficient CR heating, which thus decreases CR energy adiabatically at a fast rate.

In the future, we will study the origin of the magnetic field amplifications in more detail, especially with regard to the correlation between magnetic and jet energy. Finally, by applying our findings to simulation with radiative gas cooling we will study whether CR Alfvén-wave heating is a viable and locally stable mechanism for self-regulated systems and thus successful in quenching cluster cooling flows.

Part I

Appendix

A Additional Figures

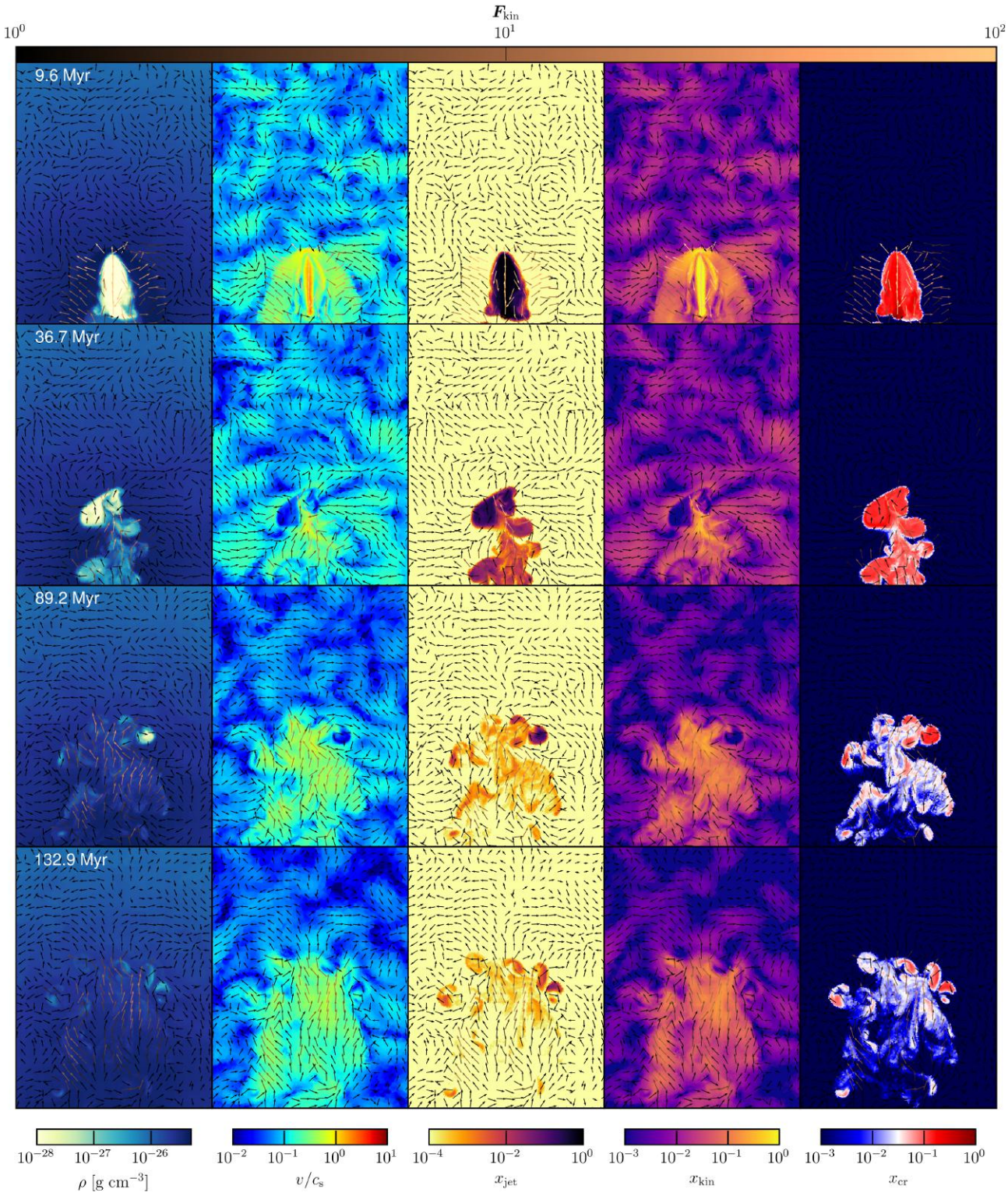

Figure A.1: The density ρ, velocity in units of sound speed v/c_s, jet mass fraction $x_{\rm jet}$, kinetic-to-thermal pressure ratio $x_{\rm kin}$ and CR-to-thermal pressure ratio $x_{\rm cr}$ are portrayed of the fiducial run without MHD. The images correspond to thin 80 kpc $-$ 60 kpc $-$ 2 kpc projections weighted with the jet tracer mass fraction to highlight the features of the jet centered at $(40, 0, 0)$. The arrows show the kinetic energy flux $\boldsymbol{F}_{\rm kin}$ where arrow length and color are scaled logarithmically with respect to the absolute value $|\boldsymbol{F}_{\rm kin}|_{x,z}$ in the $x-z$ plane that is shown. The color scales are fixed for different times shown, respectively.

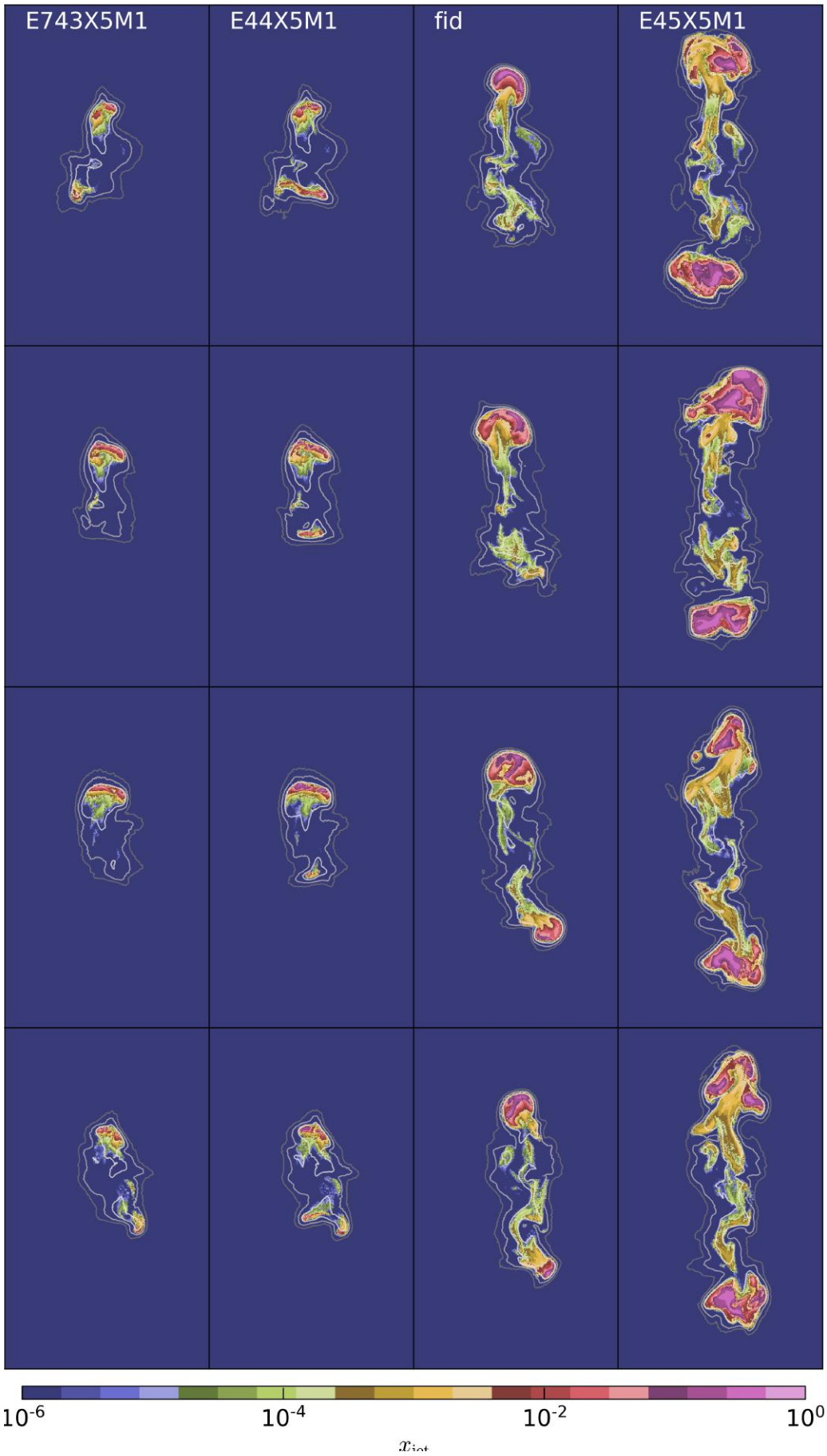

Figure A.2: The jet mass fraction $x_{\rm jet}$ is shown for simulations with varying jet power at 80.5 Myr. Contours represent the CR energy density from dark to light $10^{-13} - 10^{-12} - 10^{-11}$ erg cm^{-3}. Thin projections of the background and the contours have dimensions 160kpc – 96kpc – 4kpc, which are weighted with the jet mass and the volume, respectively. The simulations are rotated by $\pi/4$ around the vertical axis from top to bottom.

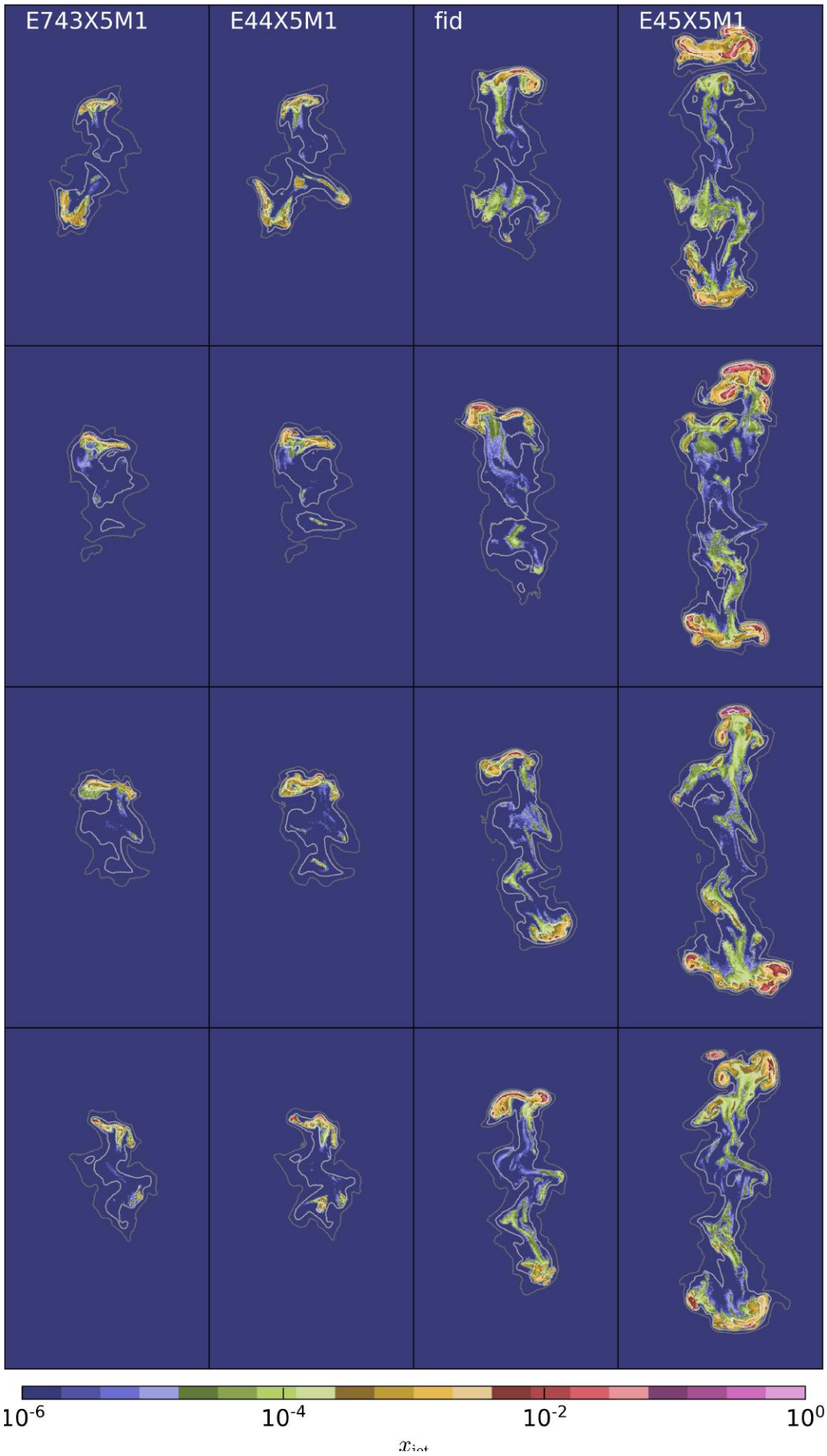

Figure A.3: Same as Figure A.2 at 185.4 Myr. Here, the projections of the background and the contours have dimensions 220kpc − 132kpc − 4kpc.

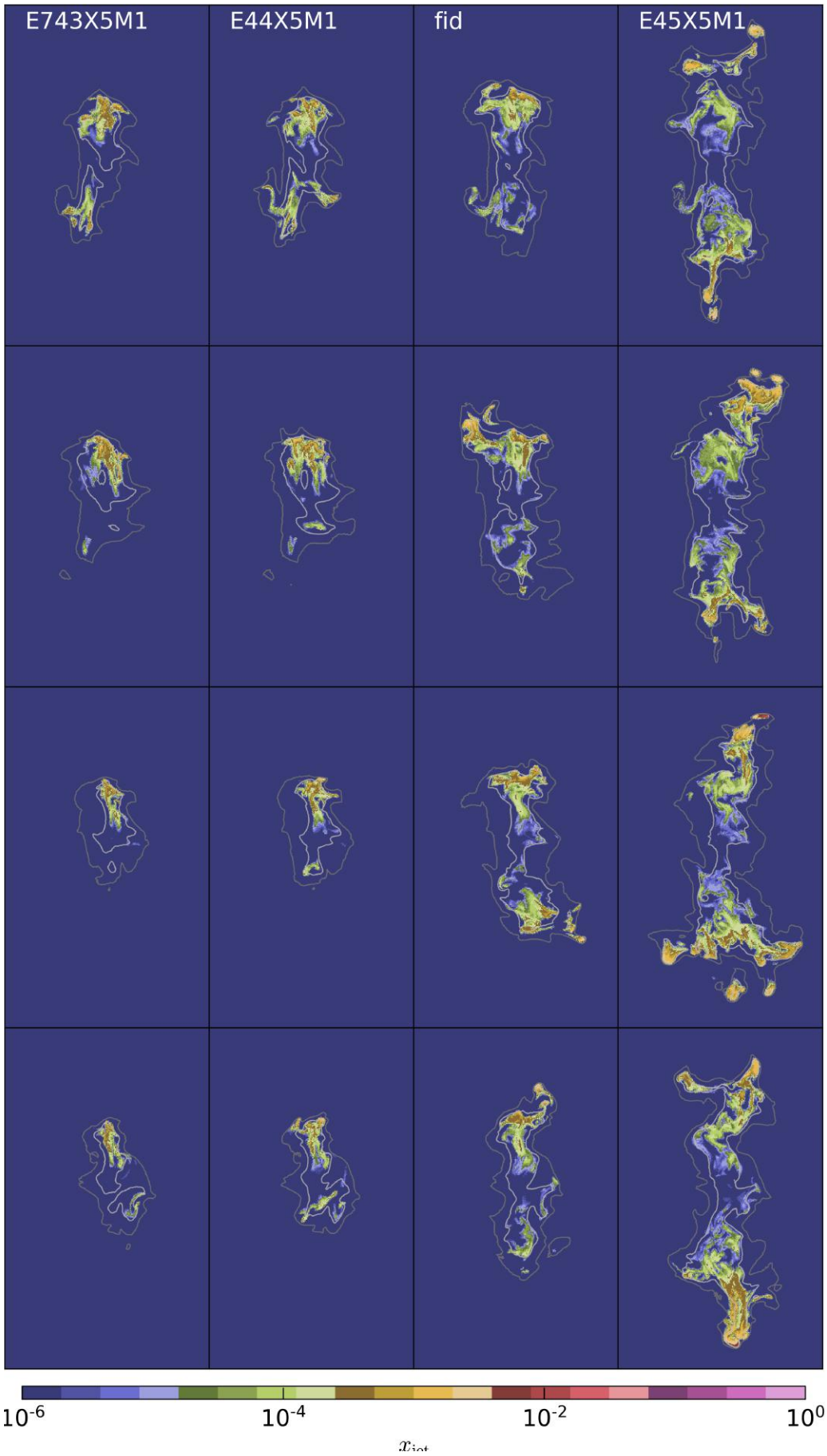

Figure A.4: Same as Figure A.2 at 422.4 Myr. Here, the projections of the background and the contours have dimensions 300kpc − 180kpc − 4kpc.

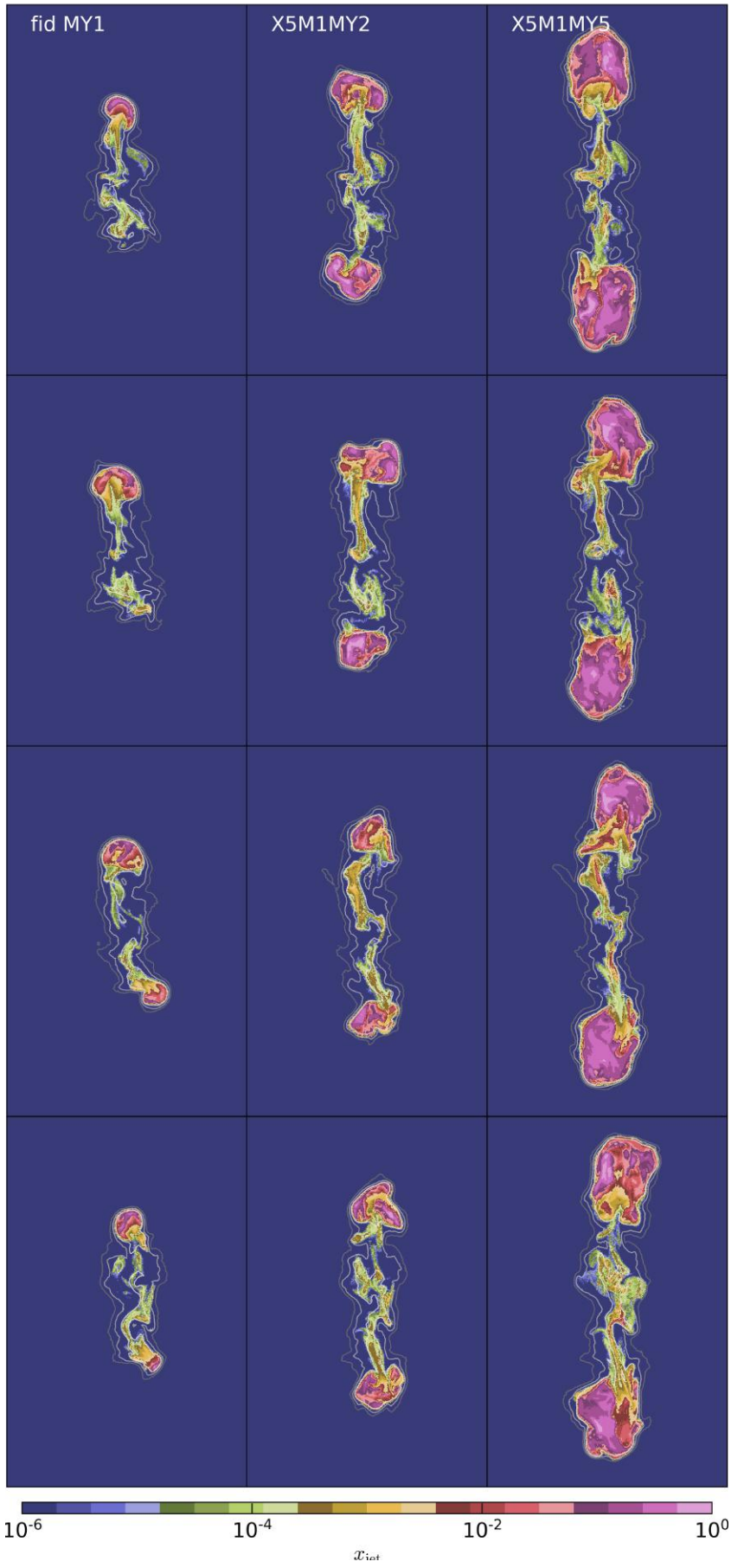

Figure A.5: The jet mass fraction $x_{\rm jet}$ is shown for simulations with varying jet activity at 80.5 Myr. Contours represent the CR energy density from dark to light $10^{-13} - 10^{-12} - 10^{-11}$ erg cm^{-3}. Thin projections of the background and the contours have dimensions 200kpc $-$ 130kpc $-$ 4kpc, which are weighted with the jet mass and the volume, respectively. The simulations are rotated by $\pi/4$ around the vertical axis from top to bottom.

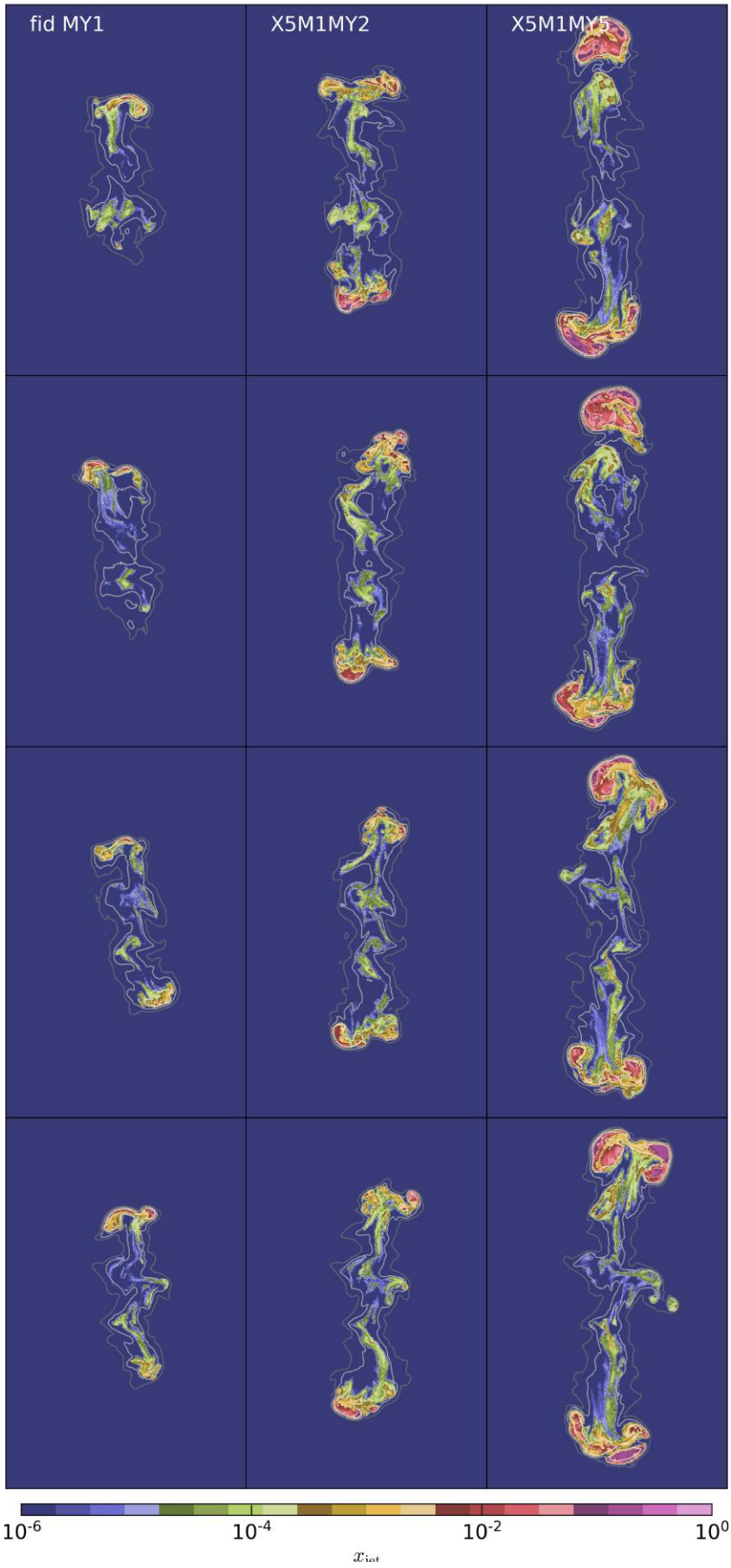

Figure A.6: Same as Figure A.5 at 185.4 Myr. Here, the projections of the background and the contours have dimensions 270kpc − 175.5kpc − 4kpc.

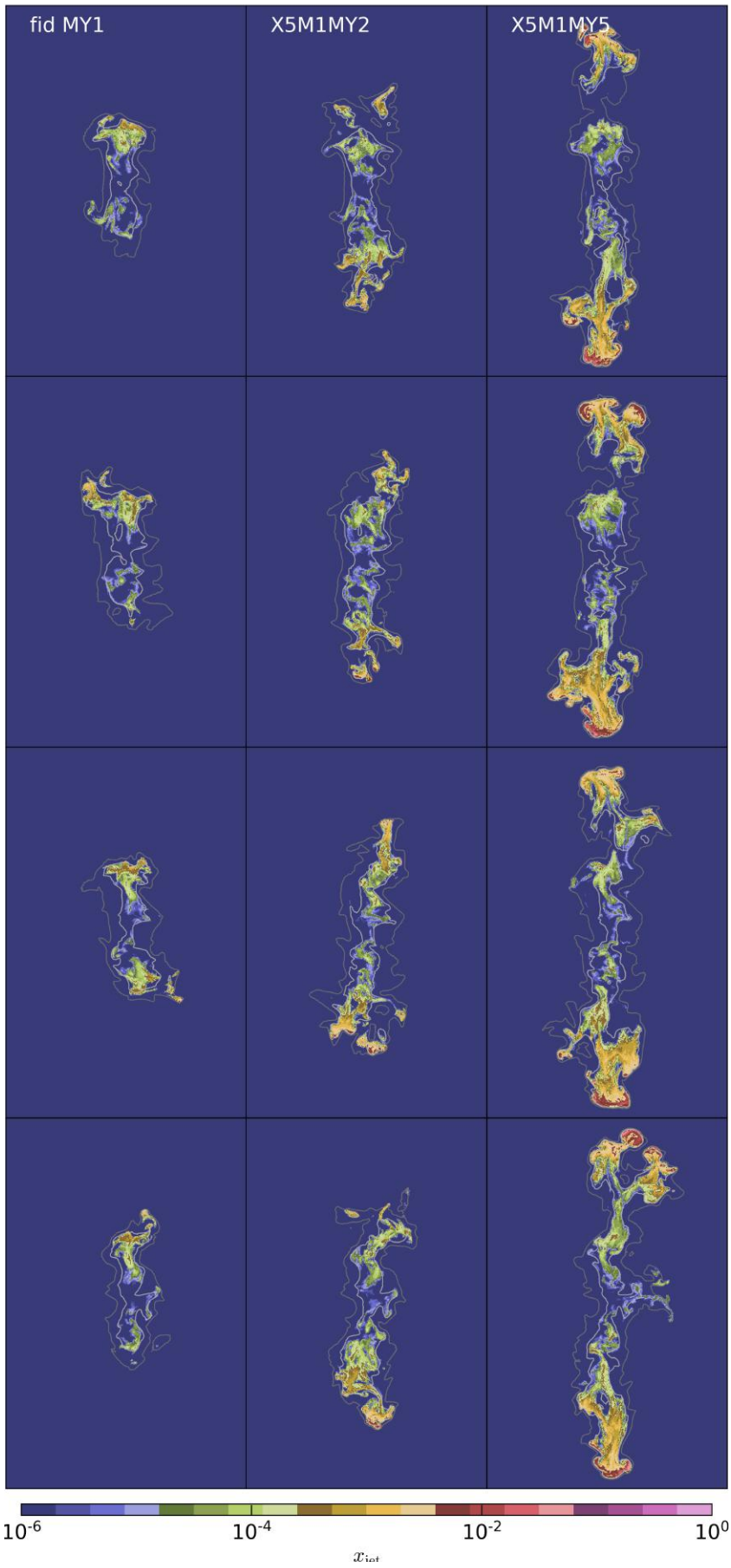

Figure A.7: Same as Figure A.5 at 422.4 Myr. Here, the projections of the background and the contours have dimensions 400kpc − 260kpc − 4kpc.

B Bibliography

Abdo, A.A. et al: 2010, *Science* **328(5979)**, 725

Allen, S.W. et al: 2006, *Mon. Not. R. Astron. Soc.* **372(1)**, 21

Allen, S.W. and Fabian, A.C.: 1998, *Mon. Not. R. Astron. Soc.* **297(3)**, L63

Asai, N., Fukuda, N. and Matsumoto, R.: 2005, *Adv. Sp. Res.* **36(4)**, 636

Asai, N., Fukuda, N. and Matsumoto, R.: 2007, *Astrophys. J.* **663(2)**, 816

Ascasibar, Y. and Markevitch, M.: 2006, *Astrophys. J.* **650(1)**, 102

Bagchi, J. et al: 2006, *Science* **314(5800)**, 791

Battaner, E. and Lesch, H.: 2000, *An. Física* **94(1)**, 213

Baym, G., Bödeker, D. and McLerran, L.: 1996, *Phys. Rev. D* **53(2)**, 662

Belsole, E. et al: 2001, *Astron. Astrophys.* **365(1)**, L188

Berezinskii, V.S. et al: 1990, *Astrophysics of cosmic rays*, North-Holland, Amsterdam

Bhattacharyya, W. and Gupta, N.: 2016, *Astrophys. J.* **817(2)**, 121

Bicknell, G.V.: 1994, *Astrophys. J.* **422(2)**, 542

Biermann, L. and Schlüter, A.: 1950, *Zeitschrift fur Naturforsch. - Sect. A J. Phys. Sci.* **5(2)**, 65

Bîrzan, L. et al: 2008, *Astrophys. J.* **686(2)**, 859

Bîrzan, L. et al: 2004, *Astrophys. J.* **607(2)**, 800

Blandford, R.D. and Payne, D.G.: 1982, *Mon. Not. R. Astron. Soc.* **199(4)**, 883

Blandford, R.D. and Znajek, R.L.: 1977, *Mon. Not. R. astr. Soc* **179**, 433

Blanton, E.L. et al: 2010, *Proc. Natl. Acad. Sci. U. S. A.* **107(16)**, 7174

Blanton, E.L. et al: 2009, *Astrophys. J.* **697(2)**, L95

Blanton, E.L., Sarazin, C.L. and McNamara, B.R.: 2003, *Astrophys. J.* **585(1)**, 227

Blanton, E.L. et al: 2004, *Astrophys. J.* **612(2)**, 817

Blanton, E.L. et al: 2001, *Astrophys. J.* **558(1)**, L15

Blundell, K.M. et al: 2006, *Astrophys. J.* **644(1)**, L13

Böhringer, H. et al: 2001, *Astron. Astrophys.* **365**, 181

Bonafede, A. et al: 2010, *Astron. Astrophys.* **513**, A30

Bourne, M.A. and Sijacki, D.: 2017, *preprint, (arXiv:1705.07900)*

Bravi, L., Gitti, M. and Brunetti, G.: 2016, *Mon. Not. R. Astron. Soc. Lett.* **455(1)**, L41

Bridle, A.H.: 1984, *Annu. Rev. Astron. Astrophys.* **22**, 319

Brüggen, M. et al: 2012, *Space Sci. Rev.* **166(1)**, 187

Brüggen, M., van Weeren, R.J. and Rottgering, H.J.a.: 2011, *Mem. della Soc. Astron. Ital.* **82**, 627

Brunetti, G. and Jones, T.W.: 2014, *Int. J. Mod. Phys. D* **23(4)**, 30007

Brunetti, G. and Lazarian, A.: 2011, *Mon. Not. R. Astron. Soc.* **410(1)**, 127

Burns, J.O.: 1990, *Astron. J.* **99(1)**, 14

Caprioli, D. and Spitkovsky, A.: 2014, *Astrophys. J.* **794(1)**, 46

Carilli, C.L. and Taylor, G.B.: 2002, *Annu. Rev. Astron. Astrophys.* **40(1)**, 319

Cassano, R. et al: 2010, *Astrophys. J.* **721(2)**, L82

Cassano, R., Gitti, M. and Brunetti, G.: 2008, *Astron. Astrophys.* **486(3)**, L31

Celotti, A., Ghisellini, G. and Chiaberge, M.: 2001, *Mon. Not. R. Astron. Soc.* **321(1)**, L1

Chandrasekhar, S.: 1981, *Hydrodynamic and Hydromagnetic Stability*, Dover, New York

Chen, H. et al: 2017, *Astrophys. J.* **838(1)**, 38

Churazov, E. et al: 2001, *Astrophys. J.* **554(1)**, 261

Churazov, E. et al: 2003, *Astrophys. J.* **590(1)**, 225

Clarke, T.E. et al: 2009, *Astrophys. J.* **697(2)**, 1481

Clarke, T.E., Kronberg, P.P. and Böhringer, H.: 2001, *Astrophys. J.* **547(2)**, L111

Clarke, T.E. et al: 2005, *Astrophys. J.* **625(2)**, 748

Cooley, J.W. and Tukey, J.W.: 1965, *Math. Comput.* **19(90)**, 297

Croston, J.H.: 2008, in *Extragalactic Jets Theory Obs. from Radio to Gamma Ray ASP Conf. Ser.*, pp 335–342, Astronomical Society of the Pacific, San Francisco

Croston, J.H. and Hardcastle, M.J.: 2014, *Mon. Not. R. Astron. Soc.* **438(4)**, 3310

Croston, J.H. et al: 2003, *Mon. Not. R. Astron. Soc.* **346(4)**, 1041

Croston, J.H. et al: 2008, *Mon. Not. R. Astron. Soc.* **386(3)**, 1709

Croston, J.H., Kraft, R.P. and Hardcastle, M.J.: 2007, *Astrophys. J.* **660(1)**, 191

David, L.P. et al: 2001, *Astrophys. J.* **557(2)**, 546

De Grandi, S. et al: 2004, *Astron. Astrophys.* **419(1)**, 7

De Young, D.S.: 2006, *Astrophys. J.* **648(1)**, 200

Diehl, S. et al: 2008, *Astrophys. J.* **687(1)**, 173

Dunn, R.J.H. and Fabian, A.C.: 2006, *Mon. Not. R. Astron. Soc.* **373(3)**, 959

Dunn, R.J.H., Fabian, A.C. and Sanders, J.S.: 2006, *Mon. Not. R. Astron. Soc.* **366(3)**, 758

Dunn, R.J.H., Fabian, A.C. and Taylor, G.B.: 2005, *Mon. Not. R. Astron. Soc.* **364(4)**, 1343

Dursi, L.J. and Pfrommer, C.: 2008, *Astrophys. J.* **677(2)**, 993

Enßlin, T. et al: 2011, *Astron. Astrophys.* **527**, A99

Enßlin, T.A. and Brüggen, M.: 2001, in *Clust. galaxies high redshift universe Obs. X-rays, Recent results Xmm-newt. Chandra, XXXVIth Rencontres Moriond , XXIst Moriond Astrophys. Meet.*, Savoie

Enßlin, T.A. and Gopal-Krishna: 2001, *Astron. Astrophys* **366**, 26

Enßlin, T.A. et al: 2007, *Astron. Astrophys.* **473(1)**, 41

Enßlin, T.A., Vogt, C. and Pfrommer, C.: 2005, in *Magn. Plasma Galaxy Evol.*, pp 231–238, Jagiellonian University, Kraków, Poland

Evans, C.R. and Hawley, J.F.: 1988, *Astrophys. J.* **332(2)**, 659

Fabian, A.C. et al: 2003a, *Mon. Not. R. Astron. Soc.* **344(3)**, L43

Fabian, A.C. et al: 2003b, *Mon. Not. R. Astron. Soc.* **344(3)**, 48

Fabian, A.C. et al: 2000, *Mon. Not. R. Astron. Soc.* **318(4)**, L65

Fabian, A.C. et al: 2006, *Mon. Not. R. Astron. Soc.* **366(2)**, 417

Fabian, A.C. et al: 2017, *Mon. Not. R. Astron. Soc.* **464(1)**, L1

Fanaroff, B.L. and Riley, J.M.: 1974, *Mon. Not. R. Astron. Soc.* **167(1)**, 31P

Farmer, A.J. and Goldreich, P.: 2004, *Astrophys. J.* **604(2)**, 671

Feretti, L. et al: 2006, *Mon. Not. R. Astron. Soc.* **368(2)**, 544

Feretti, L. et al: 2010, *Highlights Astron.* **15**, 459

Feretti, L. et al: 1995, *Astron. Astrophys.* **298**, 699

Feretti, L. et al: 2001, *Astron. Astrophys.* **373**, 106

Feretti, L. et al: 2012, *Astron. Astrophys. Rev.* **20**, 54F

Feretti, L. et al: 2004, *Astron. Astrophys.* **423**, 111

Fermi, E.: 1949, *Phys. Rev.* **75(8)**, 1169

Finoguenov, A. et al: 2010, *Astrophys. J.* **715(2)**, 1143

Fletcher, A.: 2010, in *Dyn. Interstellar Mediu. A Celebr. Can. Galact. Pl. Surv.*, p. 197, Astronomical Society of the Pacific, San Francisco

Forman, W. et al: 2007, *Astrophys. J.* **665(2)**, 1057

Forman, W. et al: 2005, *Astrophys. J.* **635(2)**, 894

Fujita, Y. and Ohira, Y.: 2013, *Mon. Not. R. Astron. Soc.* **428(1)**, 599

Gaspari, M., Ruszkowski, M. and Sharma, P.: 2012, *Astrophys. J.* **746(1)**, 94

Giacintucci, S. et al: 2014a, *Astrophys. J.* **795(1)**, 73

Giacintucci, S. et al: 2017, *Astrophys. J.* **841(2)**, 71

Giacintucci, S. et al: 2014b, *Astrophys. J.* **781(1)**, 9

Giacintucci, S. et al: 2005, *Astron. Astrophys.* **440(3)**, 867

Gilkis, A. and Soker, N.: 2012, *Mon. Not. R. Astron. Soc.* **427(2)**, 1482

Giovannini, G. et al: 2009, *Astron. Astrophys.* **507(3)**, 1257

Giovannini, G. et al: 2011, *Astron. Astrophys.* **530**, L5

Gitti, M. et al: 2007, *Astrophys. J.* **660(2)**, 1118

Gitti, M. et al: 2011, *Astrophys. J.* **732(1)**, 13

Gnedin, N.Y., Ferrara, A. and Zweibel, E.G.: 2000, *Astrophys. J.* **539(2)**, 505

Godfrey, L. et al: 2009, *Astrophys. J.* **695(1)**, 707

Goldreich, P. and Sridhar, S.: 1995, *Astrophys. J.* **438(2)**, 763

Gould, R.J.: 1972, *Physica* **58(3)**, 379

Govoni, F. and Feretti, L.: 2004, *Int. J. Mod. Phys. D* **13(8)**, 1549

Govoni, F. et al: 2001, *Astron. Astrophys.* **376(3)**, 803

Govoni, F. et al: 2009, *Astron. Astrophys.* **499(2)**, 371

Grasso, D. and Rubinstein, H.R.: 2000, *Phys. Rep.* **348(3)**, 163

Guo, F.: 2015, *Astrophys. J.* **803(1)**, 48

Guo, F., Duan, X. and Yuan, Y.F.: 2017, *preprint, (arXiv:1705.10916)*

Guo, F. and Oh, S.P.: 2008, *Mon. Not. R. Astron. Soc.* **384(1)**, 251

Hardcastle, M.J. et al: 2002, *Astrophys. J.* **581(2)**, 948

Hardcastle, M.J. and Croston, J.H.: 2005, *Mon. Not. R. Astron. Soc.* **363(2)**, 649

Hardcastle, M.J., Croston, J.H. and Kraft, R.P.: 2007a, *Astrophys. J.* **669(2)**, 893

Hardcastle, M.J. et al: 2007b, *Astrophys. J.* **670(2)**, L81

Hardcastle, M.J., Kraft, R.P. and Worrall, D.M.: 2006, *Mon. Not. R. Astron. Soc. Lett.* **368(1)**, 15

Hardcastle, M.J. and Krause, M.G.H.: 2014, *Mon. Not. R. Astron. Soc.* **443(2)**, 1482

Hardcastle, M.J. et al: 2003, *Astrophys. J.* **593(1)**, 169

Harris, D. and Krawczynski, H.: 2006, *Annu. Rev. Astron. Astrophys.* **44**, 463

Hawley, J.F. et al: 2015, *Space Sci. Rev.* **191(1-4)**, 441

Heinz, S. and Churazov, E.: 2005, *Astrophys. J.* **634(1)**, 141

Hillel, S. and Soker, N.: 2016, *Mon. Not. R. Astron. Soc.* **455(2)**, 2139

Hitomi Collaboration et al: 2016, *Nature* **535**, 117

Hoffer, A.S. et al: 2012, *Astrophys. J. Suppl. Ser.* **199(1)**, 23

Isobe, N. et al: 2002, *Astrophys. J.* **580(2)**, L111

Jacob, S.: 2015, *Master thesis*, University of Heidelberg

Jacob, S. and Pfrommer, C.: 2017a, *Mon. Not. R. Astron. Soc.* **467(2)**, 1449

Jacob, S. and Pfrommer, C.: 2017b, *Mon. Not. R. Astron. Soc.* **467(2)**, 1478

Johnston-Hollitt, M.: 2003, *Ph.D. thesis*, University of Adelaide

Kale, R. et al: 2015, *Astron. Astrophys.* **579**, A92

Kannan, R. et al: 2016, *Astrophys. J. Lett.* **837(2)**, 1

Kataoka, J.: 2005, *Astrophys. J.* **622(2)**, 797

Kempner, J.C. et al: 2004, in *Proc. Riddle Cool. Flows Galaxies Clust. Galaxies*, University of Virginia, Charlottesville

Kennel, C.F. and Engelmann, F.: 1966, *Phys. Fluids* **9**, 2377

King, A.R. and Pringle, J.E.: 2007, *Mon. Not. R. Astron. Soc. Lett.* **377(1)**, L25

Kirkpatrick, C.C. et al: 2009, *Astrophys. J.* **707(1)**, L69

Kirkpatrick, C.C. and McNamara, B.R.: 2015, *Mon. Not. R. Astron. Soc.* **452(4)**, 4361

Kirkpatrick, C.C., McNamara, B.R. and Cavagnolo, K.W.: 2011, *Astrophys. J.* **731(2)**, L23

Kokotanekov, G. et al: 2017, *preprint, (arXiv:1706.00225)*

Komarov, S.V. et al: 2016, *Mon. Not. R. Astron. Soc.* **460(1)**, 467

Kraft, R.P. et al: 2003, *Astrophys. J.* **592(1)**, 129

Kronberg, P.P.: 2003, in *Matter Energy Clust. Galaxies*, Vol. 301, pp 169–183, Astronomical Society of the Pacific, Chung-Li, Taiwan

Kuchar, P. and Enßlin, T.A.: 2011, *Astron. Astrophys.* **529(A13)**, 13

Kulsrud, R. and Pearce, W.P.: 1969, *Astrophys. J.* **156**, 445

Kulsrud, R.M.: 2005, *Plasma Physics for Astrophysics*, Princeton University Press, Princeton, NJ

Kulsrud, R.M. et al: 1997, *Astrophys. J.* **480(2)**, 481

Kulsrud, R.M. and Cesarsky, C.J.: 1971, *Astrophys. Lett.* **8**, 189

Laing, R.A.: 1980, *Mon. Not. R. Astron. Soc.* **193**, 439

Laing, R.A. and Bridle, A.H.: 2014, *Mon. Not. R. Astron. Soc.* **437(4)**, 3405

Ledlow, M.J. and Owen, F.N.: 1996, *Astron. J.* **112(1)**, 9

Lee, M.A. and Völk, H.J.: 1973, *Astrophys. Space Sci.* **24(1)**, 31

Li, H. et al: 2006, *Astrophys. J.* **643(1)**, 92

Li, Y. et al: 2015, *Astrophys. J.* **811(2)**, 73

Li, Y., Ruszkowski, M. and Bryan, G.L.: 2016, *preprint, (arXiv:1611.05455)*

Lind, K.R. et al: 1989, *Astrophys. J.* **344**, 89

Liu, R.Y., Rieger, F.M. and Aharonian, F.A.: 2017, *Astron. J.* **842(1)**, 39

Loewenstein, M., Zweibel, E.G. and Begelman, M.C.: 1991, *Astrophys. J.* **377**, 392

Lucchini, M., Tavecchio, F. and Ghisellini, G.: 2017, *Mon. Not. R. Astron. Soc.* **466(4)**, 4299

Lyutikov, M.: 2006, *Mon. Not. R. Astron. Soc.* **373(1)**, 73

Mannheim, K. and Schlickeiser, R.: 1994, *Astron. Astrophys* **286**, 983

Marcowith, A. et al: 2016, *Reports Prog. Phys.* **79(4)**, 046901

Markevitch, M. and Vikhlinin, A.: 2007, *Phys. Rep.* **443(1)**, 1

Mathews, W.G. and Brighenti, F.: 2008, *Astrophys. J.* **676(2)**, 880

Mathews, W.G., Faltenbacher, A. and Brighenti, F.: 2006, *Astrophys. J.* **638(2)**, 659

Mazzotta, P. and Giacintucci, S.: 2008, *Astrophys. J.* **675**, L9

McNamara, B.: 1997, in *Galact. Clust. Cool. Flows*, Vol. 115, p. 109, Oranim, Israel

McNamara, B. and Nulsen, P.: 2007, *Annu. Rev. Astron. Astrophys.* **45(1)**, 117

McNamara, B.R. and Nulsen, P.E.J.: 2012, *New J. Phys.* **14**, 40

McNamara, B.R. et al: 2005, *Nature* **433(7021)**, 45

McNamara, B.R. et al: 2000, *Astrophys. J.* **534(2)**, L135

McNamara, B.R. et al: 2001, *Astrophys. J.* **562(2)**, L149

Meyer, E.T. et al: 2017, *Astrophys. J. Lett.* **835(2)**, 1

Migliori, G. et al: 2007, *Astrophys. J.* **668**, 203

Mittal, R. et al: 2009, *Astron. Astrophys.* **501(3)**, 835

Miyoshi, T. and Kusano, K.: 2005, *J. Comput. Phys.* **208(1)**, 315

Morganti, R. et al: 1988, *Astron. Astrophys.* **189(1-2)**, 11

Morsony, B.J. et al: 2010, *Mon. Not. R. Astron. Soc.* **407(2)**, 1277

Murgia, M. et al: 2012, *Astron. Astrophys.* **548**, A75

Murgia, M. et al: 2011, *Astron. Astrophys.* **526**, A148

Narayan, R. and Medvedev, M.V.: 2001, *Astrophys. J.* **562(2)**, L129

Navarro, J.F., Frenk, C.S. and White, S.D.M.: 1996, *Astrophys. J.* **462**, 563

Navarro, J.F., Frenk, C.S. and White, S.D.M.: 1997, *Astrophys. J.* **490(2)**, 493

Nazarenko, S.V. and Schekochihin, A.A.: 2011, *J. Fluid Mech.* **677**, 134

Nulsen, P.E.J. et al: 2002, *Astrophys. J.* **568(1)**, 163

Nulsen, P.E.J. et al: 2007, *AGN heating through cavities and shocks*, Springer-Verlag, Berlin, Heidelberg

Nuza, S.E. et al: 2017, *Mon. Not. R. Astron. Soc.* **470(1)**, 240

Pakmor, R., Bauer, A. and Springel, V.: 2011, *Mon. Not. R. Astron. Soc.* **418(2)**, 1392

Pakmor, R. et al: 2016a, *Mon. Not. R. Astron. Soc.* **462(3)**, 2603

Pakmor, R. and Springel, V.: 2013, *Mon. Not. R. Astron. Soc.* **432(1)**, 176

Pakmor, R. et al: 2016b, *Mon. Not. R. Astron. Soc.* **455(1)**, 1134

Patrignani, C. et al: 2016, *Chinese Phys. C* **40(10)**, 100001

Peterson, J.R. and Fabian, A.C.: 2006, *Phys. Rep.* **427(1)**, 1

Peterson, J.R. et al: 2001, *Astron. Astrophys.* **365**, L104

Pfrommer, C.: 2013, *Astrophys. J.* **779(1)**, 10

Pfrommer, C., Chang, P. and Broderick, A.E.: 2012, *Astrophys. J.* **752(1)**, 24

Pfrommer, C. and Dursi, J.: 2010, *Nat. Phys.* **6(7)**, 520

Pfrommer, C. and Enßlin, T.A.: 2004, *Astron. Astrophys.* **413(1)**, 17

Pfrommer, C. et al: 2017, *Mon. Not. R. Astron. Soc.* **465(4)**, 4500

Pinzke, A., Oh, S.P. and Pfrommer, C.: 2013, *Mon. Not. R. Astron. Soc.* **435(2)**, 1061

Pinzke, A., Oh, S.P. and Pfrommer, C.: 2015, *preprint, (arXiv:1503.07870)*

Pizzolato, F. and Soker, N.: 2006, *Mon. Not. R. Astron. Soc.* **371(4)**, 1835

Pollack, L.K., Taylor, G.B. and Allen, S.W.: 2005, *Mon. Not. R. Astron. Soc.* **359(4)**, 1229

Powell, K.G. et al: 1999, *J. Comput. Phys.* **154(2)**, 284

Rafferty, D.A., McNamara, B.R. and Nulsen, P.E.J.: 2008, *Astrophys. J.* **687(2)**, 899

Rafferty, D.A. et al: 2006, *Astrophys. J.* **652(1)**, 216

Randall, S.W. et al: 2011, *Astrophys. J.* **726(2)**, 86

Rebusco, P. et al: 2005, *Mon. Not. R. Astron. Soc.* **359(3)**, 1041

Rephaeli, Y.: 1979, *Astrophys. J.* **227**, 364

Reynolds, C.S., Balbus, S.A. and Schekochihin, A.A.: 2015, *Astrophys. J.* **815(1)**, 41

Reynolds, C.S., Heinz, S. and Begelman, M.C.: 2002, *Mon. Not. R. Astron. Soc.* **332(2)**, 271

Reynolds, C.S. et al: 2005, *Mon. Not. R. Astron. Soc.* **357(1)**, 242

Rossetti, M. et al: 2013, *Astron. Astrophys.* **556**, A44

Rottgering, H.J.a. et al: 1997, *Mon. Not. R. Astron. Soc.* **290(4)**, 577

Russell, H.R. et al: 2011, *Mon. Not. R. Astron. Soc. Lett.* **417(1)**, L1

Ruszkowski, M. et al: 2008, *Mon. Not. R. Astron. Soc.* **383(4)**, 1359

Ruszkowski, M. et al: 2007, *Mon. Not. R. Astron. Soc.* **378(2)**, 662

Ruszkowski, M. and Oh, S.P.: 2010, *Astrophys. J.* **713(2)**, 1332

Ruszkowski, M. and Oh, S.P.: 2011, *Mon. Not. R. Astron. Soc.* **414(2)**, 1493

Ruszkowski, M., Yang, H.Y.K. and Reynolds, C.S.: 2017, *preprint, (arXiv:1701.07441)*

Rybicki, G.B. and Lightman, A.P.: 1979, *Radiative Processes in Astrophysics*, Wiley

Saikia, D.J. and Jamrozy, M.: 2009, *Bull. Astron. Soc. India* **37(3-4)**, 63

Salomé, P. et al: 2011, *Astron. Astrophys.* **531**, A85

Sanders, J.S. and Fabian, A.C.: 2008, *Mon. Not. R. Astron. Soc. Lett.* **390(1)**, L93

Sanders, J.S., Fabian, A.C. and Smith, R.K.: 2011, *Mon. Not. R. Astron. Soc.* **410(3)**, 1797

Sanders, J.S., Fabian, A.C. and Taylor, G.B.: 2009, *Mon. Not. R. Astron. Soc.* **396(3)**, 1449

Sarazin, C.L.: 1999, *Astrophys. J.* **520(2)**, 529

Schmidt, R.W., Fabian, A.C. and Sanders, J.S.: 2002, *Mon. Not. R. Astron. Soc.* **337(1)**, 71

Schuecker, P. et al: 2004, *Astron. Astrophys.* **426(2)**, 387

Schwartz, D.A. et al: 2006, *Astrophys. J.* **640(2)**, 592

Sharma, P. et al: 2009, *Astrophys. J.* **699(1)**, 348

Sharma, P., Colella, P. and Martin, D.F.: 2010, *SIAM J. Sci. Comput.* **32(6)**, 3564

Sharma, P. and Hammett, G.W.: 2007, *J. Comput. Phys.* **227(1)**, 123

Sharma, P. and Hammett, G.W.: 2011, *J. Comput. Phys.* **230(12)**, 4899

Sijacki, D. et al: 2008, *Mon. Not. R. Astron. Soc.* **387(4)**, 1403

Skilling, J.: 1971, *Astrophys. J.* **170**, 265

Skilling, J.: 1975, *Mon. Not. R. Astron. Soc.* **172**, 557

Soker, N., Blanton, E. and Sarazin, C.: 2002, *Astrophys. J.* **573(2)**, 533

Solovyeva, L. et al: 2008, *Astron. Astrophys.* **484(3)**, 621

Sommer, M.W. et al: 2017, *Mon. Not. R. Astron. Soc.* **466(1)**, 996

Springel, V.: 2010, *Mon. Not. R. Astron. Soc.* **401(2)**, 791

Strong, A.W. and Moskalenko, I.V.: 1998, *Astrophys. J.* **509(1)**, 212

Strong, A.W., Moskalenko, I.V. and Ptuskin, V.S.: 2007, *Annu. Rev. Nucl. Part. Sci.* **57(1)**, 285

Tavecchio, F. et al: 2000, *Astrophys. J.* **544(1)**, L23

Tregillis, I.L., Jones, T.W. and Ryu, D.: 2004, *Astrophys. J.* **601(2)**, 778

Turner, M.S. and Widrow, L.M.: 1988, *Phys. Rev. D* **37(10)**, 2743

Vacca, V. et al: 2010, *Astron. Astrophys.* **514**, A71

Vallée, J.P.: 2004, *New Astron. Rev.* **48(10)**, 763

van Leer, B.: 1984, *SIAM J. Sci. Stat. Comput.* **5(1)**, 1

van Weeren, R.J. et al: 2011, *Astron. Astrophys.* **533**, A35

Vikhlinin, A., Markevitch, M. and Murray, S.S.: 2001, *Astrophys. J.* **549(1)**, L47

Vogelsberger, M. et al: 2012, *Mon. Not. R. Astron. Soc.* **425(4)**, 3024

Vogt, C. and Enßlin, T.A.: 2005, *Astron. Astrophys.* **434(1)**, 67

Voigt, L.M. and Fabian, A.C.: 2004, *Mon. Not. R. Astron. Soc.* **347(4)**, 1130

Voigt, L.M. and Fabian, A.C.: 2006, *Mon. Not. R. Astron. Soc.* **368(2)**, 518

Voit, G.M.: 2005, *Rev. Mod. Phys.* **77(1)**, 207

Voit, G.M. et al: 2015, *Nature* **519(7542)**, 203

Webber, W.R.: 1998, *Astrophys. J.* **506(1)**, 329

Weinberger, R. et al: 2017, *preprint, (arXiv:1607.02212)*

Werner, N. et al: 2013, *Astrophys. J.* **767(2)**, 153

Werner, N. et al: 2014, *Mon. Not. R. Astron. Soc.* **439(3)**, 2291

Wiener, J., Oh, S.P. and Guo, F.: 2013, *Mon. Not. R. Astron. Soc.* **434(3)**, 2209

Wise, M.W. et al: 2007, *Astrophys. J.* **659(2)**, 1153

Worrall, D. and Birkinshaw, M.: 2000, *Astrophys. J.* **530(2)**, 719

Worrall, D.M.: 2009, *The X-ray jets of active galaxies*, Vol. 17

Yan, H. and Lazarian, A.: 2002, *Phys. Rev. Lett.* **89(28)**, 1102

Yang, H.Y.K. and Reynolds, C.S.: 2016a, *Astrophys. J.* **829(2)**, 90

Yang, H.Y.K. and Reynolds, C.S.: 2016b, *Astrophys. J.* **818(2)**, 181

Young, A.J., Wilson, A.S. and Mundell, C.G.: 2002, *Astrophys. J.* **579(2)**, 560

Yuan, Z.S., Han, J.L. and Wen, Z.L.: 2015, *Astrophys. J.* **813(1)**, 77

Zakamska, N.L. and Narayan, R.: 2003, *Astrophys. J.* **582(1)**, 162

Zhu, Q., Hernquist, L. and Li, Y.: 2015, *Astrophys. J.* **800(1)**, 6

Zhuravleva, I. et al: 2014, *Nature* **515(7525)**, 85

ZuHone, J.A. et al: 2015, *Astrophys. J.* **798(2)**, 90

ZuHone, J.A. et al: 2013, *Astrophys. J.* **762(2)**, 69

ZuHone, J.A. et al: 2016, *Astrophys. J.* **821(1)**, 6

Zweibel, E.G.: 2013, *Phys. Plasmas* **20(5)**, 055501

Zweibel, E.G.: 2017, *Phys. Plasmas* **24(5)**, 055402

Erklärung:

Ich versichere, dass ich diese Arbeit selbstständig verfasst habe und keine anderen als die angegebenen Quellen und Hilfsmittel benutzt habe.

Heidelberg, den (Datum) .....